

## Updated Combination of CDF and D0 Searches for Standard Model Higgs Boson Production with up to $10.0 \text{ fb}^{-1}$ of Data

The TEVNPH Working Group\*

for the CDF and D0 Collaborations

September 18, 2018

We combine results from the CDF and D0 Collaborations on direct searches for the standard model (SM) Higgs boson ( $H$ ) in  $p\bar{p}$  collisions at the Fermilab Tevatron at  $\sqrt{s} = 1.96 \text{ TeV}$ . Compared to the previous Tevatron Higgs boson search combination, more data have been included in those channels that hadn't previously used the full dataset, additional channels have been incorporated, and some previously used channels have been reanalyzed to gain sensitivity. Searches are carried out for hypothesized Higgs boson masses between 100 and 200  $\text{GeV}/c^2$ . With up to  $10 \text{ fb}^{-1}$  of luminosity analyzed, the 95% C.L. median expected upper limits on Higgs boson production are factors of 0.89, 1.08, and 0.48 times the values of the SM cross section for Higgs bosons of mass  $m_H = 115 \text{ GeV}/c^2$ ,  $125 \text{ GeV}/c^2$ , and  $165 \text{ GeV}/c^2$ , respectively. In the absence of signal, we expect to exclude the regions  $100 < m_H < 120 \text{ GeV}/c^2$  and  $139 < m_H < 184 \text{ GeV}/c^2$ . We exclude, at the 95% C.L., two regions:  $100 < m_H < 103 \text{ GeV}/c^2$ , and  $147 < m_H < 180 \text{ GeV}/c^2$ . There is a significant excess of data events with respect to the background estimation in the mass range  $115 < m_H < 140 \text{ GeV}/c^2$ , which causes our observed limits to not be as stringent as expected. At  $m_H = 120 \text{ GeV}/c^2$ , the  $p$ -value for a background fluctuation to produce this excess is  $\sim 1.5 \times 10^{-3}$ , corresponding to a local significance of 3.0 standard deviations. The global significance (incorporating the look-elsewhere effect) for such an excess anywhere in the full mass range investigated is approximately 2.5 standard deviations. We also combine separately searches for  $H \rightarrow b\bar{b}$  and  $H \rightarrow W^+W^-$ . We find that the excess is concentrated in the  $H \rightarrow b\bar{b}$  channel, appearing in the searches over a broad range of  $m_H$ . The maximum local significance of 3.2 standard deviations corresponds to a global significance of approximately 2.9 standard deviations. Our results in the  $H \rightarrow W^+W^-$  channels are also consistent with the possible presence of a low-mass Higgs boson.

*Preliminary Results*

---

\* The Tevatron New-Phenomena and Higgs Working Group can be contacted at [TEVNPHWG@fnal.gov](mailto:TEVNPHWG@fnal.gov). More information can be found at <http://tevnphwg.fnal.gov/>.

## I. INTRODUCTION

Understanding the mechanism for electroweak symmetry breaking, specifically by testing for the presence or absence of the standard model (SM) Higgs boson, has been a major goal of particle physics for many years, and is a central part of the Fermilab Tevatron physics program. Both the CDF and D0 collaborations have performed new combinations [1, 2] of multiple direct searches for the SM Higgs boson. The new searches include more data in some channels, additional channels, and improved analysis techniques compared to previous iterations. Precision electroweak data, including the recently updated measurements of the  $W$ -boson mass from the CDF and D0 Collaborations [3, 4], yield an indirect constraint on the allowed mass of the Higgs boson,  $m_H < 152 \text{ GeV}/c^2$  [5], at 95% confidence level (C.L.). The Large Electron Positron Collider (LEP) has excluded Higgs boson masses below  $114.4 \text{ GeV}/c^2$  [6], and the LHC experiments, ATLAS and CMS, now limit the SM Higgs boson to have a mass between  $115.5$  and  $127 \text{ GeV}/c^2$  [7, 8] at the 95% C.L. Both LHC experiments report local  $\sim 3$  standard deviation (s.d.) excesses at approximately  $125 \text{ GeV}/c^2$ . The sensitivities of the new combinations presented here exceed those of previous Tevatron combinations [9, 10], providing sensitivity within the full allowed Higgs boson mass range.

In this note, we combine the most recent results of all such searches in  $p\bar{p}$  collisions at  $\sqrt{s} = 1.96 \text{ TeV}$  in the Higgs boson mass range from  $100$ – $200 \text{ GeV}/c^2$ . The analyses combined here seek signals of Higgs bosons produced in association with a vector boson ( $q\bar{q} \rightarrow W/ZH$ ), through gluon-gluon fusion ( $gg \rightarrow H$ ), and through vector boson fusion (VBF) ( $q\bar{q} \rightarrow q'\bar{q}'H$ ) corresponding to integrated luminosities up to  $10.0 \text{ fb}^{-1}$  at CDF and up to  $9.7 \text{ fb}^{-1}$  at D0. The Higgs boson decay modes studied are  $H \rightarrow b\bar{b}$ ,  $H \rightarrow W^+W^-$ ,  $H \rightarrow ZZ$ ,  $H \rightarrow \tau^+\tau^-$  and  $H \rightarrow \gamma\gamma$ . For Higgs boson masses greater than  $125 \text{ GeV}/c^2$ ,  $H \rightarrow W^+W^-$  modes with leptonic decay provide the greatest sensitivity [11–14], while below  $125 \text{ GeV}/c^2$  sensitivity comes mainly from ( $q\bar{q} \rightarrow W/ZH$ ) where  $H$  decays to  $b\bar{b}$  and the  $W$  or  $Z$  boson decays leptonically [13, 15, 16]. The dominant decay mode for a low mass Higgs boson is  $H \rightarrow b\bar{b}$ , and thus measurements of this process provide constraints on possible Higgs boson phenomenology that are complementary to those provided by the LHC.

To simplify the combination, the searches are separated into mutually exclusive final states referred to as “analysis sub-channels” in this note. Listings of these analysis sub-channels are provided in Tables I and II. The selection procedures for each analysis are detailed in Refs. [17] through [38], and are briefly described below.

## II. ACCEPTANCE, BACKGROUNDS, AND LUMINOSITY

Event selections are similar for the corresponding CDF and D0 analyses, consisting typically of a preselection followed by the use of a multivariate analysis technique with a final discriminating variable to separate signal and background. For the case of  $WH \rightarrow \ell\nu b\bar{b}$ , an isolated charged lepton ( $\ell = \text{electron or muon}$ ) and two or three jets are required, with one or more of the jets being  $b$ -tagged, i.e., identified as containing a weakly-decaying  $B$  hadron. Selected events must also display a significant imbalance in transverse momentum (referred to as missing transverse energy or  $\cancel{E}_T$ ). Events with more than one isolated charged lepton are rejected.

The D0  $WH \rightarrow \ell\nu b\bar{b}$  analyses are now treated in a wider context as topologies with a charged lepton, missing energy and at least two jets are sensitive to  $WH \rightarrow \ell\nu b\bar{b}$  and  $VH \rightarrow VWW \rightarrow \ell\nu jjjj$  production. Events are classified based on jet multiplicity, lepton flavor and number of  $b$ -tagged jets, thus improving the overall sensitivity. As with other D0 analyses targeting the  $H \rightarrow b\bar{b}$  decay, a boosted decision tree based  $b$ -tagging algorithm, which builds and improves upon the previous neural network  $b$ -tagger [39], is used. For example, the loose  $b$ -tagging criterion corresponds to an identification efficiency of  $\approx 80\%$  for true  $b$ -jets for a mis-identification rate of  $\approx 10\%$ . Six orthogonal  $b$ -tagging categories are defined. To avoid overlap with the  $H \rightarrow W^+W^- \rightarrow \ell\nu jj$  analysis, the four categories with the greatest purity are kept, namely those corresponding to events with a single tight  $b$ -tagged jet (TST), two loose  $b$ -tagged jets (LDT), two medium  $b$ -tagged jets (MDT) and two tight  $b$ -tagged jets (TDT). Boosted decision trees are also used to discriminate against the multijet background. The output of these decision trees are used inputs to the final discriminants which are again boosted decision trees, trained separately for each sub-sample (i.e. jet multiplicity, lepton flavor and  $b$ -tag category) and for each Higgs boson mass. Overall, the sensitivity has been improved by  $\approx 10$ – $15\%$  with respect to the previous result.

For the CDF  $WH \rightarrow \ell\nu b\bar{b}$  analyses, events are analyzed in two and three jet sub-channels separately, and in each

of these samples the events are grouped into various lepton and  $b$ -tag categories. Events are broken into separate analysis categories based on the quality of the identified lepton. Separate categories are used for events with a high quality central muon or central electron candidate, an isolated track or identified loose muon in the extended muon coverage, a forward electron candidate, and a loose central electron or a loose isolated track candidate. The final two lepton categories, which provide some acceptance for lower quality electrons and single prong tau decays, are used only in the case of two-jet events. Within the lepton categories there are five  $b$ -tagging categories considered for two-jet events: two tight  $b$  tags (TT), one tight  $b$  tag and one loose  $b$  tag (TL), a single tight  $b$  tag (Tx), two loose  $b$  tags (LL), and a single loose  $b$  tag. For three jet categories only the TT and TL  $b$ -tagging categories are considered. The tight and loose  $b$ -tag definitions are taken from a neural network tagging algorithm [40] based on sets of kinematic variables sensitive to displaced decay vertices and tracks within jets with large transverse impact parameters relative to the hard-scatter vertices. Using an operating point that gives an equivalent rate of false tags, the new algorithm improves the  $b$ -tagging efficiency by  $\sim 20\%$ . A Bayesian neural network discriminant is trained at each Higgs boson mass in  $5 \text{ GeV}/c^2$  steps within the test range for each of the specific categories (defined by lepton type,  $b$ -tagging type, and number of jets) to separate signal from backgrounds.

For the  $ZH \rightarrow \nu\bar{\nu}b\bar{b}$  analyses, the selection is similar to the  $WH$  selection, except all events with isolated leptons are rejected and stronger multijet background suppression techniques are applied. Both the CDF and D0 analyses use a track-based missing transverse momentum calculation as a discriminant against false  $\cancel{E}_T$ . In addition both CDF and D0 utilize multivariate techniques, a boosted decision tree at D0 and a neural network at CDF, to further discriminate against the multijet background before  $b$  tagging. There is a sizable fraction of the  $WH \rightarrow \ell\nu b\bar{b}$  signal in which the lepton is undetected that is selected in the  $ZH \rightarrow \nu\bar{\nu}b\bar{b}$  samples, so these analyses are also referred to as  $VH \rightarrow \cancel{E}_T b\bar{b}$ . The CDF analysis uses three non-overlapping categories of  $b$ -tagged events (SS, SJ and 1S). These categories are based on two older CDF  $b$ -tagging algorithms, an algorithm for reconstructing displaced, secondary vertices of  $b$ -quark decays (S) and an algorithm for assigning a likelihood for tracks within a jet to have originated from a displaced vertex (J). The D0 analysis requires exactly two jets. The  $b$ -tagging criteria are optimized to reduce the loss in sensitivity due to systematic uncertainties. The  $b$ -tagger output values for each of the two jets are added to form an event  $b$  tag, the value of which is used to define two high purity samples: the medium  $b$ -tag sample (MS) and the tight  $b$ -tag sample (TS). After applying a multijet veto, these samples have a signal-to-background ratio of 0.4% and 1.5% respectively. Boosted decision trees (BDT), trained separately for the different  $b$ -tagging categories and at each test mass, are used as the final discriminant. Improved training of the BDTs has been implemented; this, and a number of other small improvements, leads to a gain in sensitivity of  $\approx 10\%$  with respect to the previous result. The CDF analysis uses a second layer of neural network discriminants for separating signal from backgrounds.

The  $ZH \rightarrow \ell^+\ell^-b\bar{b}$  analyses require two isolated leptons and at least two jets. The lack of missing energy from neutrinos allows for a significantly better dijet mass resolution in this channel than in the  $WH \rightarrow \ell\nu b\bar{b}$  and  $ZH \rightarrow \nu\bar{\nu}b\bar{b}$  analyses due to the use of event-wide transverse momentum constraints. D0's  $ZH \rightarrow \ell^+\ell^-b\bar{b}$  analyses separate events into non-overlapping samples of events with either one tight  $b$  tag (TST) or one tight  $b$  tag and one loose  $b$  tag (TLDT). CDF has incorporated its neural network  $b$ -tagging algorithm in this analysis and uses four out of the five  $WH$  tagging categories (TT, TL, Tx, and LL). CDF now also separates events with two or three jets into independent analysis channels. Relative to the analysis that was combined in Ref. [9], the  $Z$ +heavy flavor background prediction was increased by a factor of 1.4, and heavy-flavor contributions were subtracted from the  $Z$ +light-flavor Monte Carlo. The net effect of these two modifications resulted in a negligible effect on the observed outcome and the predicted sensitivity of this channel. To increase signal acceptance D0 loosens the selection criteria for one of the leptons to include an isolated track not reconstructed in the muon detector ( $\mu\mu_{trk}$ ) or an electron from the inter-cryostat region of the D0 detector ( $ee_{ICR}$ ). Combined with the dielectron ( $ee$ ) and dimuon ( $\mu\mu$ ) analyses these provide four orthogonal analyses. CDF uses neural networks to select loose dielectron and dimuon candidates. D0 applies a kinematic fit to optimize reconstruction, improving the mass resolution by  $\approx 15\%$ . CDF corrects jet energies for  $\cancel{E}_T$  using a neural network approach. D0 uses random forests of decision trees (RF) to provide the final variables for setting limits. For this iteration of the analysis, a two-step process is applied. Initially a RF is used to separate signal and  $t\bar{t}$  background, thus producing  $t\bar{t}$ -depleted and  $t\bar{t}$ -enriched samples. A second 'global' RF is then used to separate signal from all backgrounds. The final limit is calculated using the output distributions of the global RF for both the  $t\bar{t}$ -depleted and -enriched samples. Overall an improvement in sensitivity of  $\approx 10$ -15% is achieved compared to the previous result. CDF utilizes a multi-layer discriminant based on neural networks where separate discriminant functions are used to define four separate regions of the final discriminant function.

For the  $H \rightarrow W^+W^-$  analyses, signal events are characterized by large  $\cancel{E}_T$  and two opposite-signed, isolated leptons. The presence of neutrinos in the final state prevents the accurate reconstruction of the candidate Higgs boson mass. D0 selects events containing electrons and/or muons, dividing the data sample into three final states:  $e^+e^-$ ,  $e^\pm\mu^\mp$ , and  $\mu^+\mu^-$ . Each final state is further subdivided according to the number of jets in the event: 0, 1, or 2 or more (“2+”) jets. The dimuon and dielectron channels use boosted decision trees to reduce the dominant Drell-Yan background. Decays involving tau leptons are included in two orthogonal ways. A dedicated analysis ( $\mu\tau_{\text{had}}$ ) using  $7.3 \text{ fb}^{-1}$  of integrated luminosity studying the final state involving a muon and a hadronic tau decay plus up to one jet is included in the Tevatron combination. Final states involving other tau decays and mis-identified hadronic tau decays are included in the  $e^+e^-$ ,  $e^\pm\mu^\mp$ , and  $\mu^+\mu^-$  final state analyses. CDF separates the  $H \rightarrow W^+W^-$  events in five non-overlapping samples, split into “high  $s/b$ ” and “low  $s/b$ ” categories defined by lepton types and the number of reconstructed jets: 0, 1, or 2+ jets. The sample with two or more jets is not split into low  $s/b$  and high  $s/b$  lepton categories due to the smaller statistics in this channel. The D0  $e^+e^-$ ,  $e^\pm\mu^\mp$ , and  $\mu^+\mu^-$  final state channels use boosted decision trees as the final discriminants; for categories with non-zero jet multiplicity  $b$ -tagging information is included. The dimuon and dielectron analyses sub-divide the 0 and 1 jet categories into  $WW$ -enriched and  $WW$ -depleted using dedicated boosted decision trees. All sub-samples are used in the limit setting, with the additional channels significantly constraining the uncertainty on the  $WW$  cross-section. Overall, the gain in sensitivity is  $\approx 5$ -10%. The  $\mu\tau_{\text{had}}$  channel uses neural networks as the final discriminant. CDF uses neural-network outputs, including likelihoods constructed from calculated matrix-element probabilities as additional inputs for the 0-jet bin. A sixth CDF channel is the low dilepton mass ( $m_{\ell^+\ell^-}$ ) channel, which accepts events with  $m_{\ell^+\ell^-} < 16 \text{ GeV}/c^2$ . CDF has further improved its analysis of the low dilepton mass channel by reducing the  $\Delta R$  cut applied to dilepton pairs down to 0.1, which increases Higgs signal acceptance in this channel by  $\sim 10\%$ .

The division of events into categories based on the number of reconstructed jets allows the analysis discriminants to separate differing contributions of signal and background processes more effectively. The signal production mechanisms considered are  $gg \rightarrow H \rightarrow W^+W^-$ ,  $WH/ZH \rightarrow jjW^+W^-$ , and vector-boson fusion. The relative fractions of the contributions from each of the three signal processes and background processes, notably  $W^+W^-$  production and  $t\bar{t}$  production, are very different in the different jet categories. Dividing our data into these categories provides more statistical discrimination, but introduces the need to evaluate the systematic uncertainties carefully in each jet category. A discussion of these uncertainties is found in Section III.

D0 includes a  $VH \rightarrow \ell^\pm\ell'^\pm + X$  analysis in which the associated vector boson and the  $W$  boson from the Higgs boson decay are required to decay leptonically, giving like-sign dilepton final states. Previously the three final  $e^\pm e^\pm$ ,  $e^\pm\mu^\pm$ , and  $\mu^\pm\mu^\pm$  had been considered, in this combination (as in the previous combination) only the most sensitive  $e^\pm\mu^\pm$  final state is included. The combined output of two decision trees, trained against the instrumental and diboson backgrounds respectively, is used as the final discriminant. D0 includes tri-lepton analyses to increase the sensitivity to associated production and other decay modes, such as  $H \rightarrow ZZ$ . The  $ee\mu$ ,  $\mu\mu e$  and  $\tau\tau\mu$  final states are considered. The  $ee\mu$  and  $\mu\mu e$  final states use boosted decision trees as the final discriminants. The  $\mu\mu e$  and  $\tau\tau\mu$  final states are sub-divided to improve the sensitivity. The former is divided into three sub-samples with enriched  $ZH$  or  $WH$  content and varying levels of background contamination and the later is divided according to the jet multiplicity and a kinematic variable based on the event  $P_T$  used as the discriminating variable.

CDF also includes a separate analysis of events with same-sign leptons to incorporate additional potential signal from associated production events in which the two leptons (one from the associated vector boson and one from a  $W$  boson produced in the Higgs boson decay) have the same charge. CDF additionally incorporates three tri-lepton channels to include additional associated production contributions in which leptons result from the associated  $W$  boson and the two  $W$  bosons produced in the Higgs boson decay or where an associated  $Z$  boson decays into a dilepton pair and a third lepton is produced in the decay of either of the  $W$  bosons resulting from the Higgs boson decay. In the latter case, CDF separates the sample into one jet and two or more jet sub-channels to take advantage of the fact that the Higgs boson candidate mass can be reconstructed from the invariant mass of the two jets, the lepton, and the missing transverse energy. CDF also includes a tri-lepton channel focusing on  $WH$  production in which one of the three leptons is reconstructed as a hadronic tau.

CDF includes a search for  $H \rightarrow ZZ$  using four lepton events. In addition to the simple four-lepton invariant mass discriminant used previously for separating potential Higgs boson signal events from the non-resonant  $ZZ$  background, the  $\cancel{E}_T$  in these events is now used as a second discriminating variable to better identify four lepton signal contributions from  $ZH \rightarrow ZWW$  and  $ZH \rightarrow Z\tau\tau$  production. CDF also contributes opposite-sign channels in which one of the

two lepton candidates is a hadronic tau. Events are separated into  $e\text{-}\tau$  and  $\mu\text{-}\tau$  channels. The final discriminants are obtained from boosted decision trees which incorporate both hadronic tau identification and kinematic event variables as inputs.

D0 also includes channels in which one of the  $W$  bosons in the  $H \rightarrow W^+W^-$  process decays leptonically and the other decays hadronically. Electron and muon final states are studied separately. Random forests are used for the final discriminants.

CDF includes a generic analysis searching for Higgs bosons decaying to tau lepton pairs incorporating contributions from direct  $gg \rightarrow H$  production, associated  $WH$  or  $ZH$  production, and vector boson fusion production. CDF also includes an analysis of events that contain one or more reconstructed leptons ( $\ell = e$  or  $\mu$ ) in addition to a tau lepton pair focusing on associated production where  $H \rightarrow \tau\tau$  and additional leptons are produced in the decay of the  $W$  or  $Z$  boson. For these searches, multiple Support Vector Machine (SVM) [41] classifiers are obtained using separate trainings for the signal against each of the primary backgrounds. In the generic search, events with either one or two jets are separated into two independent analysis channels. The final discriminant for setting limits is obtained using the minimum score of four SVM classifiers obtained from trainings against the primary backgrounds ( $Z \rightarrow \tau\tau$ ,  $t\bar{t}$ , multijet, and  $W$ +jet production). In the extended analysis events are separated into five separate analysis channels ( $\ell\ell\ell$ ,  $e\mu\tau_{\text{had}}$ ,  $\ell\ell\tau_{\text{had}}$ ,  $\ell\tau_{\text{had}}\tau_{\text{had}}$ , and  $\ell\ell\ell\ell$ ). The four lepton category includes  $\tau_{\text{had}}$  candidates. The final discriminants are likelihoods based on outputs obtained from independent SVM trainings against each of the primary backgrounds ( $Z$ +jets,  $t\bar{t}$ , and dibosons). These channels are included in the combination only for lower Higgs masses to avoid overlap with other search channels.

CDF incorporates an all-hadronic analysis based on the older CDF  $b$ -tagging algorithms, which results in two sub-channels (SS and SJ). Both  $WH/ZH$  and VBF production contribute to the  $jjb\bar{b}$  final state. Events with either four or five reconstructed jets are selected, and at least two must be  $b$ -tagged. The large QCD multijet backgrounds are modeled from the data by applying a measured mistag probability to the non  $b$ -tagged jets in events containing a single  $b$ -tagged jet. Neural network discriminants based on kinematic event variables including those designed to separate quark and gluon jets are used to obtain the final limits.

D0 and CDF both contribute analyses searching for Higgs bosons decaying into diphoton pairs. The CDF analysis looks for a signal peak in the diphoton invariant mass spectrum above the smooth background originating from QCD production. Events are separated into four independent analysis channels based on the photon candidates contained within the event: two central candidates (CC), one central and one plug candidate (CP), one central and one central conversion candidate (C'C), or one plug and one central conversion candidate (C'P). In the D0 analysis, the contribution of jets misidentified as photons is reduced by combining information sensitive to differences in the energy deposition from these particles in the tracker, calorimeter and central preshower in a neural network (ONN). The output of boosted decision trees, rather than the diphoton invariant mass, is used as the final discriminating variable. Input variables include the transverse energies of the leading two photons, the azimuthal opening angle between them, the diphoton invariant mass and transverse momentum and the ONN output value. Improved vertexing and energy calibrations have been incorporated. Additionally the impact of systematic uncertainties is now reduced by inclusion of photon-dominated and jet-dominated sub-samples in the limit setting procedure. Overall a sizeable improvement in sensitivity of  $\approx 30\%$  is achieved.

CDF incorporates three non-overlapping sets of analysis channels searching for the process  $t\bar{t}H \rightarrow t\bar{t}b\bar{b}$ . One set of channels selects events with a reconstructed lepton, large missing transverse energy, and four or more reconstructed jets. Events containing four, five, and six or more jets are analyzed separately and further sub-divided into five  $b$ -tagging categories based on the older CDF tagging algorithms (three tight  $b$  tags (SSS), two tight and one loose  $b$  tags (SSJ), one tight and two loose  $b$  tags (SJJ), two tight  $b$  tags (SS), and one tight  $b$  tag and one loose  $b$  tag (SJ)). Neural network discriminants trained at each mass point are used to set limits. A second set of channels selects events with no reconstructed lepton. These events are separated into two categories, one containing events with large missing transverse energy and five to nine reconstructed jets and another containing events with low missing transverse energy and seven to ten reconstructed jets. Events in these two channels are required to have a minimum of two  $b$ -tagged jets based on an independent neural network tagging algorithm. Events with three or more  $b$  tags are analyzed in separate channels from those with exactly two tags. Two stages of neural network discriminants are used (the first helps reject large multijet backgrounds and the second separates potential  $t\bar{t}H$  signal events from  $t\bar{t}$  background events).

For both CDF and D0, events from QCD multijet (instrumental) backgrounds are typically measured in independent data samples using several different methods. For CDF, backgrounds from SM processes with electroweak gauge bosons

or top quarks were generated using PYTHIA [42], ALPGEN [43], MC@NLO [44], and HERWIG [45] programs. For D0, these backgrounds were generated using PYTHIA, ALPGEN, and COMPHEP [46], with PYTHIA providing parton-showering and hadronization for all the generators. These background processes were normalized using either experimental data or next-to-leading order calculations (including MCFM [47] for the  $W$ + heavy flavor process). All Monte Carlo samples are passed through detailed GEANT-based simulations [48] of the CDF and D0 detectors.

Tables I and II summarize, for CDF and D0 respectively, the integrated luminosities, the Higgs boson mass ranges over which the searches are performed, and references to further details for each analysis.

TABLE I: Luminosity, explored mass range and references for the different processes and final states ( $\ell = e$  or  $\mu$ ) for the CDF analyses. The generic labels “2 $\times$ ”, “3 $\times$ ”, and “4 $\times$ ” refer to separations based on lepton categories.

Channel	Luminosity (fb <sup>-1</sup> )	$m_H$ range (GeV/ $c^2$ )	Reference
$WH \rightarrow \ell\nu b\bar{b}$ 2-jet channels	4 $\times$ (TT,TL,Tx,LL,Lx)	9.45	100-150 [17]
$WH \rightarrow \ell\nu b\bar{b}$ 3-jet channels	3 $\times$ (TT,TL)	9.45	100-150 [17]
$ZH \rightarrow \nu\bar{\nu} b\bar{b}$ (SS,SJ,1S)		9.45	100-150 [18]
$ZH \rightarrow \ell^+\ell^-\bar{b}\bar{b}$ 2-jet channels	2 $\times$ (TT,TL,Tx,LL)	9.45	100-150 [19]
$ZH \rightarrow \ell^+\ell^-\bar{b}\bar{b}$ 3-jet channels	2 $\times$ (TT,TL,Tx,LL)	9.45	100-150 [19]
$H \rightarrow W^+W^-$ 2 $\times$ (0 jets,1 jet)+(2 or more jets)+(low- $m_{\ell\ell}$ )		9.7	110-200 [20]
$H \rightarrow W^+W^-$ ( $e$ - $\tau_{\text{had}}$ )+( $\mu$ - $\tau_{\text{had}}$ )		9.7	130-200 [21]
$WH \rightarrow WW^+W^-$ (same-sign leptons)+(tri-leptons)		9.7	110-200 [20]
$WH \rightarrow WW^+W^-$ tri-leptons with 1 $\tau_{\text{had}}$		9.7	130-200 [21]
$ZH \rightarrow ZW^+W^-$ (tri-leptons with 1 jet)+(tri-leptons with 2 or more jets)		9.7	110-200 [20]
$H \rightarrow ZZ$ four leptons		9.7	120-200 [22]
$H + X \rightarrow \tau^+\tau^-$ (1 jet)+(2 jets)		8.3	100-150 [23]
$WH \rightarrow \ell\nu\tau^+\tau^-/ZH \rightarrow \ell^+\ell^-\tau^+\tau^-$ $\ell$ - $\tau_{\text{had}}$ - $\tau_{\text{had}}$		6.2	100-150 [24]
$WH \rightarrow \ell\nu\tau^+\tau^-/ZH \rightarrow \ell^+\ell^-\tau^+\tau^-$ ( $\ell$ - $\ell$ - $\tau_{\text{had}}$ )+(e- $\mu$ - $\tau_{\text{had}}$ )		6.2	100-125 [24]
$WH \rightarrow \ell\nu\tau^+\tau^-/ZH \rightarrow \ell^+\ell^-\tau^+\tau^-$ $\ell$ - $\ell$ - $\ell$		6.2	100-105 [24]
$ZH \rightarrow \ell^+\ell^-\tau^+\tau^-$ four leptons including $\tau_{\text{had}}$ candidates		6.2	100-115 [24]
$WH + ZH \rightarrow jjb\bar{b}$ (SS,SJ)		9.45	100-150 [25]
$H \rightarrow \gamma\gamma$ (CC,CP,C'C,C'P)		10.0	100-150 [26]
$t\bar{t}H \rightarrow WWb\bar{b}b\bar{b}$ (lepton) (4jet,5jet, $\geq$ 6jet) $\times$ (SSS,SSJ,SJJ,SS,SJ)		9.45	100-150 [27]
$t\bar{t}H \rightarrow WWb\bar{b}b\bar{b}$ (no lepton) (low met,high met) $\times$ (2 tags,3 or more tags)		5.7	100-150 [28]

### III. SIGNAL PREDICTIONS

In order to predict the kinematic distributions of Higgs boson signal events, CDF and D0 use the PYTHIA [42] Monte Carlo program, with CTEQ5L and CTEQ6L1 [49] leading-order (LO) parton distribution functions. We scale these Monte Carlo predictions to the most recent higher-order calculations of inclusive cross sections, and differential cross sections, such as in the Higgs boson  $p_T$  spectrum and the number of associated jets, as described below. The  $gg \rightarrow H$  production cross section we use is calculated at next-to-next-to leading order (NNLO) in QCD with a next-to-next-to leading log (NNLL) resummation of soft gluons; the calculation also includes two-loop electroweak effects and handling of the running  $b$  quark mass [50, 51]. The numerical values in Table III are updates [52] of these predictions with  $m_t$  set to 173.1 GeV/ $c^2$  [53], and with a treatment of the massive top and bottom loop corrections up to next-to-leading-order (NLO) + next-to-leading-log (NLL) accuracy. The factorization and renormalization scale choice for this calculation is  $\mu_F = \mu_R = m_H$ . These calculations are refinements of the earlier NNLO calculations of the  $gg \rightarrow H$  production cross section [54–56]. Electroweak corrections were computed in Refs. [57, 58]. Soft gluon resummation was introduced in the prediction of the  $gg \rightarrow H$  production cross section in Ref. [59]. The  $gg \rightarrow H$  production cross

TABLE II: Luminosity, explored mass range and references for the different processes and final states ( $\ell = e, \mu$ ) for the D0 analyses.

Channel	Luminosity ( $\text{fb}^{-1}$ )	$m_H$ range ( $\text{GeV}/c^2$ )	Reference
$H+(X)\rightarrow\ell\nu+\geq jj$ (0,1, $\geq 2b$ tags) $\times$ (2,3,4+ jet)	9.7	100-200	[29]
$ZH\rightarrow\nu\bar{\nu}b\bar{b}$ (MS,TS)	9.5	100-150	[30]
$ZH\rightarrow\ell^+\ell^-b\bar{b}$ (TST,TLDT) $\times$ ( $ee,\mu\mu,ee_{ICR},\mu\mu_{trk}$ )	9.7	100-150	[31]
$VH\rightarrow e^\pm\mu^\pm+X$	9.7	115-200	[33]
$H\rightarrow W^+W^-\rightarrow\ell^\pm\nu\ell^\mp\nu$ (0,1,2+ jet)	9.7	115-200	[34]
$H\rightarrow W^+W^-\rightarrow\mu\nu\tau_{\text{had}}\nu$	7.3	115-200	[32]
$H\rightarrow W^+W^-\rightarrow\ell\bar{\nu}jj$	5.4	130-200	[35]
$VH\rightarrow\ell\ell\ell+X$	9.7	100-200	[36]
$VH\rightarrow\tau\tau\mu+X$	7.0	115-200	[37]
$H\rightarrow\gamma\gamma$	9.7	100-150	[38]

section depends strongly on the gluon parton density function, and the accompanying value of  $\alpha_s(q^2)$ . The cross sections used here are calculated with the MSTW 2008 NNLO PDF set [60], as recommended by the PDF4LHC working group [61]. The inclusive Higgs boson production cross sections are listed in Table III.

For analyses that consider inclusive  $gg\rightarrow H$  production but do not split it into separate channels based on the number of reconstructed jets, we use the inclusive uncertainties from the simultaneous variation of the factorization and renormalization scale up and down by a factor of two. We use the prescription of the PDF4LHC working group for evaluating PDF uncertainties on the inclusive production cross section. QCD scale uncertainties that affect the cross section via their impacts on the PDFs are included as a correlated part of the total scale uncertainty. The remainder of the PDF uncertainty is treated as uncorrelated with the QCD scale uncertainty.

For analyses seeking  $gg\rightarrow H$  production that divide events into categories based on the number of reconstructed jets, we employ a new approach for evaluating the impacts of the scale uncertainties. Following the recommendations of Ref. [62, 63], we treat the QCD scale uncertainties obtained from the NNLL inclusive [50, 51], NLO one or more jets [64], and NLO two or more jets [65] cross section calculations as uncorrelated with one another. We then obtain QCD scale uncertainties for the exclusive  $gg\rightarrow H+0$  jet, 1 jet, and 2 or more jet categories by propagating the uncertainties on the inclusive cross section predictions through the subtractions needed to predict the exclusive rates. For example, the  $H+0$  jet cross section is obtained by subtracting the NLO  $H+1$  or more jet cross section from the inclusive NNLL+NNLO cross section. We now assign three separate, uncorrelated scale uncertainties which lead to correlated and anticorrelated uncertainty contributions between exclusive jet categories. The procedure in Ref. [64] is used to determine PDF model uncertainties. These are obtained separately for each jet bin and treated as 100% correlated between jet bins and between D0 and CDF.

The scale choice affects the  $p_T$  spectrum of the Higgs boson when produced in gluon-gluon fusion, and this effect changes the acceptance of the selection requirements and also the shapes of the distributions of the final discriminants. The effect of the acceptance change is included in the calculations of Ref. [64] and Ref. [65], as the experimental requirements are simulated in these calculations. The effects on the final discriminant shapes are obtained by reweighting the  $p_T$  spectrum of the Higgs boson production in the Monte Carlo simulations to higher-order calculations. The Monte Carlo signal simulation used by CDF and D0 is provided by the LO generator PYTHIA [42] which includes a parton shower and fragmentation and hadronization models. We reweight the Higgs boson  $p_T$  spectra in our PYTHIA Monte Carlo samples to that predicted by HQT [66] when making predictions of differential distributions of  $gg\rightarrow H$  signal events. To evaluate the impact of the scale uncertainty on our differential spectra, we use the RESBOS [67] generator, and apply the scale-dependent differences in the Higgs boson  $p_T$  spectrum to the HQT prediction, and propagate these to our final discriminants as a systematic uncertainty on the shape, which is included in the calculation of the limits.

We include all significant Higgs boson production modes in the high-mass search. Besides gluon-gluon fusion through virtual quark loops (ggH), we include Higgs boson production in association with a  $W$  or  $Z$  vector boson (VH), and vector boson fusion (VBF). For the low-mass searches, we target the  $WH$ ,  $ZH$ , VBF, and  $t\bar{t}H$  production

modes with specific searches, including also those signal components not specifically targeted but which fall in the acceptance nonetheless. Our  $WH$  and  $ZH$  cross sections are from Ref. [68]. This calculation starts with the NLO calculation of v2HV [69] and includes NNLO QCD contributions [70], as well as one-loop electroweak corrections [71]. A similar calculation of the  $WH$  cross section is available in Ref. [72]. We use the VBF cross section computed at NNLO in QCD in Ref. [73]. Electroweak corrections to the VBF production cross section are computed with the HAWK program [74], and are small and negative (2-3%) in the Higgs boson mass range considered here. We include these corrections in the VBF cross sections used for this result. The  $t\bar{t}H$  production cross sections we use are from Ref. [75].

The Higgs boson decay branching ratio predictions used for this result are those of Ref. [63, 76]. In this calculation, the partial decay widths for all Higgs boson decays except to pairs of  $W$  and  $Z$  bosons are computed with HDECAY [77], and the  $W$  and  $Z$  pair decay widths are computed with PROPHECY4F [78]. The relevant decay branching ratios are listed in Table III. The uncertainties on the predicted branching ratios from uncertainties in  $m_b$ ,  $m_c$ ,  $\alpha_s$ , and missing higher-order effects are presented in Ref. [79, 80].

#### IV. DISTRIBUTIONS OF CANDIDATES

All analyses provide binned histograms of the final discriminant variables for the signal and background predictions, itemized separately for each source, and the observed data. The number of channels combined is large, and the number of bins in each channel is large. Therefore, the task of assembling histograms and visually checking whether the expected and observed limits are consistent with the input predictions and observed data is difficult. We therefore provide histograms that aggregate all channels' signal, background, and data together. In order to preserve most of the sensitivity gain that is achieved by the analyses by binning the data instead of collecting them all together and counting, we aggregate the data and predictions in narrow bins of signal-to-background ratio,  $s/b$ . Data with similar  $s/b$  may be added together with no loss in sensitivity, assuming similar systematic uncertainties on the predictions. The aggregate histograms do not show the effects of systematic uncertainties, but instead compare the data with the central predictions supplied by each analysis.

The range of  $s/b$  is quite large in each analysis, and so  $\log_{10}(s/b)$  is chosen as the plotting variable. Plots of the distributions of  $\log_{10}(s/b)$  are shown for Higgs boson masses of 115, 125, and 165 GeV/ $c^2$  in Figure 1, demonstrating agreement with background over five orders of magnitude. These distributions can be integrated from the high- $s/b$  side downwards, showing the sums of signal, background, and data for the most pure portions of the selection of all channels added together. The integrals of the  $\approx 100$  highest  $s/b$  events are shown in Figure 2, plotted as functions of the number of signal events expected. Only the statistical errors, which are correlated point-to-point, are shown. The most significant candidates are found in the bins with the highest  $s/b$ ; an excess in these bins relative to the background prediction drives the Higgs boson cross section limit upwards, while a deficit drives it downwards. The lower- $s/b$  bins show that the modeling of the rates and kinematic distributions of the backgrounds is very good. The integrated plots show that the data are more consistent with the signal-plus-background hypothesis than the background-only hypothesis for the analyses seeking a Higgs boson mass of 125 GeV/ $c^2$ , and that a deficit of events in the highest- $s/b$  bins for the analyses seeking a Higgs boson of mass 165 GeV/ $c^2$  is observed.

We also show the distributions of the data after subtracting the expected background, and compare that with the expected signal yield for a standard model Higgs boson, after collecting all bins in all channels sorted by  $s/b$ . These background-subtracted distributions are shown in Figure 3 for Higgs boson masses of 115, 125, 135, and 165 GeV/ $c^2$ . These graphs also show the remaining uncertainty on the background prediction after fitting the background model to the data within the systematic uncertainties on the rates and shapes in each contributing channel.

In addition to the combined searches for the SM Higgs boson, we also focus our attention on the  $WH \rightarrow \ell\nu b\bar{b}$ ,  $ZH \rightarrow \nu\bar{\nu} b\bar{b}$ , and  $ZH \rightarrow \ell^+\ell^- b\bar{b}$  searches in the following sections. The corresponding candidate distribution graphs of the  $\log_{10}(s/b)$  distributions are shown in Figure 4, the integrals of these from the high  $s/b$  side are shown in Figure 5, and the background-subtracted data distributions are shown in Figure 6 for the searches optimized at  $m_H = 115, 125, 130,$  and  $135$  GeV/ $c^2$ . A powerful ingredient to the  $WH \rightarrow \ell\nu b\bar{b}$ ,  $ZH \rightarrow \nu\bar{\nu} b\bar{b}$ , and  $ZH \rightarrow \ell^+\ell^- b\bar{b}$  search MVAs is the reconstructed dijet mass  $m_{jj}$ . We verify the modeling of the distribution of this variable by showing in Figure 7, taken from [81] which used luminosities from 7.5-9.5 fb $^{-1}$ , the sum of the CDF and D0 data for the singly-tagged, doubly-tagged, and the sum of the two sets, with all backgrounds except  $WZ$  and  $ZZ$  subtracted. The diboson signal



TABLE III: The production cross sections and decay branching fractions for the SM Higgs boson assumed for the combination.

$m_H$ (GeV/ $c^2$ )	$\sigma_{gg \rightarrow H}$ (fb)	$\sigma_{WH}$ (fb)	$\sigma_{ZH}$ (fb)	$\sigma_{VBF}$ (fb)	$\sigma_{t\bar{t}H}$ (fb)	$B(H \rightarrow b\bar{b})$ (%)	$B(H \rightarrow c\bar{c})$ (%)	$B(H \rightarrow \tau^+\tau^-)$ (%)	$B(H \rightarrow W^+W^-)$ (%)	$B(H \rightarrow ZZ)$ (%)	$B(H \rightarrow \gamma\gamma)$ (%)
100	1821.8	281.1	162.7	97.3	8.0	79.1	3.68	8.36	1.11	0.113	0.159
105	1584.7	238.7	139.5	89.8	7.1	77.3	3.59	8.25	2.43	0.215	0.178
110	1385.0	203.7	120.2	82.8	6.2	74.5	3.46	8.03	4.82	0.439	0.197
115	1215.9	174.5	103.9	76.5	5.5	70.5	3.27	7.65	8.67	0.873	0.213
120	1072.3	150.1	90.2	70.7	4.9	64.9	3.01	7.11	14.3	1.60	0.225
125	949.3	129.5	78.5	65.3	4.3	57.8	2.68	6.37	21.6	2.67	0.230
130	842.9	112.0	68.5	60.5	3.8	49.4	2.29	5.49	30.5	4.02	0.226
135	750.8	97.2	60.0	56.0	3.3	40.4	1.87	4.52	40.3	5.51	0.214
140	670.6	84.6	52.7	51.9	2.9	31.4	1.46	3.54	50.4	6.92	0.194
145	600.6	73.7	46.3	48.0	2.6	23.1	1.07	2.62	60.3	7.96	0.168
150	539.1	64.4	40.8	44.5	2.3	15.7	0.725	1.79	69.9	8.28	0.137
155	484.0	56.2	35.9	41.3	2.0	9.18	0.425	1.06	79.6	7.36	0.100
160	432.3	48.5	31.4	38.2	1.8	3.44	0.159	0.397	90.9	4.16	0.0533
165	383.7	43.6	28.4	36.0	1.6	1.19	0.0549	0.138	96.0	2.22	0.0230
170	344.0	38.5	25.3	33.4	1.4	0.787	0.0364	0.0920	96.5	2.36	0.0158
175	309.7	34.0	22.5	31.0	1.3	0.612	0.0283	0.0719	95.8	3.23	0.0123
180	279.2	30.1	20.0	28.7	1.1	0.497	0.0230	0.0587	93.2	6.02	0.0102
185	252.1	26.9	17.9	26.9	1.0	0.385	0.0178	0.0457	84.4	15.0	0.00809
190	228.0	24.0	16.1	25.1	0.9	0.315	0.0146	0.0376	78.6	20.9	0.00674
195	207.2	21.4	14.4	23.3	0.8	0.270	0.0125	0.0324	75.7	23.9	0.00589
200	189.1	19.1	13.0	21.7	0.7	0.238	0.0110	0.0287	74.1	25.6	0.00526

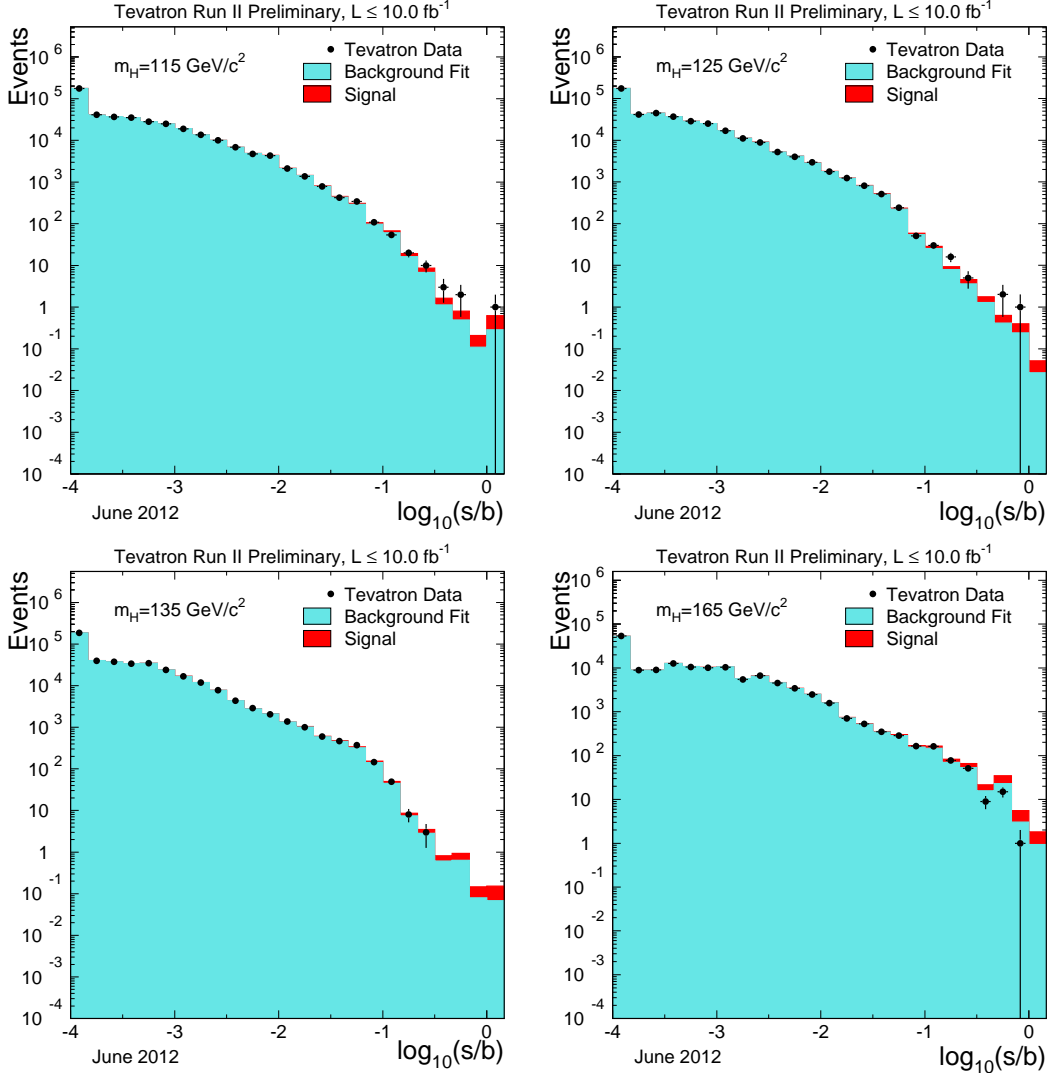


FIG. 1: Distributions of  $\log_{10}(s/b)$ , for the data from all contributing channels from CDF and D0, for Higgs boson masses of 115, 125, 135, and 165  $\text{GeV}/c^2$ . The data are shown with points, and the expected signal is shown stacked on top of the backgrounds, which have been fit to the data within their systematic uncertainties. Underflows and overflows are collected into the leftmost and rightmost bins, respectively.

is shown and also the signal expected from a Higgs boson of mass  $m_H = 120 \text{ GeV}/c^2$  is shown. The measured diboson cross section is in good agreement with the SM prediction.

## V. COMBINING CHANNELS

To gain confidence that the final result does not depend on the details of the statistical formulation, we perform two types of combinations, using Bayesian and Modified Frequentist approaches, which yield limits on the Higgs boson production rate that agree within 10% at each value of  $m_H$ , and within 1% on average. Both methods rely on

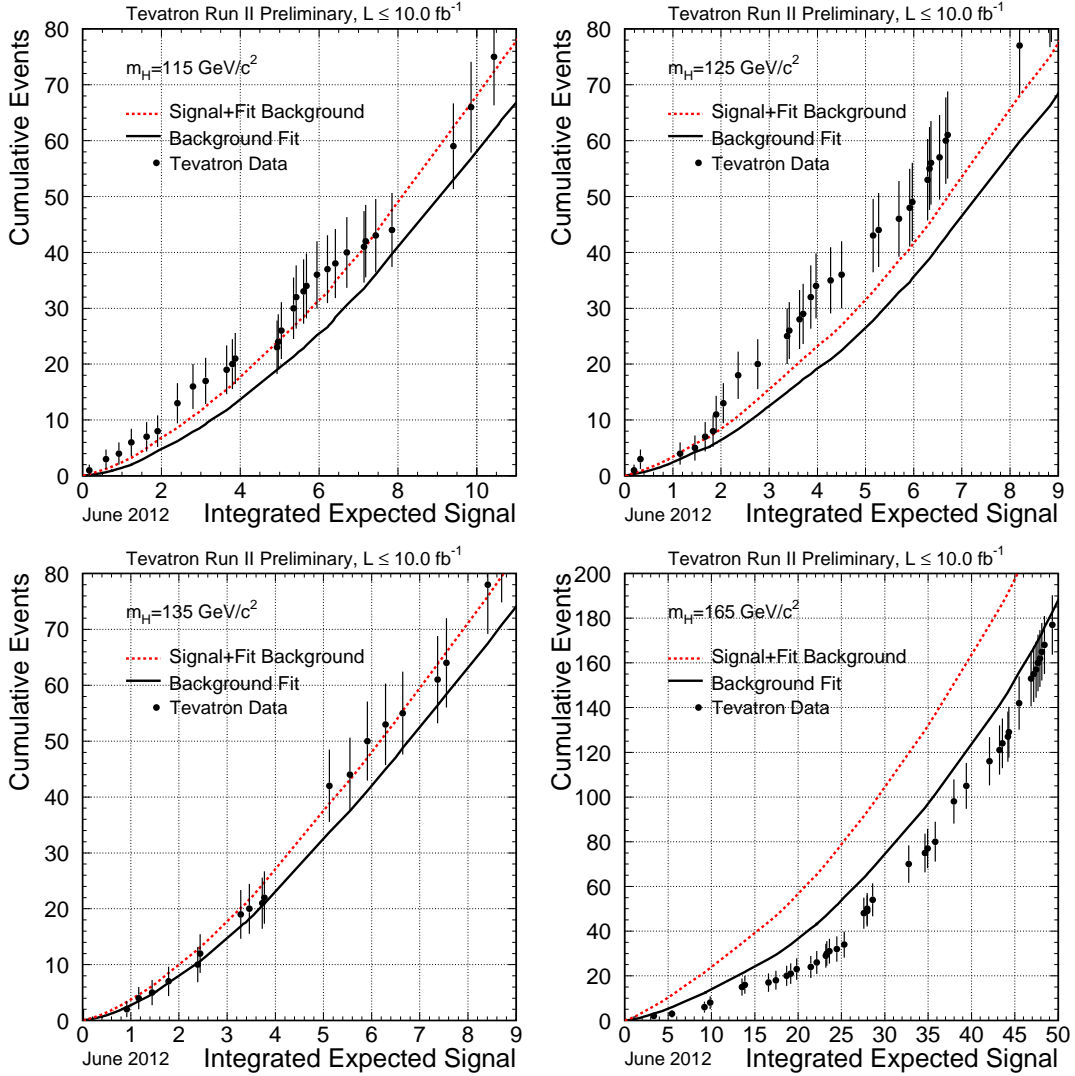


FIG. 2: Integrated distributions of  $s/b$ , starting at the high  $s/b$  side, for Higgs boson masses of 115, 125, 135, and 165  $\text{GeV}/c^2$ . The total signal+background and background-only integrals are shown separately, along with the data sums. Data are only shown for bins that have data events in them. Only the statistical errors, which are correlated point-to-point, are shown.

distributions in the final discriminants, and not just on their single integrated values. Systematic uncertainties enter on the predicted number of signal and background events as well as on the distribution of the discriminants in each analysis (“shape uncertainties”). Both methods use likelihood calculations based on Poisson probabilities.

### A. Bayesian Method

Because there is no experimental information on the production cross section for the Higgs boson, in the Bayesian technique [1] we assign a flat prior for the total number of selected Higgs boson events. For a given Higgs boson mass, the combined likelihood is a product of likelihoods for the individual channels, each of which is a product over

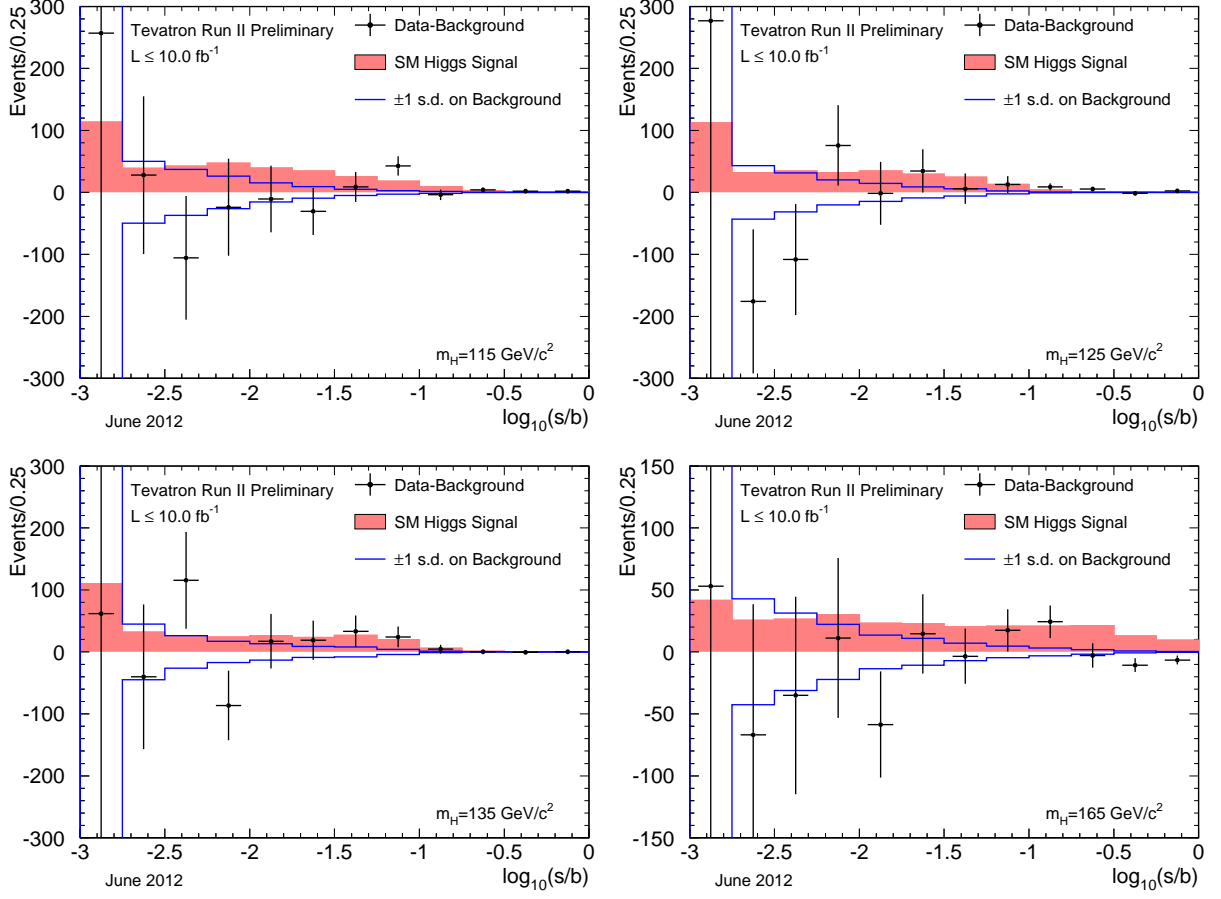


FIG. 3: Background-subtracted data distributions for all channels, summed in bins of  $s/b$ , for Higgs boson masses of 115, 125, 135, and 165  $\text{GeV}/c^2$ . The background has been fit, within its systematic uncertainties and assuming no Higgs boson signal is present, to the data. The points with error bars indicate the background-subtracted data; the sizes of the error bars are the square roots of the predicted background in each bin. The unshaded (blue-outline) histogram shows the systematic uncertainty on the best-fit background model, and the shaded histogram shows the expected signal for a standard model Higgs boson.

histogram bins:

$$\mathcal{L}(R, \vec{s}, \vec{b} | \vec{n}, \vec{\theta}) \times \pi(\vec{\theta}) = \prod_{i=1}^{N_C} \prod_{j=1}^{N_b} \mu_{ij}^{n_{ij}} e^{-\mu_{ij}} / n_{ij}! \times \prod_{k=1}^{n_{n.p}} e^{-\theta_k^2/2} \quad (1)$$

where the first product is over the number of channels ( $N_C$ ), and the second product is over  $N_b$  histogram bins containing  $n_{ij}$  events, binned in ranges of the final discriminants used for individual analyses, such as the dijet mass, neural-network outputs, or matrix-element likelihoods. The parameters that contribute to the expected bin contents are  $\mu_{ij} = R \times s_{ij}(\vec{\theta}) + b_{ij}(\vec{\theta})$  for the channel  $i$  and the histogram bin  $j$ , where  $s_{ij}$  and  $b_{ij}$  represent the expected signal and background in the bin respectively, and  $R$  is a scaling factor applied to the signal to test the sensitivity level of the experiment. Truncated Gaussian priors are used for each of the nuisance parameters  $\theta_k$ , which define the sensitivity of the predicted signal and background estimates to systematic uncertainties. These can take the form of uncertainties on overall rates, as well as the shapes of the distributions used for combination. These systematic uncertainties can

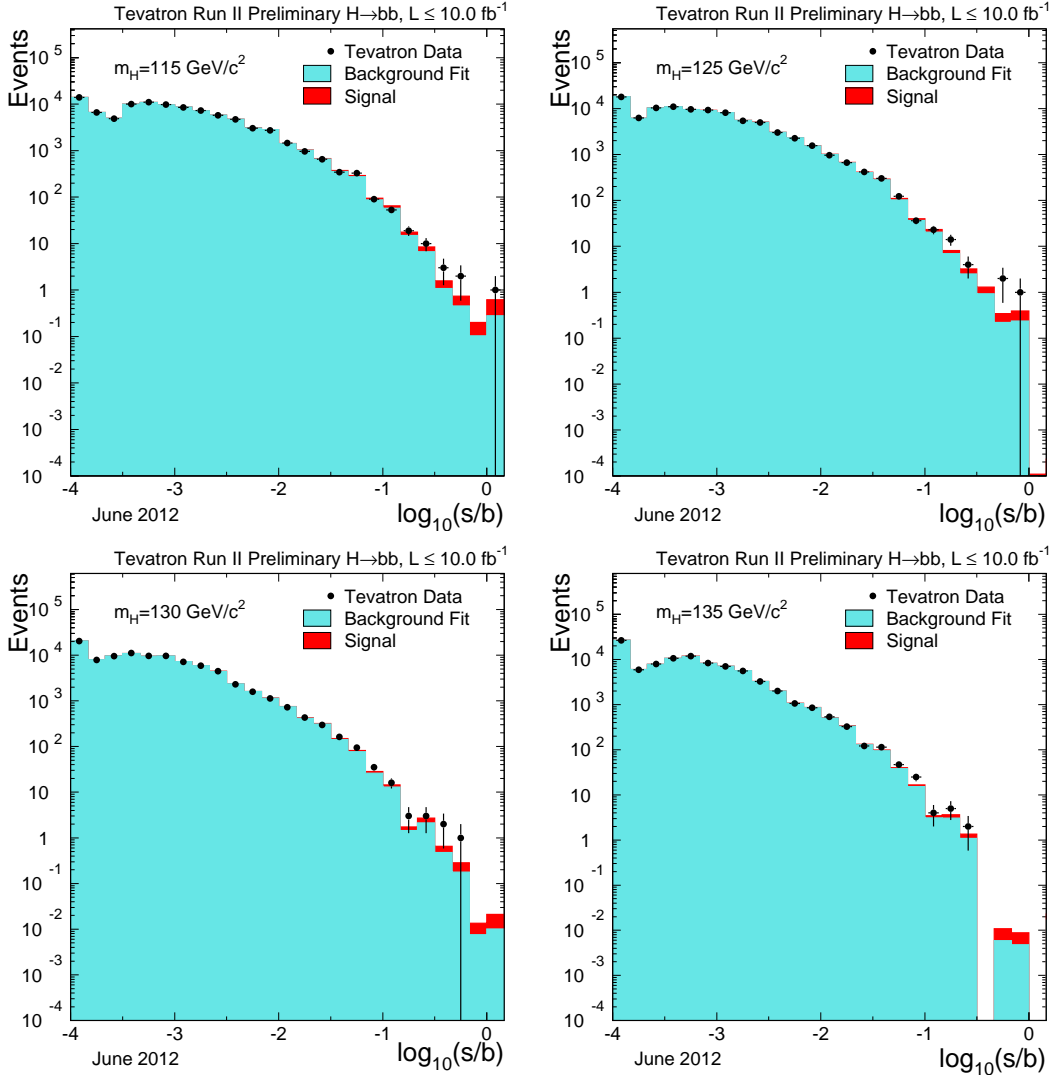


FIG. 4: Distributions of  $\log_{10}(s/b)$ , for the data from the  $WH \rightarrow \ell\nu b\bar{b}$ ,  $ZH \rightarrow \nu\bar{\nu} b\bar{b}$ , and  $ZH \rightarrow \ell^+\ell^- b\bar{b}$  searches from CDF and D0, for Higgs boson masses of 115, 125, 130, and 135  $\text{GeV}/c^2$ . The data are shown with points, and the expected signal is shown stacked on top of the backgrounds, which have been fit to the data within their systematic uncertainties. Underflows and overflows are collected into the leftmost and rightmost bins, respectively.

be far larger than the expected SM Higgs boson signal, and are therefore important in the calculation of limits. The truncation is applied so that no prediction of any signal or background in any bin is negative. The posterior density function is then integrated over all parameters (including correlations) except for  $R$ , and a 95% credibility level upper limit on  $R$  is estimated by calculating the value of  $R$  that corresponds to 95% of the area of the resulting distribution. This posterior density function is also used to estimate the best-fit value of  $R$  by finding that value which maximizes the posterior density. The fitted uncertainties are given by the shortest interval containing 68% of the integrated posterior density. These values are compared with those obtained from a profile likelihood fit to  $R$ , maximizing over the values of the nuisance parameters, and give good agreement.

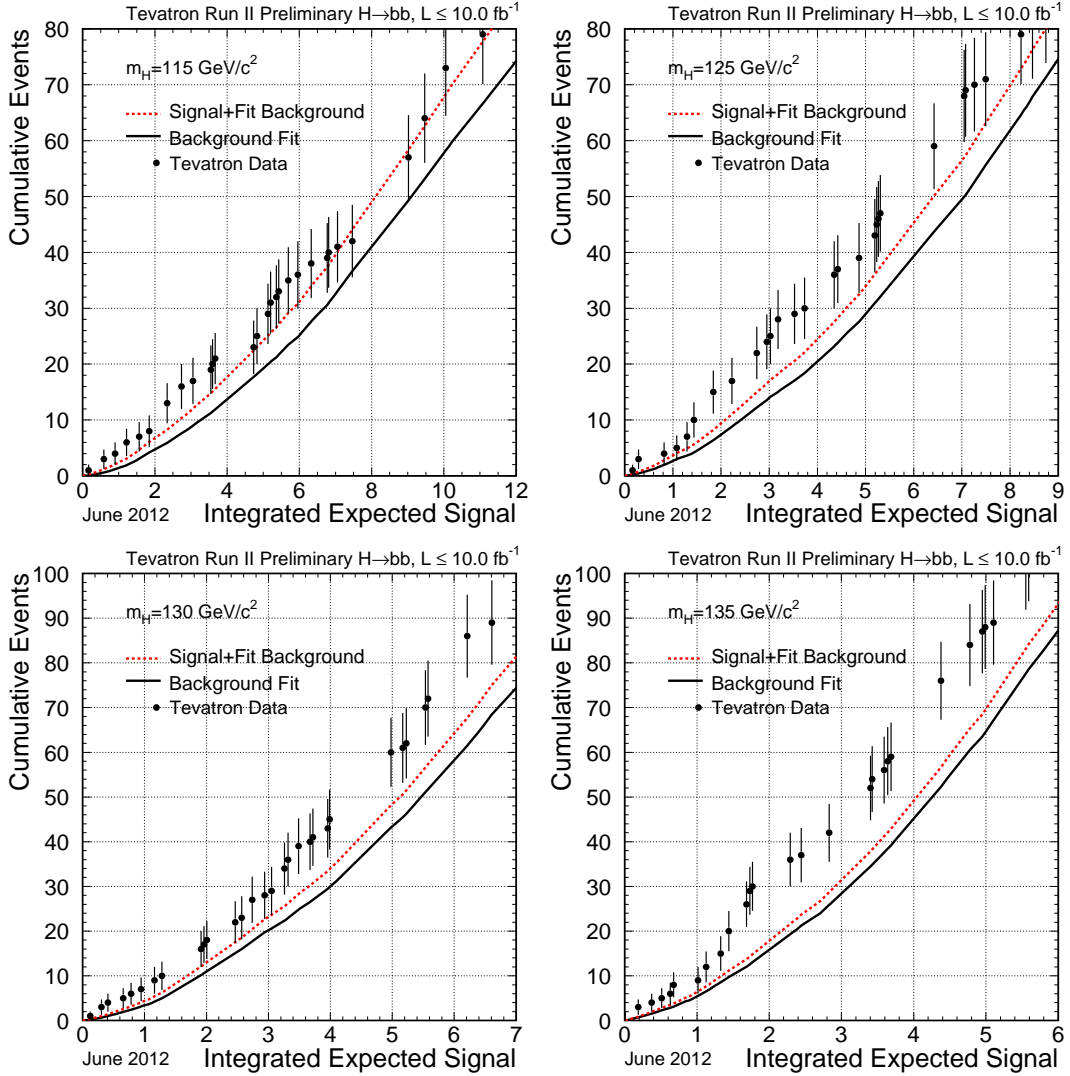


FIG. 5: Integrated distributions of  $s/b$ , starting at the high  $s/b$  side, for Higgs boson masses of 115, 125, 130, and 135  $\text{GeV}/c^2$ , for the CDF and D0  $WH \rightarrow \nu\bar{\nu}b\bar{b}$ ,  $ZH \rightarrow \nu\bar{\nu}b\bar{b}$ , and  $ZH \rightarrow \ell^+\ell^-b\bar{b}$  searches. The total signal+background and background-only integrals are shown separately, along with the data sums. Data are only shown for bins that have data events in them. Only the statistical errors, which are correlated point-to-point, are shown.

### B. Modified Frequentist Method

The Modified Frequentist technique relies on the  $\text{CL}_s$  method, using a log-likelihood ratio (LLR) as test statistic [2]:

$$LLR = -2 \ln \frac{p(\text{data}|H_1)}{p(\text{data}|H_0)}, \quad (2)$$

where  $H_1$  denotes the test hypothesis, which admits the presence of SM backgrounds and a Higgs boson signal, while  $H_0$  is the null hypothesis, for only SM backgrounds and 'data' is either an ensemble of pseudo-experiment data constructed from the expected signal and backgrounds, or the actual observed data. The probabilities  $p$  are

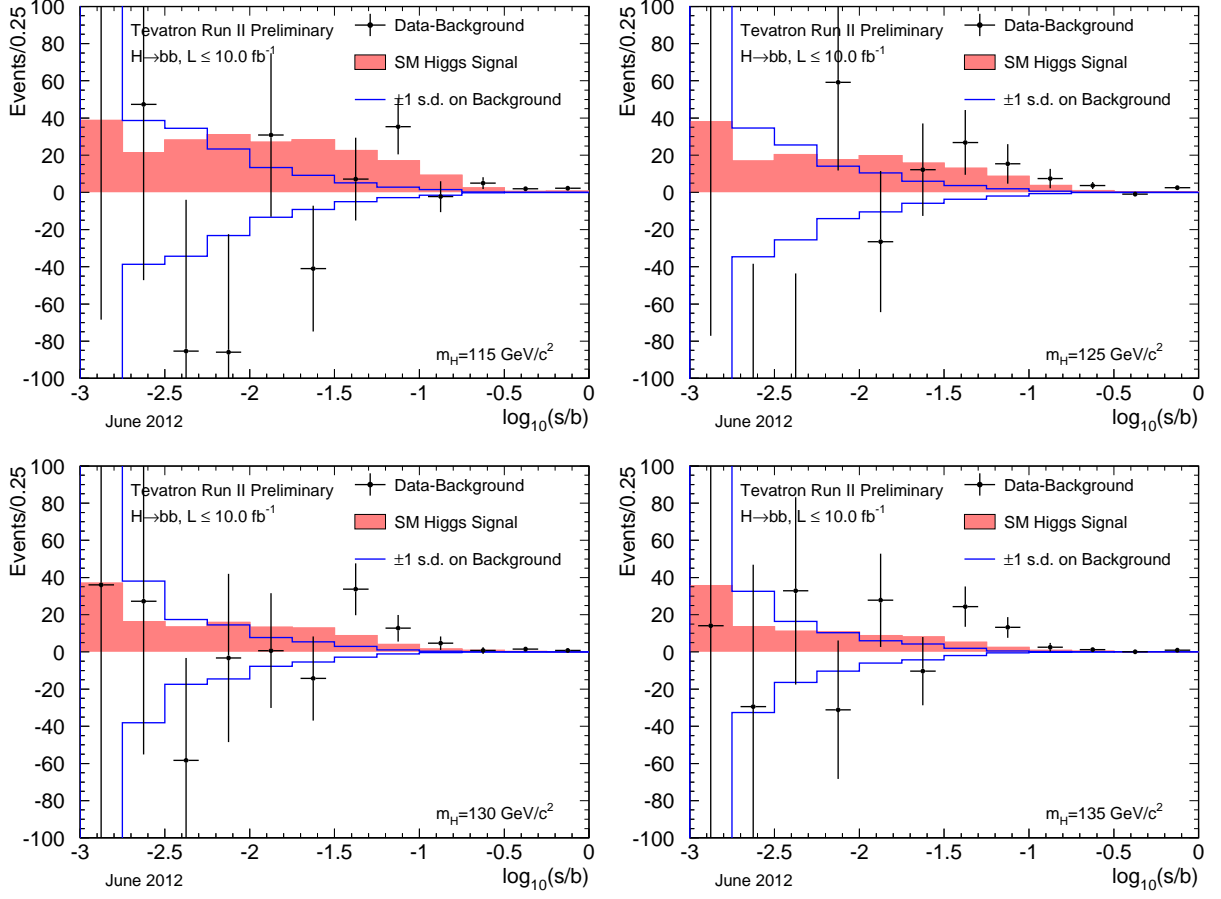


FIG. 6: Background-subtracted data distributions for all channels, summed in bins of  $s/b$ , for Higgs boson masses of 115, 125, 130, and 135  $\text{GeV}/c^2$ , for the CDF and D0  $WH \rightarrow \ell\nu b\bar{b}$ ,  $ZH \rightarrow \nu\bar{\nu}b\bar{b}$ , and  $ZH \rightarrow \ell^+\ell^-b\bar{b}$  searches. The background has been fit, within its systematic uncertainties and assuming no Higgs boson signal is present, to the data. The points with error bars indicate the background-subtracted data; the sizes of the error bars are the square roots of the predicted background in each bin. The unshaded (blue-outline) histogram shows the systematic uncertainty on the best-fit background model, and the shaded histogram shows the expected signal for a standard model Higgs boson.

computed using the best-fit values of the nuisance parameters for each pseudo-experiment, separately for each of the two hypotheses, and include the Poisson probabilities of observing the data multiplied by Gaussian priors for the values of the nuisance parameters. This technique extends the LEP procedure [82] which does not involve a fit, in order to yield better sensitivity when expected signals are small and systematic uncertainties on backgrounds are large [83].

The  $\text{CL}_s$  technique involves computing two  $p$ -values,  $\text{CL}_{s+b}$  and  $\text{CL}_b$ . The latter is defined by

$$1 - \text{CL}_b = p(LLR \leq LLR_{\text{obs}}|H_0), \quad (3)$$

where  $LLR_{\text{obs}}$  is the value of the test statistic computed for the data.  $1 - \text{CL}_b$  is the probability of observing a signal-plus-background-like outcome without the presence of signal, i.e. the probability that an upward fluctuation of the background provides a signal-plus-background-like response as observed in data. The other  $p$ -value is defined by

$$\text{CL}_{s+b} = p(LLR \geq LLR_{\text{obs}}|H_1), \quad (4)$$

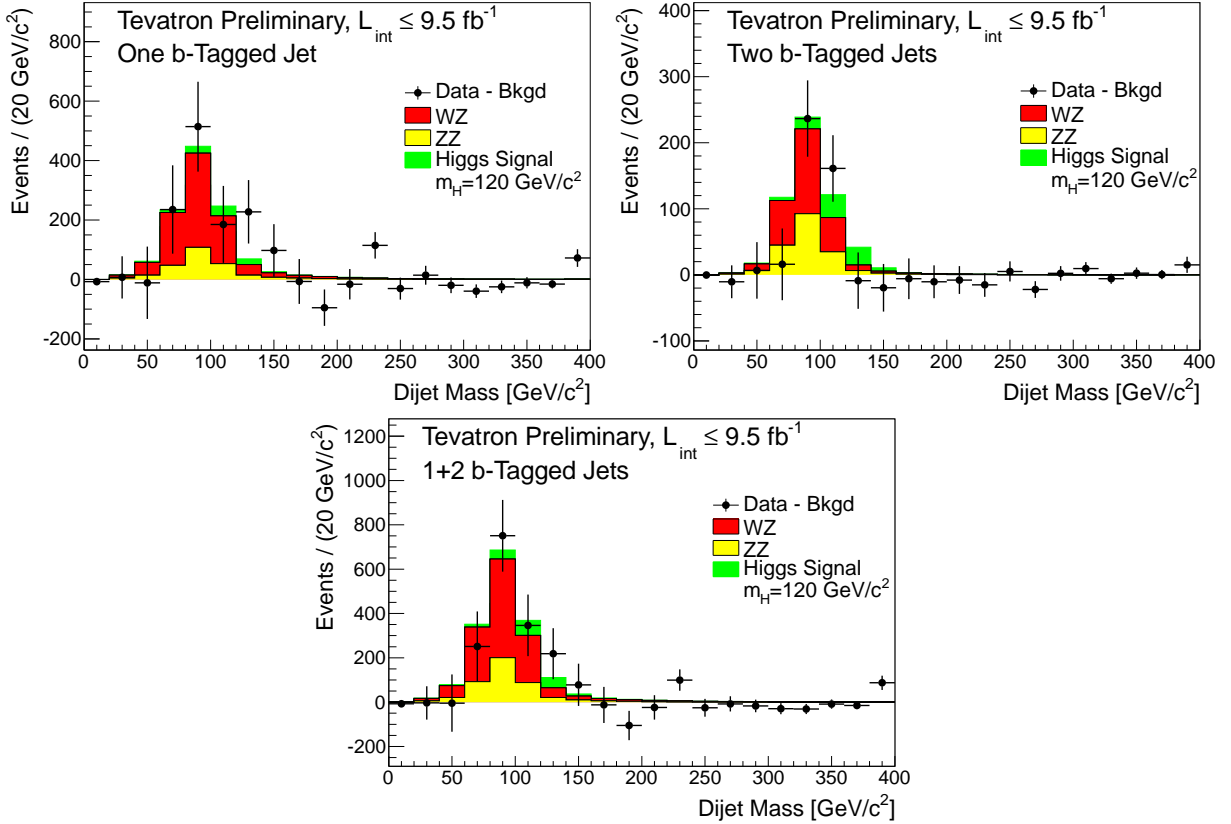


FIG. 7: Background-subtracted distributions of the reconstructed dijet mass  $m_{jj}$  for the CDF and D0  $WH \rightarrow \ell\nu b\bar{b}$ ,  $ZH \rightarrow \nu\nu b\bar{b}$ , and  $ZH \rightarrow \ell^+\ell^- b\bar{b}$  searches. The background has been fit, within its systematic uncertainties and assuming no Higgs boson signal is present, to the data. The points with error bars indicate the background-subtracted data; the sizes of the error bars are the square roots of the predicted background in each bin. The dark-shaded region shows the best-fit  $WZ + ZZ$  signal, and the lighter-shaded region shows the expectation from a Higgs boson of  $m_H = 120 \text{ GeV}/c^2$ . The three plots show the single-tagged data (top left), the double-tagged data (top right), and the sum of the two (bottom middle).

and this corresponds to the probability of a downward fluctuation of the sum of signal and background in the data. A small value of  $CL_{s+b}$  reflects inconsistency with  $H_1$ . It is also possible to have a downward fluctuation in data even in the absence of any signal, and a small value of  $CL_{s+b}$  is possible even if the expected signal is so small that it cannot be tested with the experiment. To minimize the possibility of excluding a signal to which there is insufficient sensitivity (an outcome expected 5% of the time at the 95% C.L., for full coverage), we use the quantity  $CL_s = CL_{s+b}/CL_b$ . If  $CL_s < 0.05$  for a particular choice of  $H_1$ , that hypothesis is deemed to be excluded at the 95% C.L. In an analogous way, the expected  $CL_b$ ,  $CL_{s+b}$  and  $CL_s$  values are computed from the median of the LLR distribution for the background-only hypothesis.

Systematic uncertainties are included by fluctuating the predictions for signal and background rates in each bin of each histogram in a correlated way when generating the pseudo-experiments used to compute  $CL_{s+b}$  and  $CL_b$ .

An alternate computation of the  $p$ -value  $1 - CL_b$  is to use the fitted value of  $R$  as a test statistic instead of LLR. This method is nearly as optimal as using LLR in our searches, and has been applied in the single top quark observation [84]. The background-only  $p$ -value is the probability of obtaining the fitted cross section observed in the data or more, assuming that a signal is absent. We use this method to quote our  $p$ -values and significances.



### C. Systematic Uncertainties

Systematic uncertainties differ between experiments and analyses, and they affect the rates and shapes of the predicted signal and background in correlated ways. The combined results incorporate the sensitivity of predictions to values of nuisance parameters, and include correlations between rates and shapes, between signals and backgrounds, and between channels within experiments and between experiments. More on these issues can be found in the individual analysis notes [17] through [38]. Here we discuss only the largest contributions and correlations between and within the two experiments.

#### 1. Correlated Systematics between CDF and D0

The uncertainties on the measurements of the integrated luminosities are 6% (CDF) and 6.1% (D0). Of these values, 4% arises from the uncertainty on the inelastic  $p\bar{p}$  scattering cross section, which is correlated between CDF and D0. CDF and D0 also share the assumed values and uncertainties on the production cross sections for top-quark processes ( $t\bar{t}$  and single top) and for electroweak processes ( $WW$ ,  $WZ$ , and  $ZZ$ ). In order to provide a consistent combination, the values of these cross sections assumed in each analysis are brought into agreement. We use  $\sigma_{t\bar{t}} = 7.04_{-0.36}^{+0.24}$  (scale)  $\pm 0.14$ (PDF)  $\pm 0.30$ (mass), following the calculation of Moch and Uwer [85], assuming a top quark mass  $m_t = 173.1 \pm 1.2$  GeV/ $c^2$  [53], and using the MSTW2008nnlo PDF set [60]. Other calculations of  $\sigma_{t\bar{t}}$  are similar [86].

For single top, we use the approximate next-to-next-to-next-to-leading-order (NNNLOapprox) with next-to-leading logarithmic (NLL) resummation of soft gluons calculation of the  $t$ -channel production cross section of Kidonakis [87], which has been updated using the MSTW2008nnlo PDF set [60] [88]. For the  $s$ -channel process we use [89], again based on the MSTW2008nnlo PDF set. Both of the cross section values below are the sum of the single  $t$  and single  $\bar{t}$  cross sections, and both assume  $m_t = 173.1 \pm 1.2$  GeV/ $c^2$ .

$$\sigma_{t\text{-chan}} = 2.10 \pm 0.027 \text{ (scale)} \pm 0.18 \text{ (PDF)} \pm 0.045 \text{ (mass) pb.} \quad (5)$$

$$\sigma_{s\text{-chan}} = 1.05 \pm 0.01 \text{ (scale)} \pm 0.06 \text{ (PDF)} \pm 0.03 \text{ (mass) pb.} \quad (6)$$

Other calculations of  $\sigma_{\text{SingleTop}}$  are similar for our purposes [90].

MCFM [47] has been used to compute the NLO cross sections for  $WW$ ,  $WZ$ , and  $ZZ$  production [91]. Using a scale choice  $\mu_0 = M_V^2 + p_T^2(V)$  and the MSTW2008 PDF set [60], the cross section for inclusive  $W^+W^-$  production is

$$\sigma_{W^+W^-} = 11.34_{-0.49}^{+0.56} \text{ (scale)}_{-0.28}^{+0.35} \text{ (PDF) pb} \quad (7)$$

and the cross section for inclusive  $W^\pm Z$  production is

$$\sigma_{W^\pm Z} = 3.22_{-0.17}^{+0.20} \text{ (scale)}_{-0.08}^{+0.11} \text{ (PDF) pb} \quad (8)$$

The calculation is done using  $Z \rightarrow \ell^+\ell^-$  and therefore necessarily includes contributions from  $\gamma^* \rightarrow \ell^+\ell^-$ . The cross sections quoted above have the requirement  $75 \leq m_{\ell^+\ell^-} \leq 105$  GeV/ $c^2$  for the leptons from the neutral current exchange. The same dilepton invariant mass requirement is applied to both sets of leptons in determining the  $ZZ$  cross section which is

$$\sigma_{ZZ} = 1.20_{-0.04}^{+0.05} \text{ (scale)}_{-0.03}^{+0.04} \text{ (PDF) pb} \quad (9)$$

For the diboson cross section calculations,  $|\eta_\ell| < 5$  for all calculations. Loosening this requirement to include all leptons leads to  $\sim +0.4\%$  change in the predictions. Lowering the factorization and renormalization scales by a factor of two increases the cross section, and raising the scales by a factor of two decreases the cross section. The PDF uncertainty has the same fractional impact on the predicted cross section independent of the scale choice. All PDF uncertainties are computed as the quadrature sum of the twenty 68% C.L. eigenvectors provided with MSTW2008 (MSTW2008nlo68cl).

In many analyses, the dominant background yields are calibrated with data control samples. Since the methods of measuring the multijet (“QCD”) backgrounds differ between CDF and D0, and even between analyses within the collaborations, there is no correlation assumed between these rates. Similarly, the large uncertainties on the background rates for  $W$ +heavy flavor (HF) and  $Z$ +heavy flavor are considered at this time to be uncorrelated. The calibrations of fake leptons, unvetoes  $\gamma \rightarrow e^+e^-$  conversions,  $b$ -tag efficiencies and mistag rates are performed by each collaboration using independent data samples and methods, and are therefore also treated as uncorrelated.

### 2. Correlated Systematic Uncertainties for CDF

The dominant systematic uncertainties for the CDF analyses are shown in the Appendix in Tables XI and X for the  $WH \rightarrow \ell\nu b\bar{b}$  channels, in Table XIV for the  $WH, ZH \rightarrow \cancel{E}_T b\bar{b}$  channels, in Tables XVI and XVII for the  $ZH \rightarrow \ell^+\ell^-b\bar{b}$  channels, in Tables XIX, XX, and XXI for the  $H \rightarrow W^+W^- \rightarrow \ell'^{\pm}\nu\ell'^{\mp}\nu$  channels, in Table XXII for the  $WH \rightarrow WWW \rightarrow \ell'^{\pm}\ell'^{\pm}$  and  $WH \rightarrow WWW \rightarrow \ell'^{\pm}\ell'^{\pm}\ell''^{\mp}$  channels, in Table XXIII for the  $ZH \rightarrow ZWW \rightarrow \ell^{\pm}\ell^{\mp}\ell'^{\pm}$  channels, in Table XXX for the  $H \rightarrow 4\ell$  channel, in Tables XXXI, XXXII, and XXXIII for the  $t\bar{t}H \rightarrow W^+bW^-b\bar{b}$  channels, in Table XXXIV for the  $H \rightarrow \tau^+\tau^-$  channels, in Table XXXV for the  $WH \rightarrow \ell\nu\tau^+\tau^-$  and  $ZH \rightarrow \ell^+\ell^-\tau^+\tau^-$  channels, in Table XXXVI for the  $WH/ZH$  and  $VBF \rightarrow jjb\bar{b}$  channels, and in Table XXXVII for the  $H \rightarrow \gamma\gamma$  channel. Each source induces a correlated uncertainty across all CDF channels’ signal and background contributions which are sensitive to that source. For  $H \rightarrow b\bar{b}$ , the largest uncertainties on signal arise from measured  $b$ -tagging efficiencies, jet energy scale, and other Monte Carlo modeling. Shape dependencies of templates on jet energy scale,  $b$ -tagging, and gluon radiation (“ISR” and “FSR”) are taken into account for some analyses (see tables). For  $H \rightarrow W^+W^-$ , the largest uncertainties on signal acceptance originate from Monte Carlo modeling. Uncertainties on background event rates vary significantly for the different processes. The backgrounds with the largest systematic uncertainties are in general quite small. Such uncertainties are constrained by fits to the nuisance parameters, and they do not affect the result significantly. Because the largest background contributions are measured using data, these uncertainties are treated as uncorrelated for the  $H \rightarrow b\bar{b}$  channels. The differences in the resulting limits when treating the remaining uncertainties as either correlated or uncorrelated is less than 5%.

### 3. Correlated Systematic Uncertainties for D0

The dominant systematic uncertainties for the D0 analyses are shown in the Appendix, in Tables XII, XIII, XV, XVIII, XXIV, XXV, XXVI, XXVIII, XXVII, XXIX, and XXXVIII. Each source induces a correlated uncertainty across all D0 channels sensitive to that source. Wherever appropriate the impact of systematic effects on both the rate and shape of the predicted signal and background is included. For the low mass,  $H \rightarrow b\bar{b}$  analyses, significant sources of uncertainty include the measured  $b$ -tagging rate and the normalization of the  $W$  and  $Z$  plus heavy flavor backgrounds. For the  $H \rightarrow W^+W^-$  and  $VH \rightarrow leptons + X$  analyses, significant sources of uncertainty are the measured efficiencies for selecting leptons. For analyses involving jets the determination of the jet energy scale, jet resolution and the multijet background contribution are significant sources of uncertainty. Significant sources for all analyses are the uncertainties on the luminosity and the cross sections for the simulated backgrounds. All systematic uncertainties arising from the same source are taken to be correlated among the different backgrounds and between signal and background.

## VI. COMBINED RESULTS

Before extracting the combined limits we study the distributions of the log-likelihood ratio (LLR) for different hypotheses to quantify the expected sensitivity across the mass range tested. Figure 8 and Table VII display the LLR distributions for the combined analyses as functions of  $m_H$ . Included are the median of the LLR distributions for

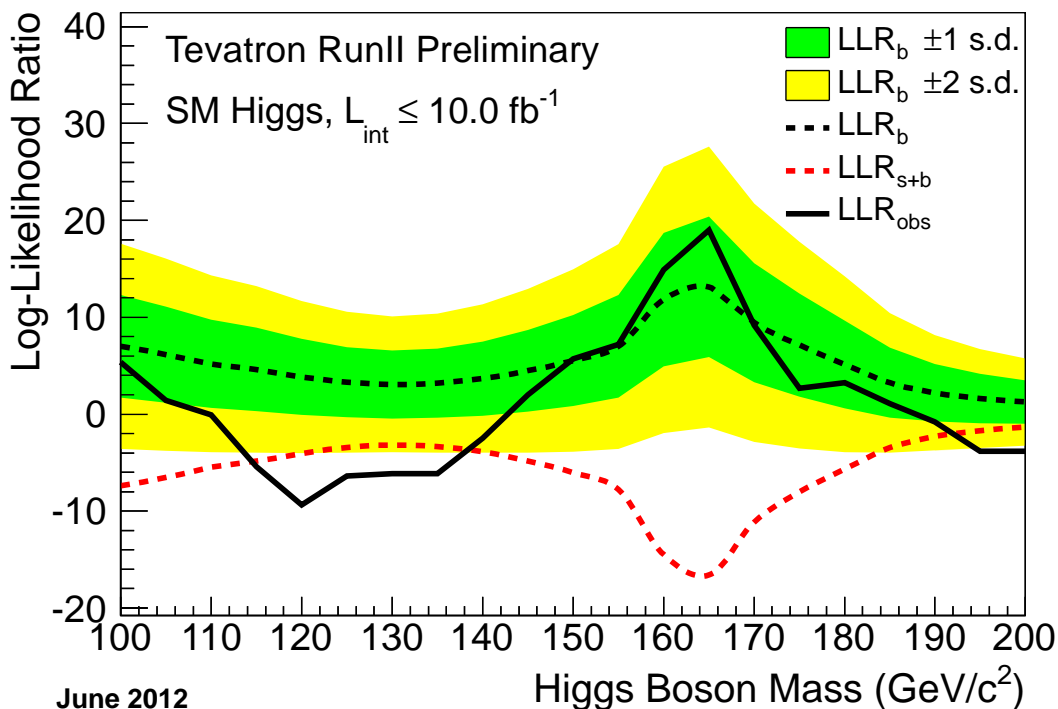


FIG. 8: Distributions of the log-likelihood ratio (LLR) as a function of Higgs boson mass obtained with the  $CL_s$  method for the combination of all CDF and D0 analyses. The thick black curve shows the outcome from the observed data. The green and yellow bands correspond to the regions enclosing 1 s.d. and 2 s.d. fluctuations around the median expected value assuming only background is present, respectively. The red dashed curve shows the median expected value assuming a Higgs boson signal is present, separately at each  $m_H$ .

the background-only hypothesis ( $LLR_b$ ), the signal-plus-background hypothesis ( $LLR_{s+b}$ ), and the observed value for the data ( $LLR_{obs}$ ). The shaded bands represent the one and two s.d. departures for  $LLR_b$  centered on the median. The separation between the medians of the  $LLR_b$  and  $LLR_{s+b}$  distributions provides a measure of the discriminating power of the search. The sizes of the one- and two-s.d.  $LLR_b$  bands indicate the width of the  $LLR_b$  distribution, assuming no signal is truly present and only statistical fluctuations and systematic effects are present. The value of  $LLR_{obs}$  relative to  $LLR_{s+b}$  and  $LLR_b$  indicates whether the data distribution appears to resemble what we expect if a signal is present (i.e. closer to the  $LLR_{s+b}$  distribution, which is negative by construction) or whether it resembles the background expectation more closely; the significance of departures of  $LLR_{obs}$  from  $LLR_b$  can be evaluated by the width of the  $LLR_b$  bands. The data are consistent with the prediction of the background-only hypothesis (the black dashed line) above  $\sim 145$   $GeV/c^2$ , except above  $\sim 190$   $GeV/c^2$  where our ability to separate the two hypotheses is very limited. For  $m_H$  from 110 to 140  $GeV/c^2$ , an excess in the data has an amplitude consistent with the expectation for a standard model Higgs boson in this mass range (dashed red line). In this region our ability to distinguish the signal-plus-background and background-only hypotheses is, as indicated by the separation of the  $LLR_{s+b}$  and  $LLR_b$  values, at the 2 s.d. level.

Motivated both by the excess in the data in the low- $m_H$  region of our searches, we compare the observed LLR with that expected if a SM Higgs boson were present with a mass  $m_H = 125$   $GeV/c^2$ . Figure 9 shows the same median expectation curves as Figure 8, but in the place of the data, the median expected LLR assuming a Higgs boson signal is present at  $m_H = 125$   $GeV/c^2$  is shown. While the search for a 125  $GeV/c^2$  Higgs boson is the most optimized to find a Higgs boson of that mass, the excess of events over the SM background estimates also affect the results of Higgs boson searches at other masses. Nearby masses are the most affected, but the expected presence of  $H \rightarrow W^+W^-$  decays for a 125  $GeV/c^2$  Higgs boson implies a small expected excess in the  $H \rightarrow W^+W^-$  searches at all masses due

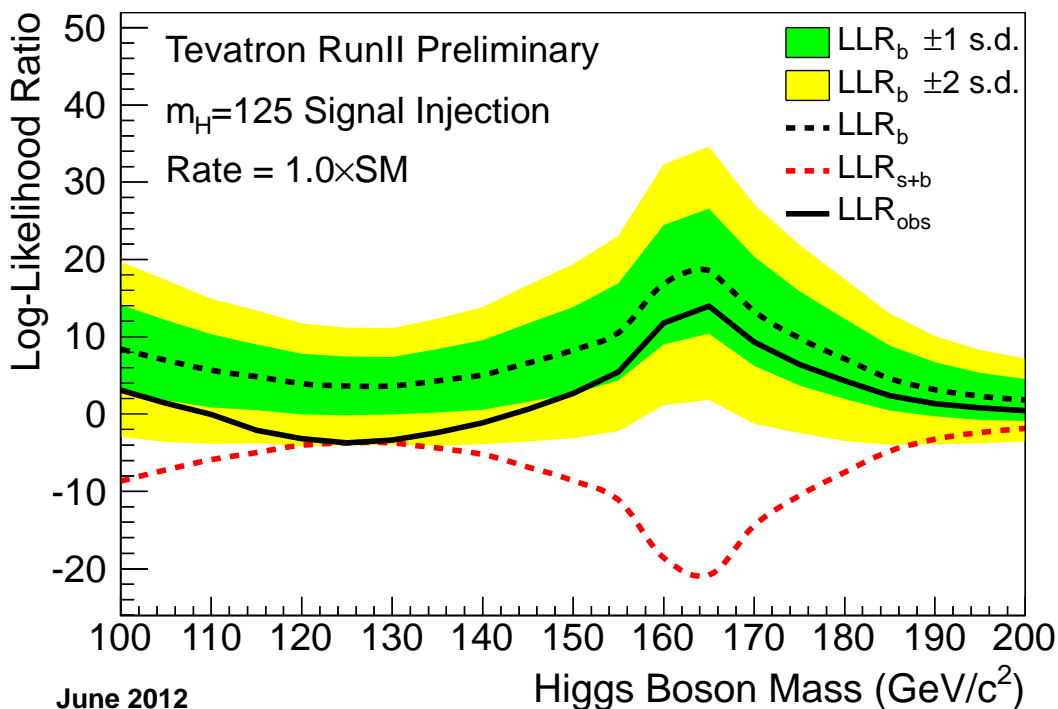


FIG. 9: The log-likelihood ratio (LLR) distributions as in Figure 8. The thick black curve shows the median expected outcome assuming a Higgs boson of mass  $m_H = 125 \text{ GeV}/c^2$  is present. The green and yellow bands correspond to the regions enclosing 1 s.d. and 2 s.d. fluctuations around the median expected value assuming only background is present, respectively. The red dashed curve shows the median expected value assuming a Higgs boson signal is present, separately at each  $m_H$ .

to the poor reconstructed mass resolution of the  $H \rightarrow W^+W^-$  searches.

Using the combination procedures outlined in Section III, we extract limits on the SM Higgs boson production  $\sigma \times B(H \rightarrow X)$  in  $p\bar{p}$  collisions at  $\sqrt{s} = 1.96 \text{ TeV}$  for  $100 \leq m_H \leq 200 \text{ GeV}/c^2$ . To facilitate comparisons with the standard model and to accommodate analyses with different degrees of sensitivity and acceptance for more than one signal production mechanism, we present our resulting limit divided by the SM Higgs boson production cross section,  $\sigma_{SM}$ , as a function of Higgs boson mass, for test masses for which both experiments have performed dedicated searches in different channels i.e. we introduce a signal strength modifier,  $R = \sigma/\sigma_{SM}$ . A value of the combined limit ratio which is less than or equal to one indicates that that particular Higgs boson mass is excluded at the 95% C.L.

The combinations of results [1, 2] of each single experiment, as used in this Tevatron combination, yield the following ratios of 95% C.L. observed (expected) limits to the SM cross section: 2.37 (1.16) for CDF and 2.11 (1.46) for D0 at  $m_H = 115 \text{ GeV}/c^2$ , 2.90 (1.41) for CDF and 2.94 (1.70) for D0 at  $m_H = 125 \text{ GeV}/c^2$ , and 0.42 (0.69) for CDF and 0.73 (0.72) for D0 at  $m_H = 165 \text{ GeV}/c^2$ .

The ratios of the 95% C.L. expected and observed limit to the SM cross section are shown in Figure 10 for the combined CDF and D0 analyses. The observed and median expected ratios are listed for the tested Higgs boson masses in Table IV for  $m_H \leq 150 \text{ GeV}/c^2$ , and in Table V for  $m_H \geq 155 \text{ GeV}/c^2$ , as obtained by the Bayesian and the  $CL_s$  methods. In the following summary we quote only the limits obtained with the Bayesian method, which was decided upon *a priori*. The corresponding limits and expected limits obtained using the  $CL_s$  method are shown alongside the Bayesian limits in the tables. We obtain the observed (expected) values of 1.07 (0.78) at  $m_H = 105 \text{ GeV}/c^2$ , 1.74 (0.89) at  $m_H = 115 \text{ GeV}/c^2$ , 2.35 (1.08) at  $m_H = 125 \text{ GeV}/c^2$ , 1.14 (0.91) at  $m_H = 145 \text{ GeV}/c^2$ , 0.34 (0.48) at  $m_H = 165 \text{ GeV}/c^2$ , and 1.32 (1.06) at  $m_H = 185 \text{ GeV}/c^2$ .

We choose to use the intersections of piecewise linear interpolations of our observed and expected rate limits in order to quote ranges of Higgs boson masses that are excluded and that are expected to be excluded. The sensitivities

of our searches to Higgs bosons are smooth functions of the Higgs boson mass and depend most strongly on the predicted cross sections and the decay branching ratios (the decay  $H \rightarrow W^+W^-$  is the dominant decay for the region of highest sensitivity). We therefore use the linear interpolations to extend the results from the  $5 \text{ GeV}/c^2$  mass points investigated to the intervals in between. The regions of Higgs boson masses excluded at the 95% C.L. thus obtained are  $100 < m_H < 103 \text{ GeV}/c^2$  and  $147 < m_H < 180 \text{ GeV}/c^2$ . The expected exclusion regions are, given the current sensitivity,  $100 < m_H < 120 \text{ GeV}/c^2$  and  $139 < m_H < 184 \text{ GeV}/c^2$ . Higgs boson masses below  $100 \text{ GeV}/c^2$  were not studied. We also show in Figure 11, and list in Table VIII, the observed values of  $1 - \text{CL}_s$  and their expected distributions for the background-only hypothesis as functions of the Higgs boson mass. The excluded regions obtained by finding the intersections of the linear interpolations of the observed  $1 - \text{CL}_s$  curve are nearly identical to those obtained with the Bayesian calculation.

Figure 12 shows the  $p$ -value  $\text{CL}_{s+b}$  as a function of  $m_H$  as well as the expected distributions in the absence of a Higgs boson signal. Figure 13 shows the  $p$ -value  $1 - \text{CL}_b$  as a function of  $m_H$ , i.e., the probability that an upward

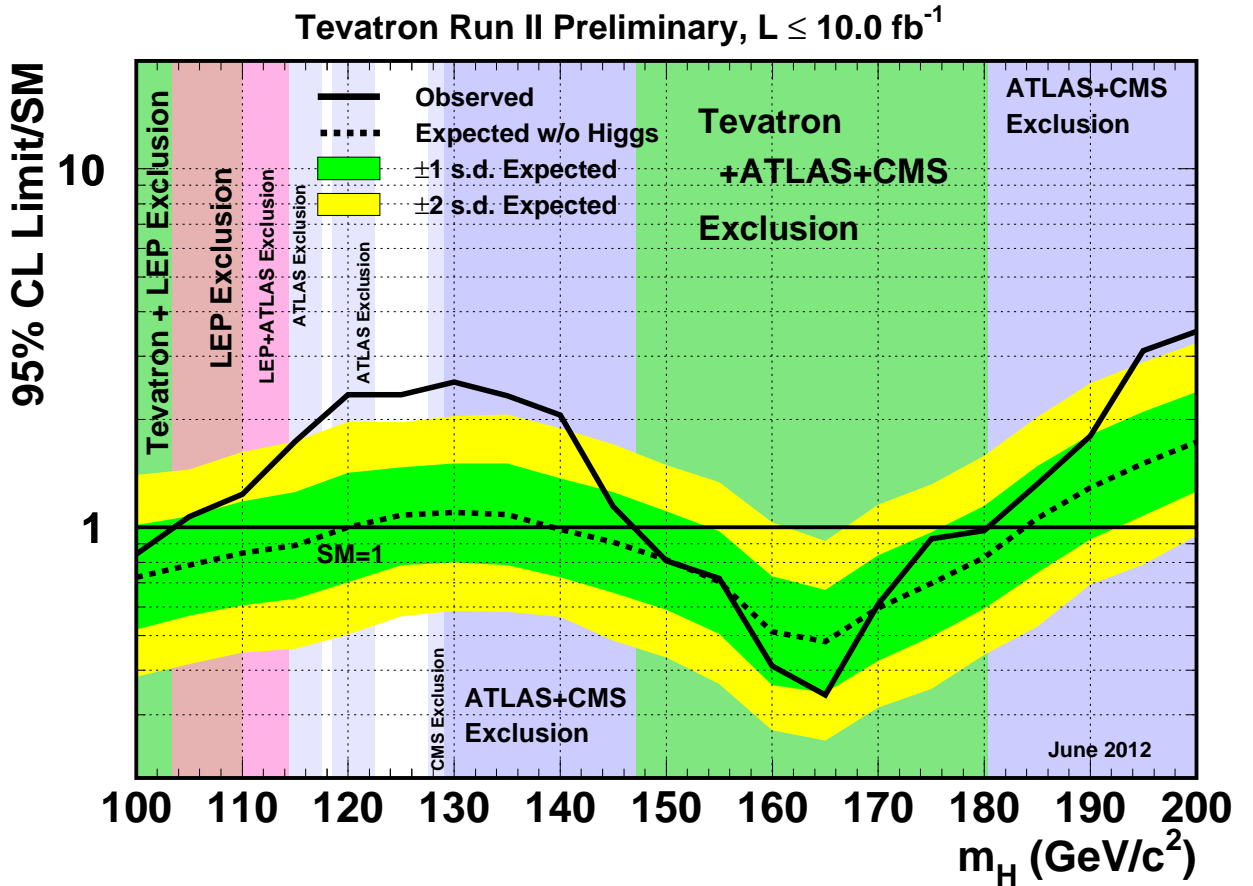


FIG. 10: Observed and expected (median, for the background-only hypothesis) 95% C.L. upper limits on the ratios to the SM cross section, as functions of the Higgs boson mass for the combined CDF and D0 analyses. The limits are expressed as a multiple of the SM prediction for test masses (every  $5 \text{ GeV}/c^2$ ) for which both experiments have performed dedicated searches in different channels. The points are joined by straight lines for better readability. The bands indicate the 68% and 95% probability regions where the limits can fluctuate, in the absence of signal. The limits displayed in this figure are obtained with the Bayesian calculation.

TABLE IV: Ratios of median expected and observed 95% C.L. limit to the SM cross section for the combined CDF and D0 analyses as a function of the Higgs boson mass in  $\text{GeV}/c^2$ , obtained with the Bayesian and with the  $\text{CL}_s$  method.

Bayesian	100	105	110	115	120	125	130	135	140	145	150
Expected	0.73	0.78	0.85	0.89	1.00	1.08	1.10	1.09	0.99	0.91	0.81
Observed	0.84	1.07	1.24	1.74	2.35	2.35	2.55	2.33	2.06	1.14	0.81
$\text{CL}_s$	100	105	110	115	120	125	130	135	140	145	150
Expected	0.73	0.78	0.85	0.91	1.00	1.08	1.12	1.10	1.02	0.92	0.82
Observed	0.80	1.08	1.26	1.86	2.49	2.42	2.57	2.46	1.94	1.13	0.80

TABLE V: Ratios of median expected and observed 95% C.L. limit to the SM cross section for the combined CDF and D0 analyses as a function of the Higgs boson mass in  $\text{GeV}/c^2$ , obtained with the Bayesian and with the  $\text{CL}_s$  method.

Bayesian	155	160	165	170	175	180	185	190	195	200
Expected	0.71	0.51	0.48	0.60	0.70	0.83	1.06	1.29	1.51	1.73
Observed	0.72	0.41	0.34	0.61	0.93	0.98	1.32	1.80	3.11	3.53
$\text{CL}_s$	155	160	165	170	175	180	185	190	195	200
Expected	0.72	0.52	0.49	0.60	0.71	0.85	1.09	1.34	1.58	1.80
Observed	0.68	0.41	0.33	0.59	0.94	0.98	1.37	1.94	3.25	3.88

fluctuation of the background can give an outcome as signal-like as the data or more. Table IX lists the observed  $p$ -values as a function of  $m_H$ . In the absence of a Higgs boson signal, the observed  $p$ -value is expected to be uniformly distributed between 0 and 1. A small  $p$ -value indicates that the data are not easily explained by the background-only hypothesis, and that the data prefer the signal-plus-background prediction. Our sensitivity to a Higgs boson with a mass of  $165 \text{ GeV}/c^2$  is such that we would expect to see a  $p$ -value corresponding to  $\sim 4$  s.d. in half of the experimental outcomes. The smallest observed  $p$ -value corresponds to a Higgs boson mass of  $120 \text{ GeV}/c^2$ . The fluctuations seen in the observed  $p$ -value as a function of the tested  $m_H$  result from excesses seen in different search channels, as well as from point-to-point fluctuations due to the separate discriminants at each  $m_H$ , and are discussed in more detail below. The width of the dip in the  $p$ -values from  $115$  to  $135 \text{ GeV}/c^2$  is consistent with the resolution of the combination of the  $H \rightarrow b\bar{b}$  and  $H \rightarrow W^+W^-$  channels. The effective resolution of this search comes from two independent sources of information. The reconstructed candidate masses help constrain  $m_H$ , but more importantly, the expected cross sections times the relevant branching ratios for the  $H \rightarrow b\bar{b}$  and  $H \rightarrow W^+W^-$  channels are strong functions of  $m_H$  in the SM. The observed excesses in the  $H \rightarrow b\bar{b}$  channels coupled with a more background-like outcome in the  $H \rightarrow W^+W^-$  channels determines the shape of the observed  $p$ -value as a function of  $m_H$ .

We perform a fit of the signal-plus-background hypothesis to the observed data, allowing the signal strength modifier to vary as a function of  $m_H$ . The resulting best-fit signal strength (modifier) is shown in Figure 14, and listed in Table VI. The signal strength is within 1 s.d. of the SM expectation with a Higgs boson signal in the range  $110 < m_H < 140 \text{ GeV}/c^2$ . The largest signal fit in this range, normalized to the SM prediction, is obtained at  $130 \text{ GeV}/c^2$ . The reason the highest signal strength is at  $130 \text{ GeV}/c^2$  while the smallest  $p$ -value from Figure 13 is at  $120 \text{ GeV}/c^2$  is because a signal at  $120 \text{ GeV}/c^2$  would have a higher cross section than a signal at  $130 \text{ GeV}/c^2$ , and since the resolution of the discriminants cannot distinguish very well a mass difference of this size, a signal at  $120 \text{ GeV}/c^2$  would be similar to a signal at  $130 \text{ GeV}/c^2$  with a larger scale factor for the predicted cross section. Figure 15 shows the posterior density for the cross section computed using the Bayesian technique at  $m_H = 125 \text{ GeV}/c^2$ .

We also investigate combinations of CDF and D0 searches based on the  $H \rightarrow b\bar{b}$  and  $H \rightarrow W^+W^-$  decay modes. Below  $125 \text{ GeV}/c^2$ , the  $H \rightarrow b\bar{b}$  searches contribute the majority of our sensitivity. The  $WH \rightarrow \ell\nu b\bar{b}$ ,  $ZH \rightarrow \nu\bar{\nu} b\bar{b}$ , and  $ZH \rightarrow \ell^+\ell^- b\bar{b}$  channels from both experiments are included in this combination. The result is shown in Figure 16. The distribution of the LLR demonstrates the compatibility of the observed data with both the background-only and

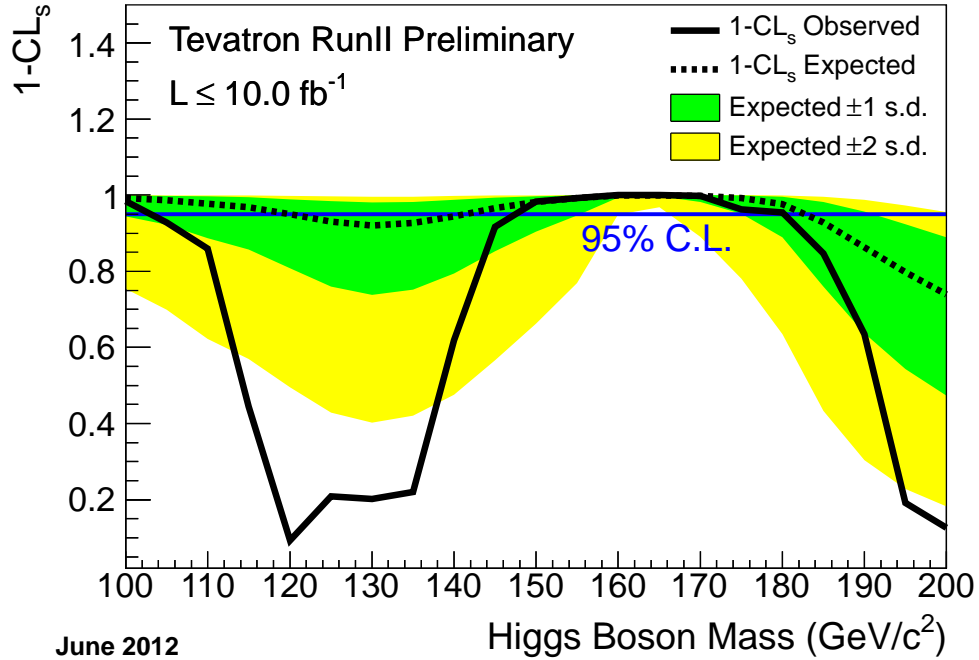


FIG. 11: The exclusion strength  $1-CL_s$  as a function of the Higgs boson mass (in steps of  $5 \text{ GeV}/c^2$ ), for the combination of the CDF and D0 analyses. The green and yellow bands correspond to the regions enclosing 1 s.d. and 2 s.d. fluctuations around the median predicted value in the background-only hypothesis, respectively.

signal-plus-background hypotheses, and is shown in Figure 17. An interesting feature of this graph is that as  $m_H$  increases towards the high end of the range shown,  $Br(H \rightarrow b\bar{b})$  falls rapidly, and the expected signal yield becomes small. Thus LLR approaches zero as  $m_H$  gets larger, independent of the experimental outcome. This feature can also be seen with the shaded bands which also converge on zero at high  $m_H$ . If there is a broad excess in the  $H \rightarrow b\bar{b}$  searches, then LLR will fall to a minimum value and rise again.

Figure 18 shows the observed and expected values of  $CL_{s+b}$  as functions of  $m_H$ . Figure 19 shows the  $p$ -value for the background-only hypothesis  $1 - CL_b$ , which represents the probability for the background to fluctuate to produce an outcome as signal-like as the observed data or more. As with Figure 17, a broad deviation is seen. The smallest  $p$ -value within the mass range where these searches are performed,  $100 < m_H < 150 \text{ GeV}/c^2$ , is  $\sim 8.06 \times 10^{-4}$  and corresponds to a significance of 3.2 s.d. Table IX lists the observed  $p$ -values and local significances for the  $H \rightarrow b\bar{b}$  searches as functions of  $m_H$ .

These probabilities do not include the look-elsewhere effect (LEE), and are thus local  $p$ -values, corresponding to searches at each value of  $m_H$  separately. The LEE accounts for the probability of observing an upwards fluctuation of the background at any of the tested values of  $m_H$  in our search region, at least as significant as the one observed at the value of  $m_H$  with the most significant local excess. A simple and correct method of calculating the LEE, and thus the global significance of the excess, is to simulate many possible experimental outcomes assuming the absence of a signal, and for each one, compute the LLR and the fitted cross section curves as functions of  $m_H$  and find the deviation with the smallest background-only-hypothesis  $p$ -value. Using this minimum  $p$ -value as a test statistic, another  $p$ -value is then computed, which is the probability of observing that minimum  $p$ -value or less. This method is difficult to pursue in the Tevatron Higgs boson searches due to the fact that in most of the analyses, a distinct multivariate analysis (MVA) discriminant function is trained for each value of  $m_H$  that is tested. This step is an important optimization, because the kinematic distributions and signal branching ratios are functions of  $m_H$ , but it introduces the difficulty of running the same set of simulated events separately through many MVA functions in order to compute the LEE with the simple method. The use of a separate MVA function at each  $m_H$  also introduces

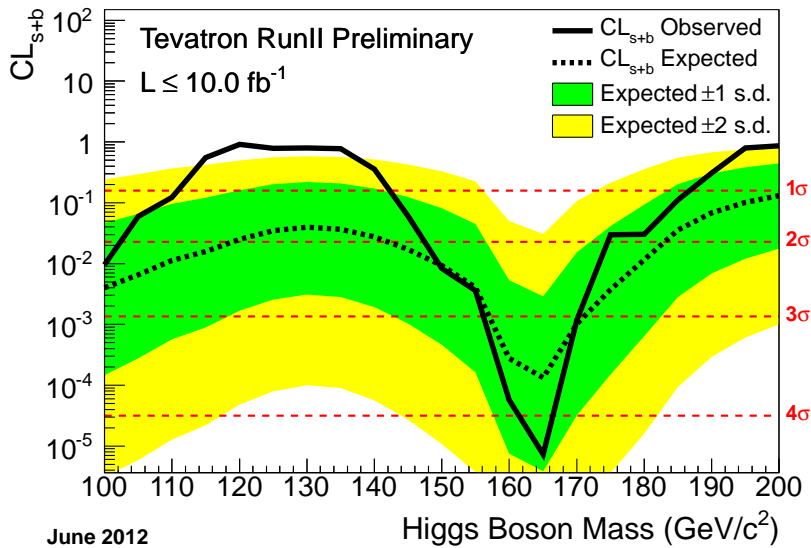


FIG. 12: The signal  $p$ -values  $CL_{s+b}$  as a function of the Higgs boson mass (in steps of  $5 \text{ GeV}/c^2$ ), for the combination of the CDF and D0 analyses. The green and yellow bands correspond to the regions enclosing 1 s.d. and 2 s.d. fluctuations around the median predicted value in the background-only hypothesis, respectively.

additional point-to-point randomness as individual events are reclassified from bins with lower  $s/b$  to higher  $s/b$  and vice versa. Even though the discriminants are nearly optimal and are thus highly similar from one  $m_H$  value to the next, small variations are amplified by the discrete nature of the data which are processed through these MVAs. One may see this in the variations of observed limits, LLR values and  $p$ -values from one mass point to the next which show more rapid variation than can be explained from mass resolution effects alone.

Gross and Vitells [92] provide a technique that extrapolates from a smaller sample of background-only Monte Carlo simulations fully propagated through the MVA discriminant functions. We lack the ability to perform this propagation through all of our channels, as we rely on exchanged histograms of distributions of selected events. We therefore estimate the LEE effect in a simplified manner. In the  $\approx 30 \text{ GeV}/c^2$  mass range, where the low-mass  $H \rightarrow b\bar{b}$  searches dominate, the reconstructed mass resolution is approximately 10-15%, or about  $15 \text{ GeV}/c^2$ . We therefore estimate a LEE factor of  $\sim 2$  for the low-mass region. The  $H \rightarrow \gamma\gamma$  searches have a much better mass resolution, of order 3%, but their contributions to the final LLR and the fitted cross sections are small due to the much smaller  $s/b$  in those searches. They introduce more rapid oscillations of LLR and the cross section fits as functions of  $m_H$ , but the magnitude of these oscillations is much smaller than those induced by the  $H \rightarrow b\bar{b}$  searches. The  $H \rightarrow \tau^+\tau^-$  searches have both worse reconstructed mass resolution and lower  $s/b$  than the  $H \rightarrow b\bar{b}$  searches and therefore similarly do not play a significant role in the estimation of the LEE.

We have cross-checked the estimation of a LEE by simulating many background-only pseudoexperiments using the reconstructed  $m_{jj}$  distributions for the  $WH \rightarrow \ell\nu b\bar{b}$ ,  $ZH \rightarrow \nu\bar{\nu} b\bar{b}$ , and  $ZH \rightarrow \ell^+\ell^- b\bar{b}$  searches, and finding the smallest  $p$ -value for each pseudoexperiment in the tested mass range. This distribution of smallest  $p$ -values is then used to estimate the chance of observing a particular smallest  $p$ -value or less. This study supports the factor of 2 used in the low-mass range. This test does not include the point-to-point scatter from the separate MVA training, and it also uses the  $m_{jj}$  variable which has better mass resolution than the MVAs, as the MVAs are trained to separate signal from background in order to perform a hypothesis test and are not optimized to measure the mass of the Higgs boson. Applying the LEE of 2 to the most significant local  $p$ -value obtained from our  $H \rightarrow b\bar{b}$  combination, we obtain a global significance of approximately 2.9 s.d.

We perform a fit of the signal-plus-background hypothesis to the observed data, allowing the signal strength modifier to vary as a function of  $m_H$ . The resulting best-fit signal strength (modifier) is shown in Figure 20. Because the  $WH \rightarrow \ell\nu b\bar{b}$ ,  $ZH \rightarrow \nu\bar{\nu} b\bar{b}$ , and  $ZH \rightarrow \ell^+\ell^- b\bar{b}$  searches seek Higgs boson production in only two modes that have



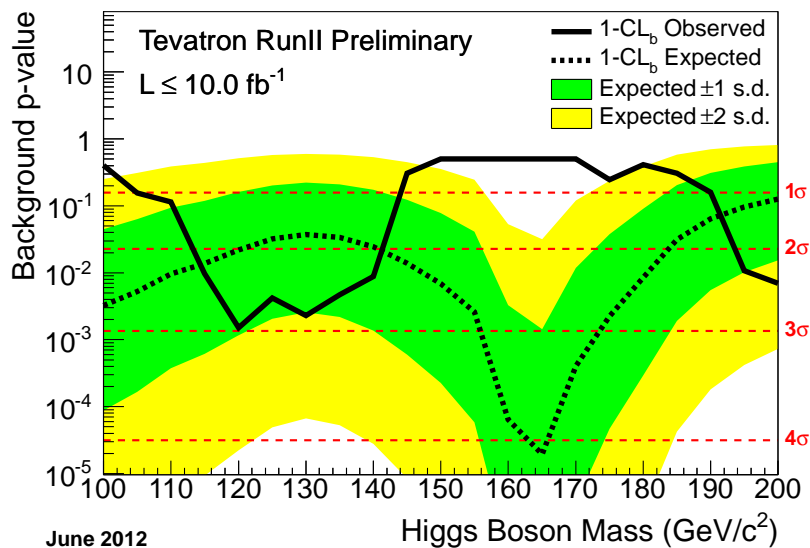


FIG. 13: The background  $p$ -values  $1\text{-CL}_b$  as a function of the Higgs boson mass (in steps of  $5 \text{ GeV}/c^2$ ), for the combination of the CDF and D0 analyses. The green and yellow bands correspond respectively to the regions enclosing 1 s.d. and 2 s.d. fluctuations around the median prediction in the signal plus background hypothesis at each value of  $m_H$ . See Table IX for numeric values.

common sources of systematic uncertainty and which vary together in many extended models, and because the three search categories are sensitive to  $H \rightarrow b\bar{b}$  decays, we no longer must normalize the measurement to the SM prediction. Instead, Figure 20 shows the measured cross section times branching ratio  $(\sigma_{WH} + \sigma_{ZH}) \times Br(H \rightarrow b\bar{b})$ , along with the SM prediction. The model assumption introduced is that the ratio  $\sigma_{WH}/\sigma_{ZH}$  is as predicted by the SM. The  $H \rightarrow b\bar{b}$  excess comes mainly from the CDF channels, which have combined  $> 2$  s.d. excesses, with the most signal-like candidates coming from CDF's  $ZH \rightarrow \ell\ell b\bar{b}$  channel. The Bayesian posterior is shown for the  $H \rightarrow b\bar{b}$  at  $m_H = 125 \text{ GeV}/c^2$  in Figure 21.

The CDF  $WH \rightarrow \ell\nu b\bar{b}$ ,  $ZH \rightarrow \nu\bar{\nu} b\bar{b}$ , and  $ZH \rightarrow \ell\ell b\bar{b}$  search channels make use of an improved neural-network  $b$ -tagging algorithm and all contribute to the observed excess. The D0  $H \rightarrow b\bar{b}$  channels combined see a  $\sim 1\text{-}1.5$  s.d. excess.

Above  $125 \text{ GeV}/c^2$ , the  $H \rightarrow W^+W^-$  channels contribute the majority of our search sensitivity. We combine all  $H \rightarrow W^+W^-$  searches from CDF and D0, incorporating potential signal contributions from  $gg \rightarrow H$ ,  $WH$ ,  $ZH$ , and VBF production. The result of this combination is shown in Figure 22. The distribution of the LLR is shown in Figure 23, which shows good agreement overall with the background-only hypothesis. Where the sensitivity is low, for  $m_H = 115 \text{ GeV}/c^2$  and  $m_H \geq 190 \text{ GeV}/c^2$ , the data are slightly more compatible with the signal-plus-background hypothesis. Figure 24 shows the observed and expected  $\text{CL}_{s+b}$  distribution as a function of  $m_H$ . Figure 25 shows the  $p$ -value for the background-only hypothesis. We perform a fit of the observed data to the signal-plus-background hypothesis, allowing the signal strength to vary in the fit as a function of  $m_H$  as shown in Figure 26. Consistent with Figure 23 the combined observed data do not indicate any significant excesses, though the D0  $H \rightarrow W^+W^-$  analysis has a slight excess ( $\sim 1.5$  s.d.) from  $115$  to  $140 \text{ GeV}/c^2$  consistent with the signal-plus-background hypothesis.

The  $H \rightarrow W^+W^-$  analyses which dominate the sensitivity of our high mass searches have poor resolution for reconstructing  $m_H$  due to the presence of two neutrinos in the final states of the most sensitive channels, and we thus expect the outcomes in these searches at each  $m_H$  in the high-mass range to be highly correlated with each other. Above  $m_H = 2M_W$ , the  $W$  bosons are on shell, and the kinematic variables take on different weights in the training of the MVAs than they do at masses below  $2M_W$ . At very high masses, the discriminating variable  $\Delta R_{\text{leptons}} = \sqrt{\Delta\phi_{\text{leptons}}^2 + \Delta\eta_{\text{leptons}}^2}$  [20, 34] plays less of a role than it does near the  $W^+W^-$  threshold. We therefore

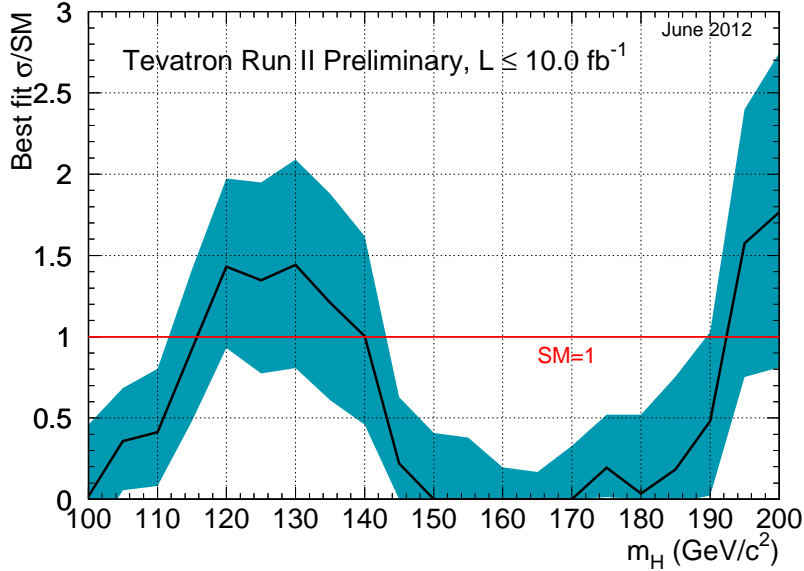


FIG. 14: The best fit signal cross section of all CDF and D0 search channels combined shown as a ratio to the standard model cross section as a function of the tested Higgs boson mass. The horizontal line at 1 represents the signal strength expected for a standard model Higgs boson hypothesis. The blue band shows the 1 s.d. uncertainty on the signal fit, and the red line is drawn at 1.0, corresponding to the SM prediction.

expect a LEE factor of approximately two for our high-mass searches in the mass range  $130 < m_H < 200 \text{ GeV}/c^2$ . Over the entire mass range of our Higgs searches,  $100 < m_H < 200 \text{ GeV}/c^2$ , we therefore expect that there are roughly four possible independent locations for uncorrelated excesses to appear in our analysis. The global  $p$ -value associated with our entire suite of Higgs searches is therefore  $1 - (1 - p_{\min})^4$ , using the Dunn-Šidák correction [93]. Based on this approach, if we simply chose to consider the region not currently excluded by other experiments, our resulting LEE factor would be one, making the global significance equivalent to the local significance. The smallest local  $p$ -value obtained from the full combination of CDF and D0 SM Higgs searches has a significance of 3.0 s.d. Applying a LEE of 4 to this value, we obtain a global significance of approximately 2.5 s.d.

We also separately combine CDF and D0 searches for  $H \rightarrow \gamma\gamma$ , and display the resulting upper limits on the production cross section times the decay branching ratio normalized to the SM prediction in Figure 27. Figure 28 shows the best-fit cross section normalized to the SM prediction for the combined  $H \rightarrow \gamma\gamma$  search channels, assuming the SM branching ratio for  $H \rightarrow \gamma\gamma$ .

As a final step, we show in Figure 29 the contribution of the three different sub-combinations to the best fit signal cross section for various values of  $m_H$ , as motivated by the observed deviations from expectation shown in the previous plots.

In summary, we combine all available CDF and D0 results on SM Higgs boson searches, based on luminosities ranging from 5.4 to 10.0  $\text{fb}^{-1}$ . Compared to our previous combination, more data have been included by those channels that hadn't previously used the full dataset, additional channels have been included, and analyses have been further optimized to gain sensitivity. The results presented here significantly extend the individual limits of each collaboration and those obtained in our previous combination. The combined search has sensitivity to a Higgs mass boson over the whole allowed mass range; we exclude, at the 95% C.L., two regions:  $100 < m_H < 103 \text{ GeV}/c^2$ , and  $147 < m_H < 180 \text{ GeV}/c^2$ . There is an excess of data events with respect to the background estimation in the mass range  $115 < m_H < 140 \text{ GeV}/c^2$  which causes our limits to not be as stringent as expected. At  $m_H = 120 \text{ GeV}/c^2$ , the  $p$ -value for a background fluctuation to produce this excess is  $\sim 1.5 \times 10^{-3}$ , corresponding to a local significance of 3.0 standard deviations. The global significance for such an excess anywhere in the full mass range is approximately

TABLE VI: Measurements of the best-fit values of  $R = \sigma \times \text{Br}/\text{SM}$  using the Bayesian method, for the combined SM,  $H \rightarrow W^+W^-$ ,  $H \rightarrow b\bar{b}$ , and  $H \rightarrow \gamma\gamma$  searches. The quoted uncertainties bound the smallest interval containing 68% of the integral of the posteriors.

$m_H$ (GeV/ $c^2$ )	$R_{\text{fit}}$ (SM)	$R_{\text{fit}}$ ( $H \rightarrow W^+W^-$ )	$R_{\text{fit}}$ ( $H \rightarrow b\bar{b}$ )	$R_{\text{fit}}$ ( $H \rightarrow \gamma\gamma$ )
100	$0.00^{+0.44}_{-0.00}$		$0.00^{+0.38}_{-0.00}$	$0.00^{+3.73}_{-0.00}$
105	$0.36^{+0.33}_{-0.30}$		$0.19^{+0.34}_{-0.19}$	$1.69^{+3.04}_{-1.69}$
110	$0.41^{+0.39}_{-0.33}$	$5.38^{+3.96}_{-3.51}$	$0.45^{+0.36}_{-0.35}$	$0.00^{+2.68}_{-0.00}$
115	$0.92^{+0.49}_{-0.44}$	$3.50^{+2.08}_{-2.13}$	$0.90^{+0.47}_{-0.45}$	$0.00^{+2.47}_{-0.00}$
120	$1.43^{+0.54}_{-0.50}$	$0.90^{+1.24}_{-0.90}$	$1.52^{+0.57}_{-0.58}$	$4.17^{+2.95}_{-2.54}$
125	$1.35^{+0.60}_{-0.57}$	$0.32^{+1.13}_{-0.32}$	$1.97^{+0.74}_{-0.68}$	$3.62^{+2.96}_{-2.54}$
130	$1.44^{+0.65}_{-0.64}$	$0.81^{+0.70}_{-0.71}$	$2.39^{+0.93}_{-0.94}$	$3.72^{+2.91}_{-2.78}$
135	$1.21^{+0.67}_{-0.60}$	$0.44^{+0.60}_{-0.44}$	$3.53^{+1.26}_{-1.16}$	$0.00^{+4.13}_{-0.00}$
140	$1.00^{+0.62}_{-0.54}$	$0.69^{+0.54}_{-0.52}$	$4.24^{+1.74}_{-1.70}$	$3.85^{+3.52}_{-3.31}$
145	$0.22^{+0.41}_{-0.22}$	$0.10^{+0.50}_{-0.10}$	$5.49^{+2.59}_{-2.35}$	$2.09^{+4.68}_{-2.09}$
150	$0.00^{+0.41}_{-0.00}$	$0.00^{+0.45}_{-0.00}$	$7.44^{+3.66}_{-3.65}$	$0.00^{+6.05}_{-0.00}$
155	$0.00^{+0.38}_{-0.00}$	$0.00^{+0.38}_{-0.00}$		
160	$0.00^{+0.20}_{-0.00}$	$0.00^{+0.20}_{-0.00}$		
165	$0.00^{+0.17}_{-0.00}$	$0.00^{+0.17}_{-0.00}$		
170	$0.00^{+0.33}_{-0.00}$	$0.00^{+0.32}_{-0.00}$		
175	$0.19^{+0.33}_{-0.18}$	$0.19^{+0.34}_{-0.19}$		
180	$0.03^{+0.49}_{-0.03}$	$0.05^{+0.48}_{-0.05}$		
185	$0.18^{+0.57}_{-0.18}$	$0.26^{+0.50}_{-0.26}$		
190	$0.48^{+0.55}_{-0.48}$	$0.57^{+0.54}_{-0.57}$		
195	$1.57^{+0.82}_{-0.82}$	$1.76^{+0.87}_{-0.86}$		
200	$1.77^{+0.98}_{-0.95}$	$2.12^{+1.07}_{-0.94}$		

2.5 standard deviations, after accounting for the look-elsewhere effect.

In addition, we separate the CDF and D0 searches into combinations focusing on the  $H \rightarrow b\bar{b}$  and  $H \rightarrow W^+W^-$  channels. The largest deviation occurs in the  $H \rightarrow b\bar{b}$  channels where a broad, signal-like, excess is observed. The minimum  $p$ -value of  $\sim 8.06 \times 10^{-4}$ , at  $m_H = 135$  GeV/ $c^2$ , corresponds to a local significance of 3.2 standard deviations prior to accounting for the look-elsewhere effect of  $\sim 2$ , which, when included, yields a global significance of  $\approx 2.9$  standard deviations.

### Acknowledgments

We thank the Fermilab staff and the technical staffs of the participating institutions for their vital contributions, and we acknowledge support from the DOE and NSF (USA); CONICET and UBACyT (Argentina); ARC (Australia); CNPq, FAPERJ, FAPESP and FUNDUNESP (Brazil); CRC Program and NSERC (Canada); CAS, CNSF, and NSC (China); Colciencias (Colombia); MSMT and GACR (Czech Republic); Academy of Finland (Finland); CEA and CNRS/IN2P3 (France); BMBF and DFG (Germany); INFN (Italy); DAE and DST (India); SFI (Ireland); Ministry of Education, Culture, Sports, Science and Technology (Japan); KRF, KOSEF and World Class University Program (Korea); CONACyT (Mexico); FOM (The Netherlands); FASI, Rosatom and RFBR (Russia); Slovak R&D Agency (Slovakia); Ministerio de Ciencia e Innovación, and Programa Consolider-Ingenio 2010 (Spain); The Swedish Research Council (Sweden); Swiss National Science Foundation (Switzerland); STFC and the Royal Society (United Kingdom); and the A.P. Sloan Foundation (USA).

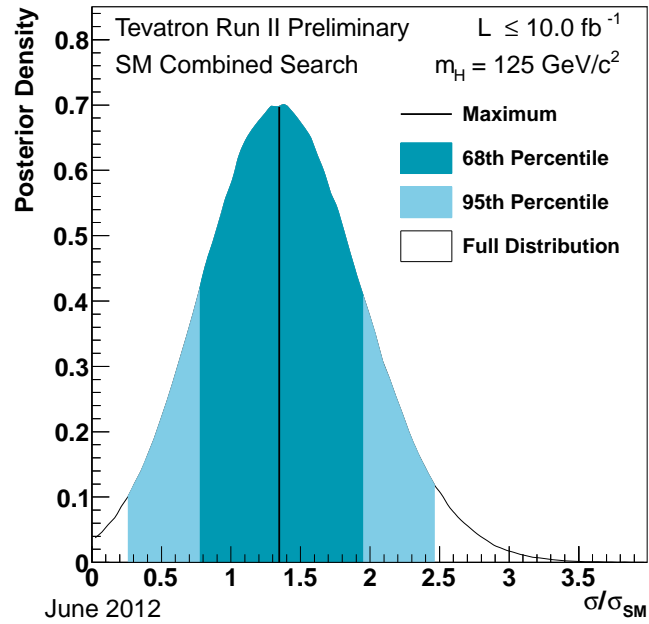


FIG. 15: The Bayesian posterior density for the cross section normalized to the SM prediction for the Tevatron combined search for a SM Higgs boson at  $m_H = 125 \text{ GeV}/c^2$ . The solid line shows the location of the maximum, and the dark-shaded region shows the shortest interval containing 68% of the integral.

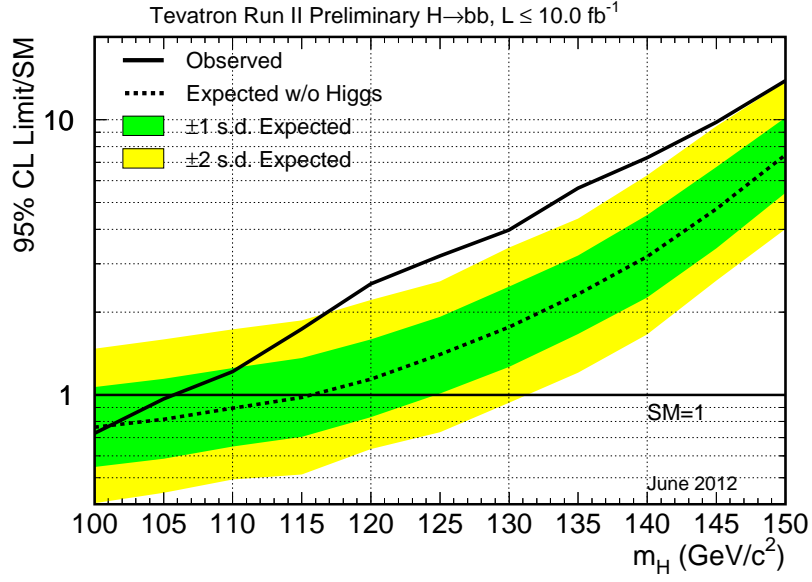


FIG. 16: Observed and expected (median, for the background-only hypothesis) 95% C.L. upper limits on the ratios to the SM cross section, as functions of the Higgs boson mass for the combination of CDF and D0 analyses focusing on the  $H \rightarrow b\bar{b}$  decay channel. The limits are expressed as a multiple of the SM prediction for test masses (every  $5 \text{ GeV}/c^2$ ) for which both experiments have performed dedicated searches in different channels. The points are joined by straight lines for better readability. The bands indicate the 68% and 95% probability regions where the limits can fluctuate, in the absence of signal. The limits displayed in this figure are obtained with the Bayesian calculation.

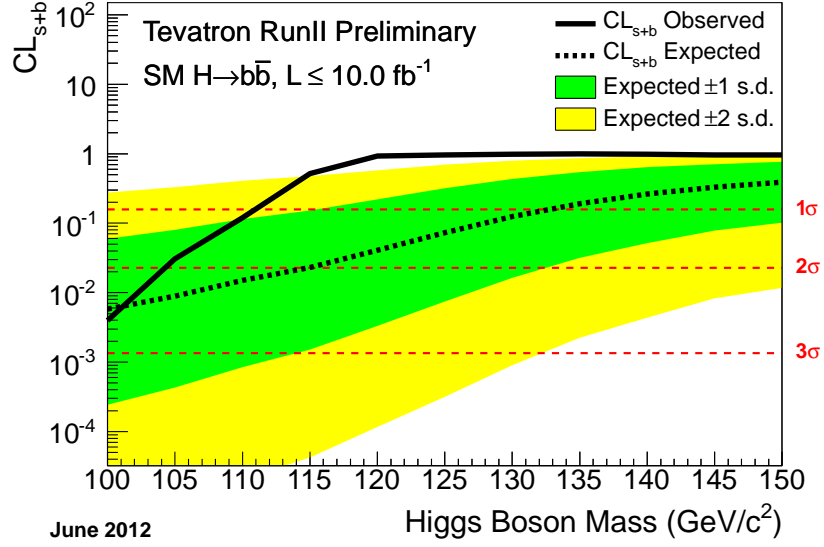


FIG. 18: The signal  $p$ -values  $CL_{s+b}$  for the signal plus background hypothesis as a function of the Higgs boson mass (in steps of  $5 \text{ GeV}/c^2$ ), for the combination of all CDF and D0 analyses in the  $H \rightarrow b\bar{b}$  channels. The green and yellow bands correspond to the regions enclosing 1 s.d. and 2 s.d. fluctuations of the background, respectively.

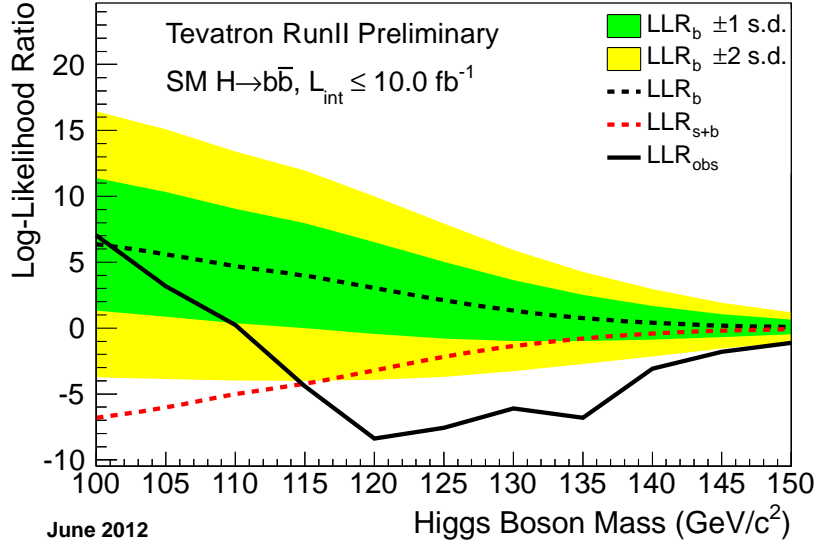


FIG. 17: Distributions of the log-likelihood ratio (LLR) as a function of Higgs boson mass obtained with the  $CL_s$  method for the combination of all CDF and D0 analyses in the  $H \rightarrow b\bar{b}$  channels. The green and yellow bands correspond to the regions enclosing 1 s.d. and 2 s.d. fluctuations of the background, respectively.

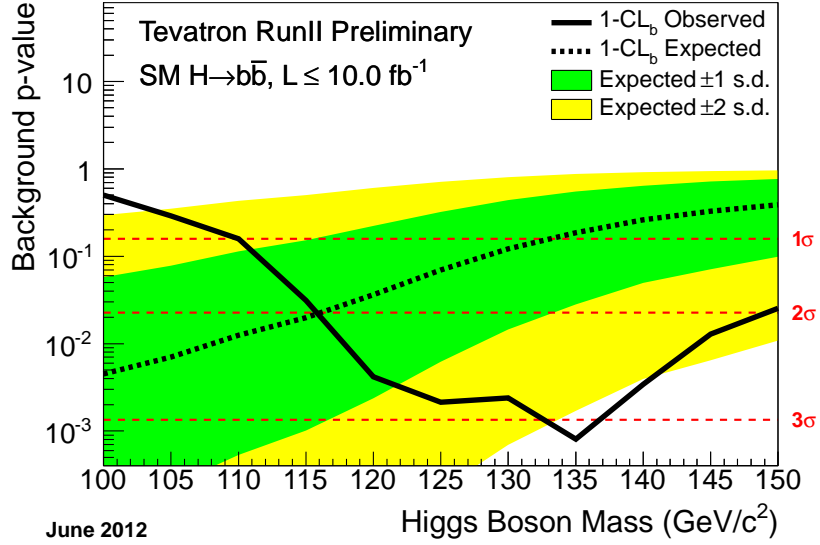


FIG. 19: The background  $p$ -values  $1-\text{CL}_b$  for the null hypothesis as a function of the Higgs boson mass (in steps of  $5 \text{ GeV}/c^2$ ), for the combination of all CDF and D0 analyses in the  $H \rightarrow b\bar{b}$  channels. The green and yellow bands correspond respectively to the regions enclosing 1 s.d. and 2 s.d. fluctuations around the median prediction in the signal plus background hypothesis at each value of  $m_H$ . See Table IX for numeric values.

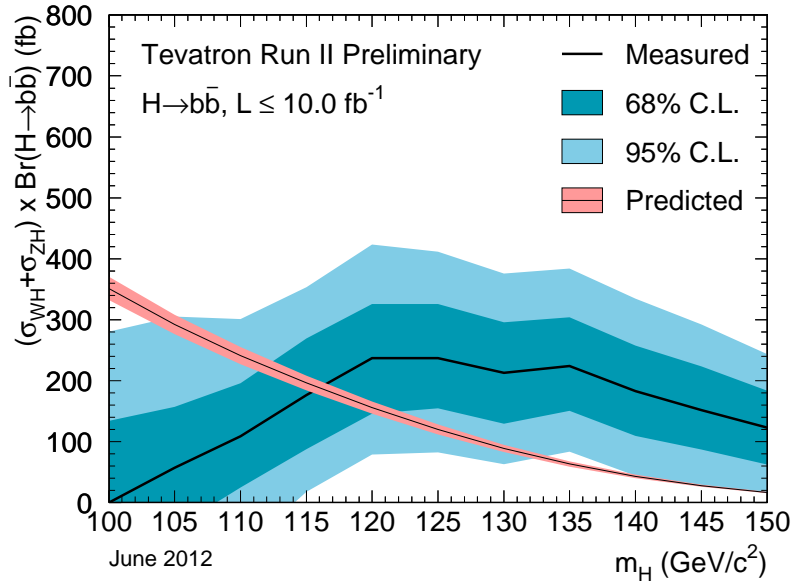


FIG. 20: The best fit of the cross section times branching ratio  $(\sigma_{WH} + \sigma_{ZH}) \times \text{Br}(H \rightarrow b\bar{b})$  for the combined CDF and D0 analyses in the  $H \rightarrow b\bar{b}$  channels, as a function of the Higgs boson mass, in steps of  $5 \text{ GeV}/c^2$ . The dark-shaded band shows the shortest interval at each tested mass which encloses 68% of the integral of the posterior, and the light-shaded band shows the corresponding interval for 95% of the integral of the posterior. Also shown is the SM prediction with its uncertainty.

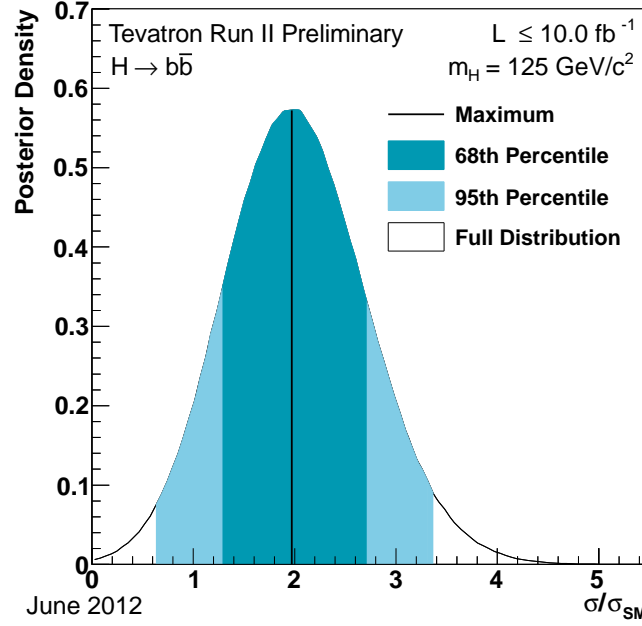


FIG. 21: The Bayesian posterior density for the cross section normalized to the SM prediction for the Tevatron combined search for a SM Higgs boson using only the  $H \rightarrow b\bar{b}$  channels at  $m_H = 125 \text{ GeV}/c^2$ . The solid line shows the location of the maximum, and the dark-shaded region shows the shortest interval containing 68% of the integral.

TABLE VII: Log-likelihood ratio (LLR) values for the combined CDF + D0 SM Higgs boson search obtained using the  $CL_S$  method.

$m_H$ ( $\text{GeV}/c^2$ )	$LLR_{\text{obs}}$	$LLR_{S+B}^{\text{med}}$	$LLR_B^{-2\text{s.d.}}$	$LLR_B^{-1\text{s.d.}}$	$LLR_B^{\text{med}}$	$LLR_B^{+1\text{s.d.}}$	$LLR_B^{+2\text{s.d.}}$
100	5.36	-7.41	17.61	12.31	7.02	1.72	-3.58
105	1.44	-6.53	16.08	11.12	6.16	1.19	-3.77
110	-0.05	-5.49	14.32	9.76	5.20	0.64	-3.92
115	-5.41	-4.86	13.21	8.91	4.62	0.32	-3.98
120	-9.39	-4.06	11.68	7.76	3.84	-0.08	-4.00
125	-6.39	-3.43	10.56	6.93	3.30	-0.33	-3.97
130	-6.12	-3.18	10.09	6.58	3.07	-0.43	-3.94
135	-6.12	-3.34	10.36	6.78	3.20	-0.38	-3.96
140	-2.46	-3.87	11.33	7.50	3.67	-0.16	-3.99
145	1.99	-4.83	12.95	8.71	4.48	0.25	-3.99
150	5.73	-6.05	14.94	10.24	5.53	0.83	-3.88
155	7.21	-7.78	17.57	12.28	6.99	1.70	-3.58
160	14.92	-14.47	25.57	18.69	11.82	4.94	-1.93
165	18.98	-16.61	27.63	20.38	13.13	5.88	-1.36
170	9.15	-11.13	21.74	15.59	9.44	3.30	-2.85
175	2.66	-8.04	17.81	12.47	7.13	1.79	-3.55
180	3.26	-5.68	14.21	9.68	5.14	0.61	-3.93
185	1.07	-3.46	10.45	6.85	3.24	-0.36	-3.96
190	-0.78	-2.31	8.15	5.18	2.21	-0.76	-3.74
195	-3.84	-1.69	6.72	4.17	1.63	-0.92	-3.47
200	-3.82	-1.31	5.76	3.51	1.26	-0.98	-3.23



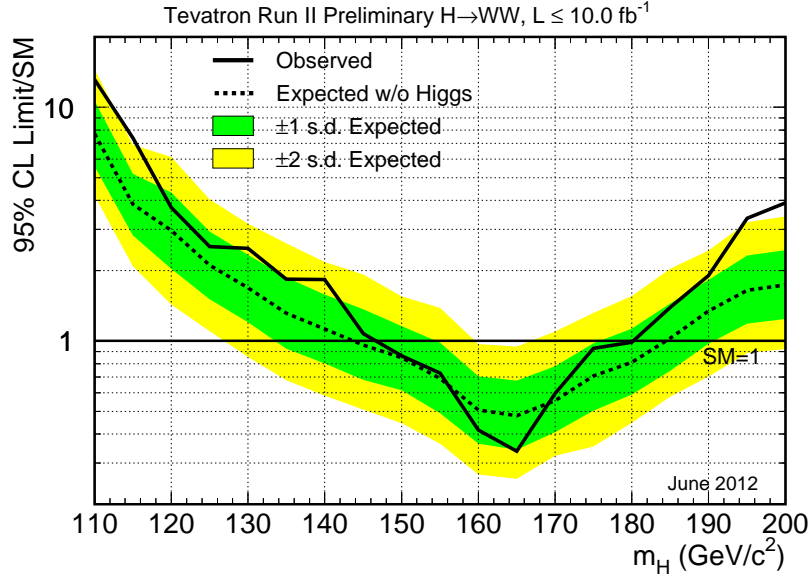


FIG. 22: Observed and expected (median, for the background-only hypothesis) 95% C.L. upper limits on the ratios to the SM cross section, as functions of the Higgs boson mass for the combination of CDF and D0 analyses focusing on the  $H \rightarrow W^+W^-$  decay channel. The limits are expressed as a multiple of the SM prediction for test masses (every  $5 \text{ GeV}/c^2$ ) for which both experiments have performed dedicated searches in different channels. The points are joined by straight lines for better readability. The bands indicate the 68% and 95% probability regions where the limits can fluctuate, in the absence of signal. The limits displayed in this figure are obtained with the Bayesian calculation.

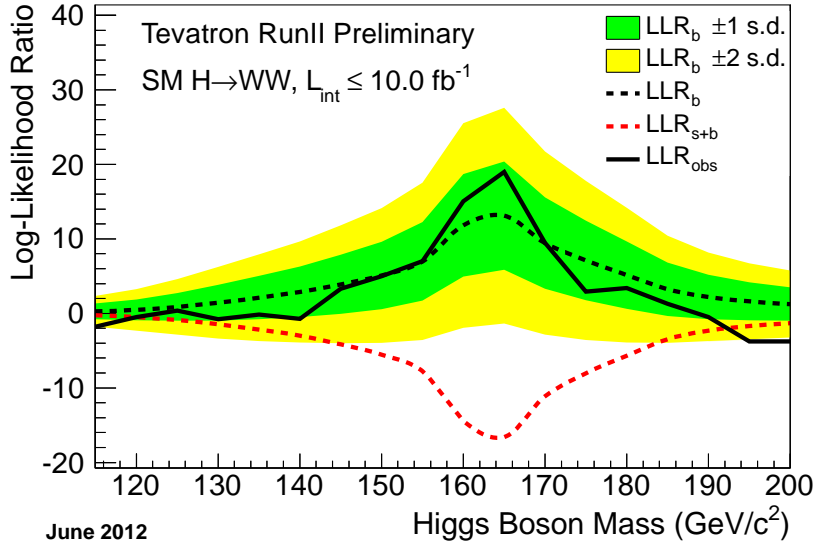


FIG. 23: Distributions of the log-likelihood ratio (LLR) as a function of Higgs boson mass obtained with the  $CL_s$  method for the combination of all CDF and D0 analyses in the  $H \rightarrow W^+W^-$  channels. The green and yellow bands correspond to the regions enclosing 1 s.d. and 2 s.d. fluctuations of the background, respectively.

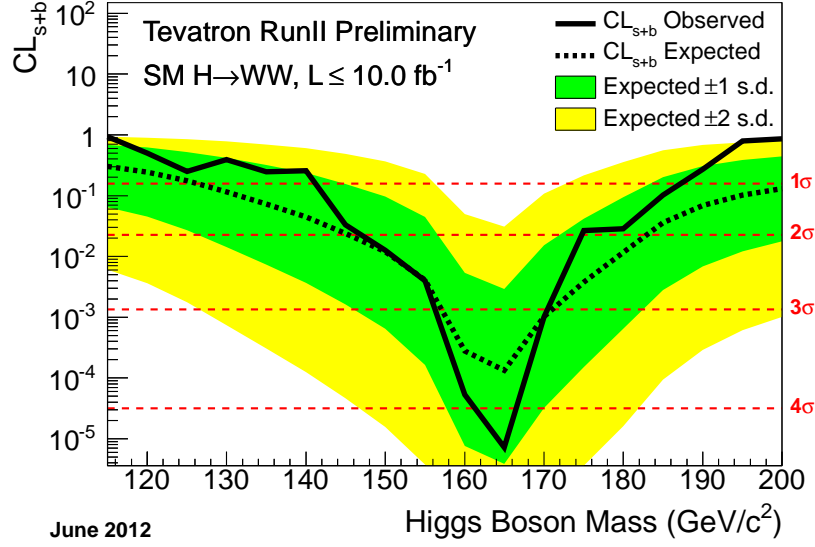


FIG. 24: The signal  $p$ -values  $CL_{s+b}$  for the signal plus background hypothesis as a function of the Higgs boson mass (in steps of  $5 \text{ GeV}/c^2$ ), for the combination of all CDF and D0 analyses in the  $H \rightarrow W^+W^-$  channels. The green and yellow bands correspond to the regions enclosing 1 s.d. and 2 s.d. fluctuations of the background, respectively.

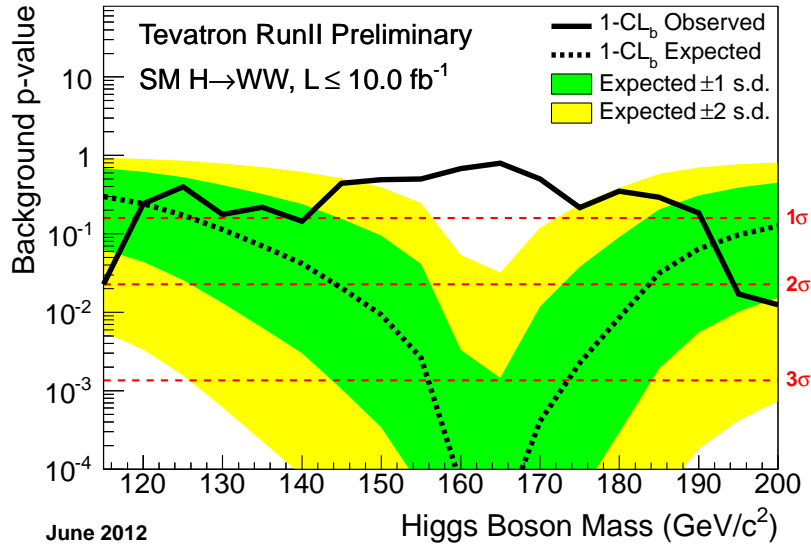


FIG. 25: The background  $p$ -values  $1-CL_b$  for the null hypothesis as a function of the Higgs boson mass (in steps of  $5 \text{ GeV}/c^2$ ), for the combination of all CDF and D0 analyses in the  $H \rightarrow W^+W^-$  channels. The green and yellow bands correspond to the regions enclosing 1 s.d. and 2 s.d. fluctuations of the background, respectively.

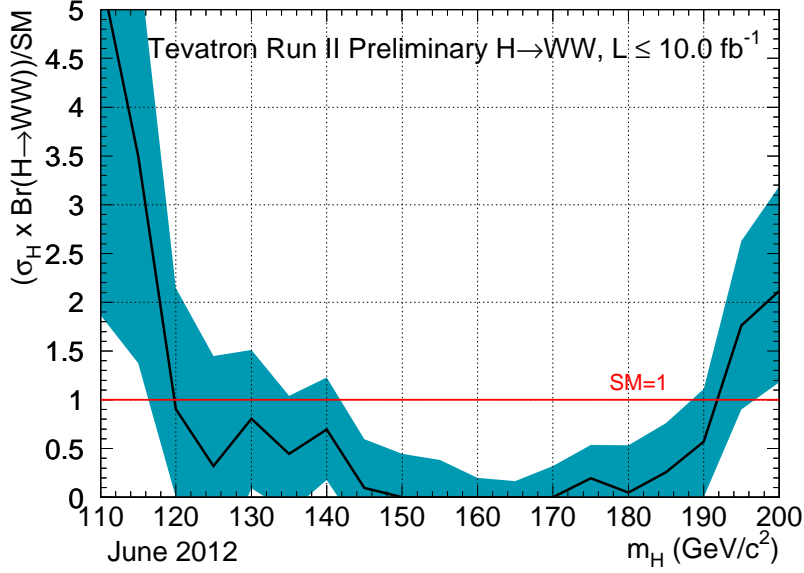


FIG. 26: The best fit of the signal cross section as a function of the Higgs boson mass (in steps of 5 GeV/c<sup>2</sup>) normalized to the SM expectation, for the combination of all CDF and D0 analyses in the  $H \rightarrow W^+W^-$  channels, assuming the SM prediction for the branching ratio of  $H \rightarrow W^+W^-$ . The blue band shows the 1 s.d. uncertainty on the signal fit, and the red line is drawn at 1.0, corresponding to the SM prediction.

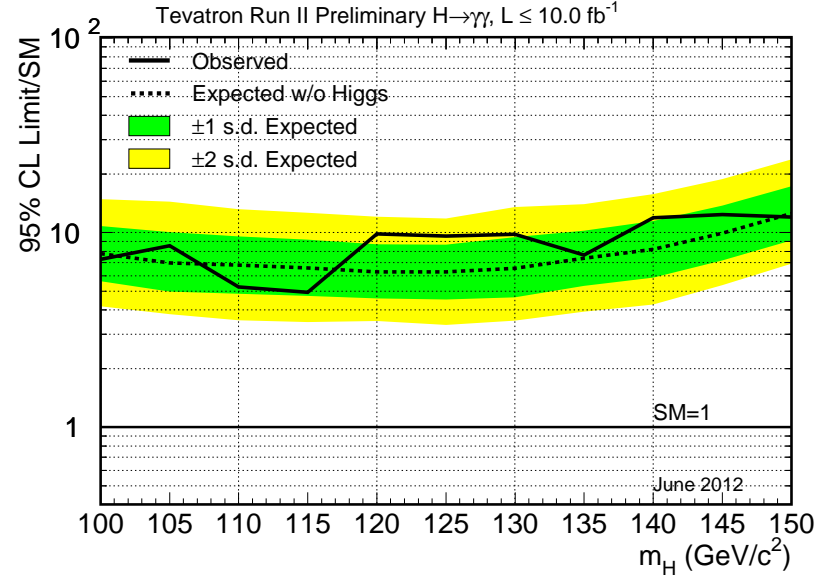


FIG. 27: Observed and expected (median, for the background-only hypothesis) 95% C.L. upper limits on the ratios to the SM cross section, as functions of the Higgs boson mass for the combination of CDF and D0 analyses focusing on the  $H \rightarrow \gamma\gamma$  decay channel. The limits are expressed as a multiple of the SM prediction for test masses (every 5 GeV/c<sup>2</sup>). The points are joined by straight lines for better readability. The bands indicate the 68% and 95% probability regions where the limits can fluctuate, in the absence of signal. The limits displayed in this figure are obtained with the Bayesian calculation.

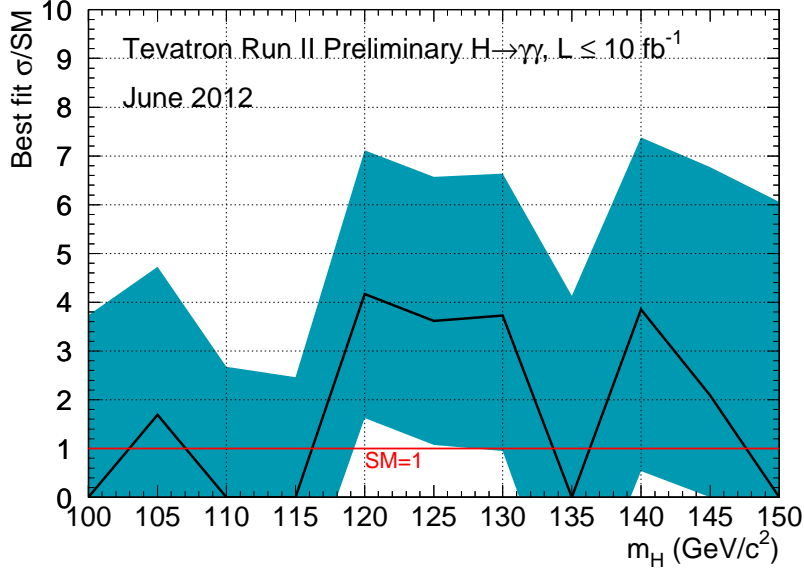


FIG. 28: The best fit of the signal cross section normalized to the SM prediction as a function of the Higgs boson mass (in steps of  $5 \text{ GeV}/c^2$ ), for the combination of the results of the CDF and D0 analyses in the  $H \rightarrow \gamma\gamma$  channels, assuming the SM branching ratio for  $H \rightarrow \gamma\gamma$ . The blue band shows the 1 s.d. uncertainty on the signal fit, and the red line is drawn at 1.0, corresponding to the SM prediction.

TABLE VIII: The observed and expected  $1\text{-CL}_s$  values as functions of  $m_H$ , for the combined CDF and D0 SM Higgs boson searches.

$m_H$ ( $\text{GeV}/c^2$ )	$1\text{-CL}_s^{\text{obs}}$	$1\text{-CL}_s^{-2\text{s.d.}}$	$1\text{-CL}_s^{-1\text{s.d.}}$	$1\text{-CL}_s^{\text{median}}$	$1\text{-CL}_s^{+1\text{s.d.}}$	$1\text{-CL}_s^{+2\text{s.d.}}$
100	0.984733	0.999862	0.999076	0.991946	0.944363	0.753477
105	0.928251	0.999743	0.998247	0.986947	0.922371	0.698868
110	0.859514	0.999440	0.996422	0.977471	0.886486	0.622156
115	0.444980	0.999041	0.994365	0.968374	0.857277	0.569486
120	0.092875	0.997892	0.989422	0.950075	0.807957	0.494648
125	0.208602	0.996486	0.983756	0.930688	0.760221	0.429162
130	0.201405	0.995590	0.980464	0.920511	0.737798	0.401923
135	0.220080	0.996034	0.982270	0.926569	0.752090	0.420332
140	0.619278	0.997508	0.987873	0.944717	0.794509	0.475693
145	0.916458	0.998803	0.993499	0.965848	0.852629	0.566360
150	0.982786	0.999523	0.997068	0.981462	0.903672	0.662878
155	0.992534	0.999835	0.998977	0.991909	0.947060	0.768774
160	0.999825	0.999953	0.999953	0.999448	0.993629	0.949186
165	0.999965	0.999955	0.999976	0.999735	0.996560	0.968572
170	0.997717	0.999938	0.999798	0.997953	0.981834	0.890325
175	0.962865	0.999843	0.999053	0.992521	0.950610	0.780557
180	0.954076	0.999296	0.995979	0.976808	0.888727	0.635001
185	0.846608	0.995895	0.982358	0.928482	0.759679	0.433596
190	0.634815	0.987244	0.956664	0.862714	0.636706	0.303485
195	0.191325	0.973359	0.924092	0.797722	0.543322	0.228722
200	0.125710	0.955755	0.889149	0.739059	0.472809	0.181778

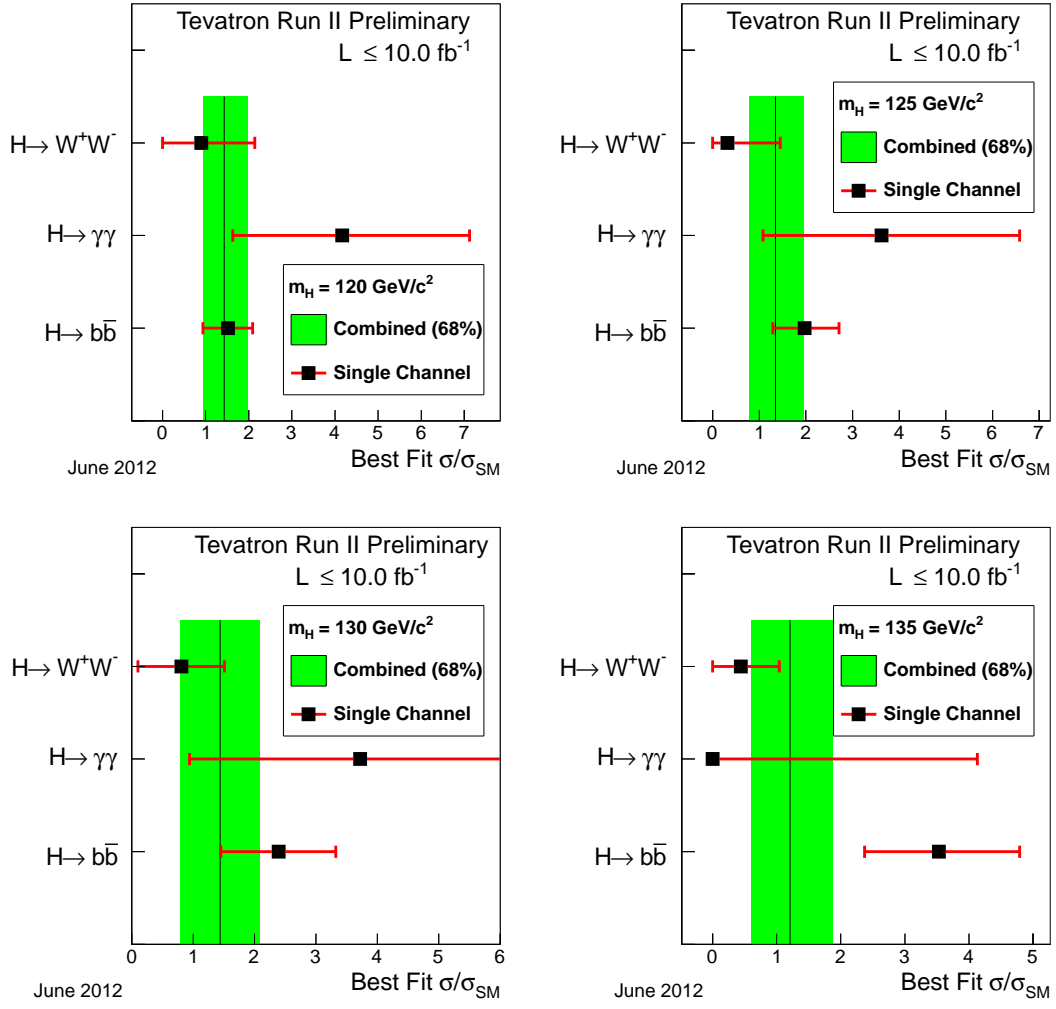


FIG. 29: Best fit signal strength for four hypothesized Higgs boson masses for the combination (black line) and for the three sub-combinations, for  $m_H$  values of 120, 125, 130, and 135  $GeV/c^2$ . The band corresponds to the  $\pm 1\sigma$  uncertainties on the full combination.

TABLE IX: The observed local background-only  $p$ -values ( $1 - \text{CL}_b^{\text{obs}}$ ) and the corresponding significances in units of standard deviations, as functions of  $m_H$ , for the combined CDF and D0 SM Higgs boson searches. Also listed are the background-only  $p$ -values and significances for the combined  $WH \rightarrow \ell\nu b\bar{b}$ ,  $ZH \rightarrow \nu\bar{\nu} b\bar{b}$ , and  $ZH \rightarrow \ell^+\ell^- b\bar{b}$  searches, labeled  $H \rightarrow b\bar{b}$  searches. See also Figures 13 and 19.

$m_H$ (GeV/ $c^2$ )	SM Higgs Search		$H \rightarrow b\bar{b}$ Search	
	$1 - \text{CL}_b^{\text{obs}}$	significance (s.d.)	$1 - \text{CL}_b^{\text{obs}}$	significance (s.d.)
100	0.401253	0.250	0.500000	0.000
105	0.155561	1.013	0.290898	0.551
110	0.114528	1.203	0.159107	0.998
115	0.009671	2.339	0.031209	1.863
120	0.001506	2.966	0.004168	2.638
125	0.004206	2.635	0.002139	2.857
130	0.002310	2.832	0.002405	2.819
135	0.004681	2.599	0.000806	3.154
140	0.008764	2.375	0.003429	2.704
145	0.307826	0.502	0.012800	2.232
150	0.500000	0.000	0.025444	1.952
155	0.500000	0.000		
160	0.500000	0.000		
165	0.500000	0.000		
170	0.500000	0.000		
175	0.244666	0.691		
180	0.415142	0.214		
185	0.308497	0.500		
190	0.160145	0.994		
195	0.010717	2.300		
200	0.007012	2.457		

- 
- [1] CDF Collaboration, “Combination of CDF standard model Higgs boson searches with up to to 9.7 fb<sup>-1</sup> of data”, CDF Conference Note 10804 (2012).
- [2] D0 Collaboration, “Search for the Standard Model Higgs Boson from the D0 Experiment in up to 9.7 fb<sup>-1</sup> of data”, D0 Conference Note 6344 (2012).
- [3] CDF Collaboration, Phys. Rev. Lett. **108**, 151803 (2012).
- [4] D0 Collaboration, “Measurement of the W Boson Mass with the D0 Detector”, Phys. Rev. Lett. **108**, 151804 (2012).
- [5] The LEP Electroweak Working Group, ”Status of March 2012”, <http://lepewwg.web.cern.ch/LEPEWWG/>.
- [6] R. Barate *et al.* [LEP Working Group for Higgs boson searches], Phys. Lett. B **565**, 61 (2003).
- [7] ATLAS Collaboration, “Combined search for the Standard Model Higgs Boson using up to 4.9 fb<sup>-1</sup> of pp collision data at  $\sqrt{s} = 7$  TeV with the ATLAS detector at the LHC”, Phys. Lett. B **710**, 49 (2012) .
- [8] CMS Collaboration, “Combined results of searches for the standard model Higgs boson in pp collisions at  $\sqrt{s} = 7$  TeV”, Phys. Lett. B **710**, 26 (2012).
- [9] The CDF and D0 Collaborations and the TEVNPH Working Group, “Combined CDF and D0 Upper Limits on Standard Model Higgs Boson Production with up to 10.0 fb<sup>-1</sup> of Data,” , FERMILAB-CONF-12-065-E, CDF Note 10806, D0 Note 6303, arXiv:1203.3774v1 [hep-ex] (2012);  
 The CDF and D0 Collaborations and the TEVNPH Working Group, “Combined CDF and D0 Upper Limits on Standard Model Higgs Boson Production with up to 8.6 fb<sup>-1</sup> of Data,” , FERMILAB-CONF-11-044-E, CDF Note 10606, D0 Note 6226, arXiv:1107.5518v2 [hep-ex] (2011);  
 The CDF and D0 Collaborations and the TEVNPH Working Group, “Combined CDF and D0 Upper Limits on Standard Model Higgs Boson Production with up to 8.2 fb<sup>-1</sup> of Data,” , FERMILAB-CONF-11-044-E, CDF Note 10441, D0 Note 6184, arXiv:1103.3233v1 [hep-ex] (2011);  
 The CDF and D0 Collaborations and the TEVNPH Working Group, “Combined CDF and D0 Upper Limits on Standard Model Higgs-Boson Production with up to 6.7 fb<sup>-1</sup> of Data”, FERMILAB-CONF-10-257-E, CDF Note 10241, D0 Note 6096, arXiv:1007.4587v1 [hep-ex] (2010);  
 The CDF and D0 Collaborations and the TEVNPH Working Group, “Combined CDF and DZero Upper Limits on Standard Model Higgs-Boson Production with 2.1 to 4.2 fb<sup>-1</sup> of Data”, FERMILAB-PUB-09-0557-E, CDF Note 9998, D0 Note 5983, arXiv:0911.3930v1 [hep-ex] (2009).  
 CDF Collaboration, “Combination of CDF standard model Higgs boson searches with up to to 9.7 fb<sup>-1</sup> of data”, CDF Conference Note 10804 (2012);  
 CDF Collaboration, “Combined Upper Limit on Standard Model Higgs Boson Production for EPS2011”, CDF Conference Note 10609 (2011);  
 CDF Collaboration, “Search for  $H \rightarrow WW^*$  Production Using 5.9 fb<sup>-1</sup>”, CDF Conference Note 10432 (2011);  
 CDF Collaboration, “Combined Upper Limit on Standard Model Higgs Boson Production for ICHEP 2010”, CDF Conference Note 10241 (2010);  
 CDF Collaboration, “Combined Upper Limit on Standard Model Higgs Boson Production for HCP 2009”, CDF Conference Note 9999 (2009);  
 CDF Collaboration, “Combined Upper Limit on Standard Model Higgs Boson Production for Summer 2009”, CDF Conference Note 9807 (2009);  
 D0 Collaboration, “Combined Upper Limits on Standard Model Higgs Boson Production from the D0 Experiment in up to 9.7 fb<sup>-1</sup> of data”, D0 Conference Note 6304 (2012);  
 D0 Collaboration, “Combined Upper Limits on Standard Model Higgs Boson Production from the D0 Experiment in up to 8.6 fb<sup>-1</sup> of data”, D0 Conference Note 6229 (2011);  
 D0 Collaboration, “Combined Upper Limits on Standard Model Higgs Boson Production in the  $W^+W^-$ ,  $\tau\tau$  and  $\gamma\gamma$  decay modes; from the D0 Experiment in up to 8.2 fb<sup>-1</sup> of data”, D0 Conference Note 6183 (2011);  
 D0 Collaboration, “Combined Upper Limits on Standard Model Higgs Boson Production from the D0 Experiment in up to 6.7 fb<sup>-1</sup> of data”, D0 Conference Note 6094 (2010);  
 D0 Collaboration, “Combined Upper Limits on Standard Model Higgs Boson Production from the D0 Experiment in 2.1-5.4 fb<sup>-1</sup>”, D0 Conference Note 6008 (2009);  
 D0 Collaboration, “Combined upper limits on Standard Model Higgs boson production from the D0 experiment in 0.9-5.0 fb<sup>-1</sup>”, D0 Conference Note 5984 (2009).
- [10] CDF Collaboration, “ Inclusive Search for Standard Model Higgs Boson Production in the WW Decay Channel Using the CDF II Detector”, Phys. Rev. Lett. **104**, 061803 (2010);  
 D0 Collaboration, “ Search for Higgs Boson Production in Dilepton and Missing Energy Final States with 5.4 fb<sup>-1</sup> of  $p\bar{p}$

- Collisions at  $\sqrt{s} = 1.96$  TeV”, Phys. Rev. Lett. 104, 061804 (2010);  
 The CDF and D0 Collaborations, “Combination of Tevatron Searches for the Standard Model Higgs Boson in the  $W^+W^-$  Decay Mode”, Phys. Rev. Lett. 104, 061802 (2010).
- [11] W. -Y. Keung and W. J. Marciano, Phys. Rev. D **30**, 248 (1984).  
 [12] E. W. N. Glover, J. Ohnemus and S. S. D. Willenbrock, Phys. Rev. D **37**, 3193 (1988).  
 [13] J. F. Gunion, H. E. Haber, G. Kane, and S. Dawson, *The Higgs Hunter’s Guide* (Addison-Wesley, Boston, 1990).  
 [14] M. Dittmar and H. K. Dreiner, Phys. Rev. D **55**, 167 (1997).  
 [15] S. L. Glashow, D. V. Nanopoulos, and A. Yildiz, Phys. Rev. D **18**, 1724 (1978).  
 [16] A. Stange, W. J. Marciano and S. Willenbrock, Phys. Rev. D **49**, 1354 (1994).  
 [17] CDF Collaboration, “Search for standard model Higgs boson production in association with a  $W$  boson using  $9.4 \text{ fb}^{-1}$ ”, CDF Conference Note 10796 (2012).  
 [18] CDF Collaboration, “Search for the standard model Higgs boson in the  $\cancel{E}_T$  plus  $b$ -jets signature in  $9.45 \text{ fb}^{-1}$ ”, CDF Conference Note 10798 (2012).  
 [19] CDF Collaboration, “A Search for the standard model Higgs boson in  $ZH \rightarrow \ell^+\ell^-b\bar{b}$  with  $9.45 \text{ fb}^{-1}$  of CDF II Data”, CDF Conference Note 10799 (2012).  
 [20] CDF Collaboration, “Search for  $H \rightarrow WW^*$  production using  $9.7 \text{ fb}^{-1}$ ”, CDF Conference Note 10785 (2012).  
 [21] CDF Collaboration, “Search for  $H \rightarrow WW^*$  with leptons and hadronic taus in the final state using  $9.7 \text{ fb}^{-1}$ ”, CDF Conference Note 10781 (2012).  
 [22] CDF Collaboration, “An inclusive search for the Higgs boson in the four lepton final state”, CDF Conference Note 10791 (2012).  
 [23] CDF Collaboration, “Search for the standard model Higgs boson in  $\tau^+\tau^-$  plus jets final state with  $8.3 \text{ fb}^{-1}$  of CDF data”, CDF Conference Note 10625 (2011).  
 [24] CDF Collaboration, “Search for the standard model Higgs in the  $\ell\nu\tau\tau$  and  $\ell\ell\tau\tau$  channels”, CDF Conference Note 10500 (2011).  
 [25] CDF Collaboration, “A search for the Higgs boson in the all-hadronic channel using  $9.45 \text{ fb}^{-1}$ ”, CDF Conference Note 10792 (2012).  
 [26] CDF Collaboration, “Search for a standard model Higgs boson decaying into photons at CDF using  $10.0 \text{ fb}^{-1}$  of data”, CDF Conference Note 10737 (2012).  
 [27] CDF Collaboration, “Search for the Higgs boson produced in association with top quarks”, CDF Conference Note 10801 (2012).  
 [28] CDF Collaboration, “Search for standard model Higgs boson production in association with  $t\bar{t}$  using no lepton final state”, CDF Conference Note 10582 (2011).  
 [29] D0 Collaboration, “Search for Higgs boson in final states with a lepton, missing energy and at least two jets in  $9.7 \text{ fb}^{-1}$  of Tevatron data,” D0 Conference Note 6346.  
 [30] D0 Collaboration, “Search for the standard model Higgs boson in the  $ZH \rightarrow \nu\nu b\bar{b}$  channel in  $9.5 \text{ fb}^{-1}$  of  $p\bar{p}$  collisions at  $\sqrt{s} = 1.96$  TeV”, D0 Conference note 6340.  
 [31] D0 Collaboration, “A Search for  $ZH \rightarrow \ell^+\ell^-b\bar{b}$  Production in  $9.7 \text{ fb}^{-1}$  of  $p\bar{p}$  Collisions”, D0 Conference Note 6342.  
 [32] D0 Collaboration, “Search for the standard model Higgs boson in tau pair final states”, D0 Conference note 6305.  
 [33] D0 Collaboration, “Search for associated Higgs boson production with  $VH \rightarrow e^\pm\nu_e\mu^\pm\nu_\mu + X$  like charged electron muon pairs using  $9.7 \text{ fb}^{-1}$  of  $p\bar{p}$  collisions at  $\sqrt{s} = 1.96$  TeV”, D0 Conference Note 6301.  
 [34] D0 Collaboration, “ Search for Higgs boson production in dilepton plus missing energy final states with  $9.7 \text{ fb}^{-1}$  of  $p\bar{p}$  collisions at  $\sqrt{s} = 1.96$  TeV”, D0 Conference Note 6343  
 [35] D0 Collaboration, “A search for the standard model Higgs boson in the  $H \rightarrow WW \rightarrow \ell\nu q\bar{q}'$  Decay Channel”, Phys. Rev. Lett. 106, 171802 (2011).  
 [36] D0 Collaboration, “Search for standard model Higgs boson with tri-leptons and missing transverse energy with  $9.7 \text{ fb}^{-1}$  of  $p\bar{p}$  collisions at  $\sqrt{s} = 1.96$  TeV”, D0 Conference Note 6276.  
 [37] D0 Collaboration, “Search for a standard model Higgs boson in the  $\tau\tau\mu$  final state with  $7.0 \text{ fb}^{-1}$  at  $\sqrt{s} = 1.96$  TeV”, D0 Conference Note 6286.  
 [38] D0 Collaboration, “Search for the Standard Model Higgs boson in  $\gamma\gamma + X$  final states at D0 with  $9.7 \text{ fb}^{-1}$  of data”, D0 Conference Note 6345.  
 [39] V. M. Abazov *et al.* [The D0 Collaboration], Nucl. Instrum. Methods A **620**, 490 (2010).  
 [40] J. Freeman *et al.*, arXiv:1205.1812 [hep-ex] (2012).  
 [41] A. Hoecker, P. Speckmayer, J. Stelzer, J. Therhaag, E. von Toerne, and H. Voss, “TMVA 4 Toolkit for Multivariate Data Analysis with ROOT User’s Guide” arXiv:physics/0703039a (2007);  
 C. Cortes and V. Vapnik, “Support vector networks”, Machine Learning **20**, 273 (1995);  
 V. Vapnik, “The Nature of Statistical Learning Theory”, Springer Verlag, New York (1995);



- C.J.C. Burges, “A Tutorial on Support Vector Machines for Pattern Recognition”, *Data Mining and Knowledge Discovery* **2**, 1 (1998).
- [42] T. Sjöstrand, L. Lonnblad and S. Mrenna, “PYTHIA 6.2: Physics and manual,” arXiv:hep-ph/0108264 (2001).
- [43] M. L. Mangano, M. Moretti, F. Piccinini, R. Pittau and A. D. Polosa, “ALPGEN, a generator for hard multiparton processes in hadronic collisions,” *J. High Energy Phys.* **0307**, 001 (2003).
- [44] S. Frixione and B.R. Webber, *J. High Energy Phys.* **0206**, 029 (2002).
- [45] G. Corcella *et al.*, *J. High Energy Phys.* **0101**, 010 (2001).
- [46] A. Pukhov *et al.*, “CompHEP: A package for evaluation of Feynman diagrams and integration over multi-particle phase space. User’s manual for version 33,” arXiv:hep-ph/9908288 (1999);  
E. Boos *et al.*, *Nucl. Instrum. Methods A* **534**, 250 (2004);  
E. Boos *et al.*, *Phys. Atom. Nucl.* **69**, 1317 (2006).
- [47] J. Campbell and R. K. Ellis, <http://mcfm.fnal.gov/>.
- [48] R. Brun, R. Hagelberg, M. Hansroul, and J. C. Lasalle, *GEANT: Simulation Program for Particle Physics Experiments. User Guide and Reference Manual*, CERN-DD-78-2-REV;  
S. Agostinelli *et al.*, *Nucl. Instrum. Methods A* **506**, 250 (2003).
- [49] H. L. Lai *et al.*, *Phys. Rev D* **55**, 1280 (1997).
- [50] C. Anastasiou, R. Boughezal and F. Petriello, *J. High Energy Phys.* **0904**, 003 (2009).
- [51] D. de Florian and M. Grazzini, *Phys. Lett. B* **674**, 291 (2009).
- [52] M. Grazzini, private communication (2010).
- [53] The CDF and D0 Collaborations and the Tevatron Electroweak Working Group, arXiv:0903.2503 [hep-ex] (2009).
- [54] R. V. Harlander and W. B. Kilgore, *Phys. Rev. Lett.* **88**, 201801 (2002).
- [55] C. Anastasiou and K. Melnikov, *Nucl. Phys. B* **646**, 220 (2002).
- [56] V. Ravindran, J. Smith, and W. L. van Neerven, *Nucl. Phys. B* **665**, 325 (2003).
- [57] S. Actis, G. Passarino, C. Sturm, and S. Uccirati, *Phys. Lett. B* **670**, 12 (2008).
- [58] U. Aglietti, R. Bonciani, G. Degrossi, A. Vicini, “Two-loop electroweak corrections to Higgs production in proton-proton collisions”, arXiv:hep-ph/0610033v1 (2006).
- [59] S. Catani, D. de Florian, M. Grazzini and P. Nason, “Soft-gluon resummation for Higgs boson production at hadron colliders,” *J. High Energy Phys.* **0307**, 028 (2003).
- [60] A. D. Martin, W. J. Stirling, R. S. Thorne and G. Watt, *Eur. Phys. J. C* **63**, 189 (2009).
- [61] <http://www.hep.ucl.ac.uk/pdf4lh/>;  
S. Alekhin *et al.*, (PDF4LHC Working Group), arXiv:1101.0536v1 [hep-ph] (2011);  
M. Botje *et al.*, (PDF4LHC Working Group), arXiv:1101.0538v1 [hep-ph] (2011).
- [62] I. W. Stewart, F. J. Tackmann, *Phys. Rev. D* **85**, 034011 (2012).
- [63] S. Dittmaier, S. Dittmaier, C. Mariotti, G. Passarino, R. Tanaka, S. Alekhin, J. Alwall and E. A. Bagnaschi *et al.*, arXiv:1201.3084 [hep-ph] (2012).
- [64] C. Anastasiou, G. Dissertori, M. Grazzini, F. Stöckli and B. R. Webber, *J. High Energy Phys.* **0908**, 099 (2009).
- [65] J. M. Campbell, R. K. Ellis, C. Williams, *Phys. Rev. D* **81**, 074023 (2010).
- [66] G. Bozzi, S. Catani, D. de Florian, and M. Grazzini, *Phys. Lett. B* **564**, 65 (2003);  
G. Bozzi, S. Catani, D. de Florian, and M. Grazzini, *Nucl. Phys. B* **737**, 73 (2006).
- [67] C. Balazs, J. Huston, I. Puljak, *Phys. Rev. D* **63** 014021 (2001).  
C. Balazs and C.-P. Yuan, *Phys. Lett. B* **478** 192-198 (2000).  
Qing-Hong Cao and Chuan-Ren Chen, *Phys. Rev. D* **76** 073006 (2007).
- [68] J. Baglio and A. Djouadi, *J. High Energy Phys.* **1010**, 064 (2010). We have obtained extended versions of the table of  $WH$  and  $ZH$  cross sections for all Higgs boson masses we test, and with more digits of precision, from the authors.
- [69] The Fortran program can be found on Michael Spira’s web page <http://people.web.psi.ch/~mspira/proglist.html>.
- [70] O. Brein, A. Djouadi, and R. Harlander, *Phys. Lett. B* **579**, 149 (2004).
- [71] M. L. Ciccolini, S. Dittmaier, and M. Kramer, *Phys. Rev. D* **68**, 073003 (2003).
- [72] G. Ferrera, M. Grazzini and F. Tramontano, *Phys. Rev. Lett.* **107**, 152003 (2011).
- [73] P. Bolzoni, F. Maltoni, S.-O. Moch, and M. Zaro, *Phys. Rev. Lett.* **105**, 011801 (2010).
- [74] M. Ciccolini, A. Denner, and S. Dittmaier, *Phys. Rev. Lett.* **99**, 161803 (2007);  
M. Ciccolini, A. Denner, and S. Dittmaier, *Phys. Rev. D* **77**, 013002 (2008).  
We would like to thank the authors of the HAWK program for adapting it to the Tevatron.
- [75] W. Beenaker, S. Dittmaier, M. Krämer, B. Plümper, M. Spira, and P. M. Zerwas, *Phys. Rev. Lett.* **87**, 201805 (2001);  
L. Reina and S. Dawson, *Phys. Rev. Lett.* **87**, 201804 (2001).
- [76] S. Dittmaier *et al.* [ LHC Higgs Cross Section Working Group Collaboration ], arXiv:1101.0593 [hep-ph] (2011).
- [77] A. Djouadi, J. Kalinowski and M. Spira, *Comput. Phys. Commun.* **108**, 56 (1998).

- [78] A. Bredenstein, A. Denner, S. Dittmaier, and M. M. Weber, Phys. Rev. D **74**, 013004 (2006);  
A. Bredenstein, A. Denner, S. Dittmaier, and M. Weber, J. High Energy Phys. **0702**, 080 (2007);  
A. Bredenstein, A. Denner, S. Dittmaier, A. Mück, and M. M. Weber, J. High Energy Phys. **0702**, 080 (2007)  
<http://omnibus.uni-freiburg.de/~sd565/programs/prophycy4f/prophycy4f.html> (2010).
- [79] J. Baglio, A. Djouadi, J. High Energy Phys. **1103**, 055 (2011).
- [80] A. Denner, S. Heinemeyer, I. Puljak, D. Rebuszi and M. Spira, Eur. Phys. J. C **71**, 1753 (2011).
- [81] The CDF and D0 Collaborations and the TEVNPH Working Group, “Combined CDF and D0 Measurement of  $WZ$  and  $ZZ$  Production in  $b$ -tagged Channels with up to 9.5 fb<sup>-1</sup> of Data” arXiv:1203.3782v1 [hep-ex] (2012).
- [82] T. Junk, Nucl. Instrum. Methods A **434**, 435 (1999);  
A.L. Read, “Modified Frequentist analysis of search results (the CL<sub>s</sub> method)”, in F. James, L. Lyons and Y. Perrin (eds.),  
*Workshop on Confidence Limits*, CERN, Yellow Report 2000-005, available through [cdsweb.cern.ch](http://cdsweb.cern.ch).
- [83] W. Fisher, “Systematics and Limit Calculations,” FERMILAB-TM-2386-E.
- [84] V. M. Abazov *et al.*, [D0 Collaboration], Phys. Rev. Lett. **103**, 092001 (2009).
- [85] S. Moch and P. Uwer, U. Langenfeld, S. Moch and P. Uwer, Phys. Rev. D **80**, 054009 (2009).
- [86] M. Cacciari, S. Frixione, M. L. Mangano, P. Nason and G. Ridolfi, J. High Energy Phys. **0809**, 127 (2008).  
N. Kidonakis and R. Vogt, Phys. Rev. D **78**, 074005 (2008).
- [87] N. Kidonakis, Phys. Rev. D **74**, 114012 (2006).
- [88] N. Kidonakis, private communication.
- [89] N. Kidonakis, N. Kidonakis, PoS DIS **2010**, 196 (2010).
- [90] B. W. Harris, E. Laenen, L. Phaf, Z. Sullivan and S. Weinzierl, Phys. Rev. D **66**, 054024 (2002).
- [91] J. Campbell and R. K. Ellis, Phys. Rev. D **65**, 113007 (2002).
- [92] E. Gross and O. Vitells, Eur. Phys. J. C **70**, 525 (2010).
- [93] Dunn, O.J., “Multiple Comparisons Among Means,” Journal of the American Statistical Association, **56**, 52-64 (1961).

# Appendices

## Appendix A: Systematic Uncertainties

TABLE X: Systematic uncertainties on the signal and background contributions for CDF's  $WH \rightarrow \ell\nu b\bar{b}$  single tight  $b$ -tag (Tx) and single loose  $b$ -tag (Lx) categories. Systematic uncertainties are listed by name; see the original references for a detailed explanation of their meaning and on how they are derived. Systematic uncertainties for  $WH$  shown in this table are obtained for  $m_H = 115 \text{ GeV}/c^2$ . Uncertainties are relative, in percent, and are symmetric unless otherwise indicated. Shape uncertainties are labeled with an "S".

CDF: single tight  $b$ -tag (Tx)  $WH \rightarrow \ell\nu b\bar{b}$  channel relative uncertainties (%)

Contribution	$W+HF$	Mistags	Top	Diboson	Non- $W$	$WH$
Luminosity ( $\sigma_{\text{inel}}(pp)$ )	3.8	0	3.8	3.8	0	3.8
Luminosity Monitor	4.4	0	4.4	4.4	0	4.4
Lepton ID	2.0-4.5	0	2.0-4.5	2.0-4.5	0	2.0-4.5
Jet Energy Scale	3.2-6.9(S)	0.9-1.8(S)	0.8-9.7(S)	3.6-13.2(S)	0	3.0-5.0(S)
Mistag Rate (tight)	0	19	0	0	0	0
Mistag Rate (loose)	0	0	0	0	0	0
$B$ -Tag Efficiency (tight)	0	0	3.9	3.9	0	3.9
$B$ -Tag Efficiency (loose)	0	0	0	0	0	0
$t\bar{t}$ Cross Section	0	0	10	0	0	0
Diboson Rate	0	0	0	6.0	0	0
Signal Cross Section	0	0	0	0	0	5
HF Fraction in $W$ +jets	30	0	0	0	0	0
ISR+FSR+PDF	0	0	0	0	0	3.8-6.8
$Q^2$	3.2-6.9(S)	0.9-1.8(S)	0	0	0	0
QCD Rate	0	0	0	0	40	0

CDF: single loose  $b$ -tag (Lx)  $WH \rightarrow \ell\nu b\bar{b}$  channel relative uncertainties (%)

Contribution	$W+HF$	Mistags	Top	Diboson	Non- $W$	$WH$
Luminosity ( $\sigma_{\text{inel}}(pp)$ )	3.8	0	3.8	3.8	0	3.8
Luminosity Monitor	4.4	0	4.4	4.4	0	4.4
Lepton ID	2	0	2	2	0	2
Jet Energy Scale	2.2-6.0(S)	0.9-1.8(S)	1.6-8.6(S)	4.6-9.6(S)	0	3.1-4.8(S)
Mistag Rate (tight)	0	0	0	0	0	0
Mistag Rate (loose)	0	10	0	0	0	0
$B$ -Tag Efficiency (tight)	0	0	0	0	0	0
$B$ -Tag Efficiency (loose)	0	0	3.2	3.2	0	3.2
$t\bar{t}$ Cross Section	0	0	10	0	0	0
Diboson Rate	0	0	0	6.0	0	0
Signal Cross Section	0	0	0	0	0	10
HF Fraction in $W$ +jets	30	0	0	0	0	0
ISR+FSR+PDF	0	0	0	0	0	2.4-4.9
QCD Rate	2.1-6.0(S)	0.9-1.8(S)	0	0	40	0

TABLE XI: Systematic uncertainties on the signal and background contributions for CDF's  $WH \rightarrow \ell\nu b\bar{b}$  two tight  $b$ -tag (TT), one tight  $b$ -tag and one loose  $b$ -tag (TL), and two loose  $b$ -tag (LL) channels. Systematic uncertainties are listed by name; see the original references for a detailed explanation of their meaning and on how they are derived. Systematic uncertainties for  $WH$  shown in this table are obtained for  $m_H = 115 \text{ GeV}/c^2$ . Uncertainties are relative, in percent, and are symmetric unless otherwise indicated. Shape uncertainties are labeled with an "S".

CDF: two tight  $b$ -tag (TT)  $WH \rightarrow \ell\nu b\bar{b}$  channel relative uncertainties (%)

Contribution	W+HF	Mistags	Top	Diboson	Non-W	WH
Luminosity ( $\sigma_{\text{inel}}(pp)$ )	3.8	0	3.8	3.8	0	3.8
Luminosity Monitor	4.4	0	4.4	4.4	0	4.4
Lepton ID	2.0-4.5	0	2.0-4.5	2.0-4.5	0	2.0-4.5
Jet Energy Scale	4.0-16.6(S)	0.9-3.3(S)	0.9-10.4(S)	4.7-19.7(S)	0	2.3-13.6(S)
Mistag Rate (tight)	0	40	0	0	0	0
Mistag Rate (loose)	0	0	0	0	0	0
$B$ -Tag Efficiency (tight)	0	0	7.8	7.8	0	7.8
$B$ -Tag Efficiency (loose)	0	0	0	0	0	0
$t\bar{t}$ Cross Section	0	0	10	0	0	0
Diboson Rate	0	0	0	6.0	0	0
Signal Cross Section	0	0	0	0	0	5
HF Fraction in W+jets	30	0	0	0	0	0
ISR+FSR+PDF	0	0	0	0	0	6.4-12.6
$Q^2$	4.0-8.8(S)	0.9-1.8(S)	0	0	0	0
QCD Rate	0	0	0	0	40	0

CDF: one tight and one loose  $b$ -tag (TL)  $WH \rightarrow \ell\nu b\bar{b}$  channel relative uncertainties (%)

Contribution	W+HF	Mistags	Top	Diboson	Non-W	WH
Luminosity ( $\sigma_{\text{inel}}(pp)$ )	3.8	0	3.8	3.8	0	3.8
Luminosity Monitor	4.4	0	4.4	4.4	0	4.4
Lepton ID	2.0-4.5	0	2.0-4.5	2.0-4.5	0	2.0-4.5
Jet Energy Scale	3.9-12.4(S)	0.9-3.3(S)	1.4-11.5(S)	5.0-16.0(S)		2.5-16.1(S)
Mistag Rate (tight)	0	19	0	0	0	0
Mistag Rate (loose)	0	10	0	0	0	0
$B$ -Tag Efficiency (tight)	0	0	3.9	3.9	0	3.9
$B$ -Tag Efficiency (loose)	0	0	3.2	3.2	0	3.2
$t\bar{t}$ Cross Section	0	0	10	0	0	0
Diboson Rate	0	0	0	6.0	0	0
Signal Cross Section	0	0	0	0	0	5
HF Fraction in W+jets	30	0	0	0	0	0
ISR+FSR+PDF	0	0	0	0	0	3.3-10.3
$Q^2$	3.9-7.7(S)	0.9-1.9(S)	0	0	0	0
QCD Rate	0	0	0	0	40	0

CDF: two loose  $b$ -tag (LL)  $WH \rightarrow \ell\nu b\bar{b}$  channel relative uncertainties (%)

Contribution	W+HF	Mistags	Top	Diboson	Non-W	WH
Luminosity ( $\sigma_{\text{inel}}(pp)$ )	3.8	0	3.8	3.8	0	3.8
Luminosity Monitor	4.4	0	4.4	4.4	0	4.4
Lepton ID	2	0	2	2	0	2
Jet Energy Scale	3.6-6.9(S)	0.9-1.8(S)	1.7-7.9(S)	1.2-8.5	0	2.7-5.4(S)
Mistag Rate (tight)	0	0	0	0	0	0
Mistag Rate (loose)	0	20	0	0	0	0
$B$ -Tag Efficiency (tight)	0	0	0	0	0	0
$B$ -Tag Efficiency (loose)	0	0	6.3	6.3	0	6.3
$t\bar{t}$ Cross Section	0	0	10	0	0	0
Diboson Rate	0	0	0	6.0	0	0
Signal Cross Section	0	0	0	0	0	10
HF Fraction in W+jets	30	0	0	0	0	0
ISR+FSR+PDF	0	0	0	0	0	2.0-13.6
QCD Rate	3.6-6.9(S)	0.9-1.8(S)	0	0	40	0

TABLE XII: Systematic uncertainties on the signal and background contributions for D0’s  $WH \rightarrow \ell\nu b\bar{b}$  single and double tag channels. Systematic uncertainties are listed by name, see the original references for a detailed explanation of their meaning and on how they are derived. Systematic uncertainties for  $WH$  shown in this table are obtained for  $m_H = 115 \text{ GeV}/c^2$ . Uncertainties are relative, in percent, and are symmetric unless otherwise indicated. Shape uncertainties are labeled with an “(S)”, and “SH” represents shape only uncertainty.

$WH \rightarrow \ell\nu b\bar{b}$  Single Tag (TST) channel relative uncertainties (%)

Contribution	Dibosons	$W + b\bar{b}/c\bar{c}$	$W+l.f.$	$t\bar{t}$	single top	Multijet	$WH$
Luminosity	6.1	6.1	6.1	6.1	6.1	–	6.1
Electron ID/Trigger eff. (S)	1–5	2–4	2–4	1–2	1–2	–	2–3
Muon Trigger eff. (S)	1	1	1	1	1	–	1
Muon ID/Reco eff./resol.	4.1	4.1	4.1	4.1	4.1	–	4.1
Jet ID/Reco eff.	2	2	2	2	2	–	2
Jet Resolution (S)	1–2	2–4	2–3	2–5	1–2	–	2
Jet Energy Scale (S)	4–7	1–5	2–5	2–7	1–2	–	2–6
Vertex Conf. Jet (S)	4–6	3–4	2–3	6–10	2–4	–	3–7
$b$ -tag/taggability (S)	1–3	1–4	7–10	1–6	1–2	–	2–9
Heavy-Flavor K-factor	–	20	–	–	–	–	–
Inst.-WH $e\nu b\bar{b}$ (S)	1–2	2–4	1–3	1–2	1–3	15	1–2
Inst.-WH $\mu\nu b\bar{b}$	–	2.4	2.4	–	–	20	–
Cross Section	6	9	6	7	7	–	6.1
Signal Branching Fraction	–	–	–	–	–	–	1-9
ALPGEN MLM pos/neg(S)	–	–	SH	–	–	–	–
ALPGEN Scale (S)	–	SH	SH	–	–	–	–
Underlying Event (S)	–	SH	SH	–	–	–	–
PDF, reweighting	2	2	2	2	2	–	2

$WH \rightarrow \ell\nu b\bar{b}$  Loose Double Tag (LDT) channel relative uncertainties (%)

Contribution	Dibosons	$W + b\bar{b}/c\bar{c}$	$W+l.f.$	$t\bar{t}$	single top	Multijet	$WH$
Luminosity	6.1	6.1	6.1	6.1	6.1	–	6.1
Electron ID/Trigger eff. (S)	2–5	2–3	2–3	1–2	1–2	–	1–2
Muon Trigger eff. (S)	1	1	1	1	1	–	1
Muon ID/Reco eff./resol.	4.1	4.1	4.1	4.1	4.1	–	4.1
Jet ID/Reco eff.	2	2	2	2	2	–	2
Jet Resolution (S)	1–7	2–7	2–3	2–7	2–4	–	1–5
Jet Energy Scale (S)	2–11	2–5	2–7	2–7	2–5	–	2–8
Vertex Conf. Jet (S)	2–11	2–12	2–3	4–15	2–3	–	3–7
$b$ -tag/taggability (S)	2–15	2–6	6–10	2–5	2–3	–	1–5
Heavy-Flavor K-factor	–	20	–	–	–	–	–
Inst.-WH $e\nu b\bar{b}$ (S)	1–2	2–4	1–3	1–2	1–3	15	1–2
Inst.-WH $\mu\nu b\bar{b}$	–	2.4	2.4	–	–	20	–
Cross Section	6	9	6	7	7	–	6.1
Signal Branching Fraction	–	–	–	–	–	–	1-9
ALPGEN MLM pos/neg(S)	–	–	SH	–	–	–	–
ALPGEN Scale (S)	–	SH	SH	–	–	–	–
Underlying Event (S)	–	SH	SH	–	–	–	–
PDF, reweighting	2	2	2	2	2	–	2

$WH \rightarrow \ell\nu b\bar{b}$  Medium Double Tag (MDT) channel relative uncertainties (%)

Contribution	Dibosons	$W + b\bar{b}/c\bar{c}$	$W+l.f.$	$t\bar{t}$	single top	Multijet	$WH$
Luminosity	6.1	6.1	6.1	6.1	6.1	–	6.1
Electron ID/Trigger eff. (S)	2–5	2–3	2–3	1–2	1–2	–	1–2
Muon Trigger eff. (S)	2–5	1–3	1–3	1–5	2–3	–	1–3
Muon ID/Reco eff./resol.	4.1	4.1	4.1	4.1	4.1	–	4.1
Jet ID/Reco eff.	2	2	2	2	2	–	2
Jet Resolution (S)	2–15	2–10	5–20	1–3	1–3	–	1–10
Jet Energy Scale (S)	2–10	2–20	1–8	1–5	1–5	–	2–10
Vertex Conf. Jet (S)	1–5	2–3	2–7	5–7	2–3	–	2–4
$b$ -tag/taggability (S)	3–15	4–15	10–15	4–10	3–9	–	2–5
Heavy-Flavor K-factor	–	20	–	–	–	–	–
Inst.-WH $e\nu b\bar{b}$ (S)	1–2	2–4	1–3	1–2	1–3	15	1–2
Inst.-WH $\mu\nu b\bar{b}$	–	2.4	2.4	–	–	20	–
Cross Section	6	9	6	7	7	–	6.1
Signal Branching Fraction	–	–	–	–	–	–	1–9
ALPGEN MLM pos/neg(S)	–	–	SH	–	–	–	–
ALPGEN Scale (S)	–	SH	SH	–	–	–	–
Underlying Event (S)	–	SH	SH	–	–	–	–
PDF, reweighting	2	2	2	2	2	–	2

 $WH \rightarrow \ell\nu b\bar{b}$  Tight Double Tag (TDT) channel relative uncertainties (%)

Contribution	Dibosons	$W + b\bar{b}/c\bar{c}$	$W+l.f.$	$t\bar{t}$	single top	Multijet	$WH$
Luminosity	6.1	6.1	6.1	6.1	6.1	–	6.1
Electron ID/Trigger eff. (S)	2–5	2–3	2–3	1–2	1–2	–	1–2
Muon Trigger eff. (S)	1	1	1	1	1	–	1
Muon ID/Reco eff./resol.	4.1	4.1	4.1	4.1	4.1	–	4.1
Jet ID/Reco eff.	2	2	2	2	2	–	2
Jet Resolution (S)	2–5	4–7	2–6	1–4	2–6	–	2–9
Jet Energy Scale (S)	2–15	2–8	1–8	2–7	1–4	–	1–9
Vertex Conf. Jet (S)	2–3	2–4	2–5	5–6	2–3	–	2–4
$b$ -tag/taggability (S)	3–15	5–10	5–15	6–10	5–10	–	5–12
Heavy-Flavor K-factor	–	20	–	–	–	–	–
Inst.-WH $e\nu b\bar{b}$ (S)	1–2	2–4	1–3	1–2	1–3	15	1–2
Inst.-WH $\mu\nu b\bar{b}$	–	2.4	2.4	–	–	20	–
Cross Section	6	9	6	7	7	–	6.1
Signal Branching Fraction	–	–	–	–	–	–	1–9
ALPGEN MLM pos/neg(S)	–	–	SH	–	–	–	–
ALPGEN Scale (S)	–	SH	SH	–	–	–	–
Underlying Event (S)	–	SH	SH	–	–	–	–
PDF, reweighting	2	2	2	2	2	–	2

TABLE XIII: Systematic uncertainties on the signal and background contributions for D0's  $VH \rightarrow VWW^* \rightarrow \ell\nu jjjj$  analysis. Systematic uncertainties are listed by name; see the original references for a detailed explanation of their meaning and on how they are derived. Signal uncertainties are shown for the total signal contribution at  $m_H = 125 \text{ GeV}/c^2$  for all channels. Those affecting the shape of the RF discriminant are indicated with "Y." Uncertainties are listed as relative changes in normalization, in percent, except for those also marked by "S," where the overall normalization is constant, and the value given denotes the maximum percentage change from nominal in any region of the distribution.

D0:  $VH \rightarrow VWW^* \rightarrow \ell\nu jjjj$  Zero Tag channel relative uncertainties (%)

Contribution	Dibosons	$W + b\bar{b}/c\bar{c}$	$W+l.f.$	Top quark	Multijet	Signal
Luminosity	6.1	6.1	6.1	6.1	–	6.1
Electron ID/Trigger eff. (S)	3	3	3	3	–	3
Muon Trigger eff. (S)	1	1	1	1	–	1
Muon ID/Reco eff./resol.	3	3	3	3	–	3
Jet ID/Reco eff.	2	2	2	2	–	2
Jet Resolution (S)	1–2	2–4	2–3	2–5	–	2
Jet Energy Scale (S)	5–10	1–5	2–7	2–7	–	2–6
Vertex Conf. Jet (S)	3–4	1–2	1–2	3–4	–	3–7
$b$ -tag/taggability (S)	4–5	1–3	1–3	5–10	–	4–10
Heavy-Flavor K-factor	–	20	–	–	–	–
Cross Section	6	9	6	7	–	6.1
Signal Branching Fraction	–	–	–	–	–	1–9
ALPGEN MLM pos/neg(S)	–	SH	–	–	–	–
ALPGEN Scale (S)	–	SH	SH	–	–	–
Underlying Event (S)	–	SH	–	–	–	–
PDF, reweighting	2	2	2	2	–	2

D0:  $VH \rightarrow VWW^* \rightarrow \ell\nu jjjj$  Loose Single Tag channel relative uncertainties (%)

Contribution	Dibosons	$W + b\bar{b}/c\bar{c}$	$W+l.f.$	Top quark	Multijet	Signal
Luminosity	6.1	6.1	6.1	6.1	–	6.1
Electron ID/Trigger eff. (S)	3	3	3	3	–	3
Muon Trigger eff. (S)	1	1	1	1	–	1
Muon ID/Reco eff./resol.	3	3	3	3	–	3
Jet ID/Reco eff.	2	2	2	2	–	2
Jet Resolution (S)	1–2	2–4	2–3	2–5	–	2
Jet Energy Scale (S)	5–10	1–5	2–7	2–7	–	2–6
Vertex Conf. Jet (S)	3–4	1–2	1–2	3–4	–	3–5
$b$ -tag/taggability (S)	2–8	1–3	1–2	5–10	–	4–10
Heavy-Flavor K-factor	–	20	–	–	–	–
Cross Section	6	9	6	7	–	6.1
Signal Branching Fraction	–	–	–	–	–	1–9
ALPGEN MLM pos/neg(S)	–	SH	–	–	–	–
ALPGEN Scale (S)	–	SH	SH	–	–	–
Underlying Event (S)	–	SH	–	–	–	–
PDF, reweighting	2	2	2	2	–	2

TABLE XIV: Systematic uncertainties on the signal and background contributions for CDF's  $WH, ZH \rightarrow \cancel{E}_T b\bar{b}$  tight double tag (SS), loose double tag (SJ), and single tag (1S) channels. Systematic uncertainties are listed by name; see the original references for a detailed explanation of their meaning and on how they are derived. Systematic uncertainties for  $ZH$  and  $WH$  shown in this table are obtained for  $m_H = 120 \text{ GeV}/c^2$ . Uncertainties are relative, in percent, and are symmetric unless otherwise indicated. Shape uncertainties are labeled with an "S".

CDF: tight double-tag (SS)  $WH, ZH \rightarrow \cancel{E}_T b\bar{b}$  channel relative uncertainties (%)

Contribution	ZH	WH	Multijet	Mistags	Top Pair	S. Top	Diboson	W + HF	Z + HF
Luminosity	3.8	3.8			3.8	3.8	3.8	3.8	3.8
Lumi Monitor	4.4	4.4			4.4	4.4	4.4	4.4	4.4
Tagging SF	10.4	10.4			10.4	10.4	10.4	10.4	10.4
Trigger Eff. (S)	0.9	1.4	0.9		0.9	1.6	2.0	1.8	1.2
Lepton Veto	2.0	2.0			2.0	2.0	2.0	2.0	2.0
PDF Acceptance	3.0	3.0			3.0	3.0	3.0	3.0	3.0
JES (S)	+1.7 -1.8	+2.4 -2.3			+0.0 -0.1	+2.5 -2.4	+4.1 -4.5	+4.3 -4.6	+8.8 -3.2
ISR/FSR		+3.0 +3.0							
Cross-Section	5	5			10	10	6	30	30
Multijet Norm. (shape)			2.5						
Mistag (S)				+36.7 -30					

CDF: loose double-tag (SJ)  $WH, ZH \rightarrow \cancel{E}_T b\bar{b}$  channel relative uncertainties (%)

Contribution	ZH	WH	Multijet	Mistags	Top Pair	S. Top	Diboson	W + HF	Z + HF
Luminosity	3.8	3.8			3.8	3.8	3.8	3.8	3.8
Lumi Monitor	4.4	4.4			4.4	4.4	4.4	4.4	4.4
Tagging SF	8.3	8.3			8.3	8.3	8.3	8.3	8.3
Trigger Eff. (S)	1.2	1.7	1.6		0.9	1.8	2.0	2.5	1.9
Lepton Veto	2.0	2.0			2.0	2.0	2.0	2.0	2.0
PDF Acceptance	3.0	3.0			3.0	3.0	3.0	3.0	3.0
JES (S)	+1.9 -1.9	+2.4 -2.4			+3.0 -2.8	-0.6 0.2	+4.2 -4.2	+6.8 -5.9	+8.3 -3.1
ISR/FSR		+2.4 -2.4							
Cross-Section	5.0	5.0			10	10	6	30	30
Multijet Norm.			1.6						
Mistag (S)				+65.2 -38.5					

CDF: single-tag (1S)  $WH, ZH \rightarrow \cancel{E}_T b\bar{b}$  channel relative uncertainties (%)

Contribution	ZH	WH	Multijet	Mistags	Top Pair	S. Top	Diboson	W + HF	Z + HF
Luminosity	3.8	3.8			3.8	3.8	3.8	3.8	3.8
Lumi Monitor	4.4	4.4			4.4	4.4	4.4	4.4	4.4
Tagging SF	5.2	5.2			5.2	5.2	5.2	5.2	5.2
Trigger Eff. (S)	1.2	1.7	1.6		0.9	1.8	2.0	2.5	1.9
Lepton Veto	2.0	2.0			2.0	2.0	2.0	2.0	2.0
PDF Acceptance	3.0	3.0			3.0	3.0	3.0	3.0	3.0
JES (S)	+2.6 -2.6	+3.3 -3.1			-0.8 +0.6	+2.7 -2.8	+5.1 -5.1	+8.2 -6.8	+10.8 -3.4
ISR/FSR		+2.0 -2.0							
Cross-Section	5.0	5.0			10	10	6	30	30
Multijet Norm.			0.7						
Mistag (S)				+17.9 -17.4					



TABLE XV: Systematic uncertainty ranges on the signal and background contributions and the error on the total background for D0's  $ZH \rightarrow \nu\nu b\bar{b}$  medium-tag and tight-tag channels. Systematic uncertainties are listed by name, see the original references for a detailed explanation of their meaning and on how they are derived. Systematic uncertainties for  $VH$  ( $WH+ZH$ ) shown in this table are obtained for  $m_H = 115$  GeV/ $c^2$ . Uncertainties are relative, in percent, and are symmetric unless otherwise indicated. Shape uncertainties are labeled with an “(S)”, and “SH” represents shape only uncertainty.

Contribution	Top	$V + b\bar{b}/c\bar{c}$	$V+l.f.$	Dibosons	Total Bkgd	$VH$
Jet ID/Reco Eff (S)	2.0	2.0	2.0	2.0	1.9	2.0
Jet Energy Scale (S)	1.3	1.5	2.8	1.5	1.9	0.3
Jet Resolution (S)	0.5	0.4	0.5	0.8	0.5	0.9
Vertex Conf. / Taggability (S)	3.4	2.2	2.0	2.3	2.2	2.1
b Tagging (S)	1.5	2.6	8.0	3.6	3.7	0.6
Lepton Identification	1.5	0.9	0.8	0.9	0.9	0.9
Trigger	2.0	2.0	2.0	2.0	1.9	2.0
Heavy Flavor Fractions	–	20.0	–	–	8.4	–
Cross Sections	10.0	10.2	10.2	7.0	9.8	7.0
Signal Branching Fraction	–	–	–	–	–	1-9
Luminosity	6.1	6.1	6.1	6.1	5.8	6.1
Multijet Normalization	–	–	–	–	1.1	–
ALPGEN MLM (S)	–	–	SH	–	–	–
ALPGEN Scale (S)	–	SH	SH	–	–	–
Underlying Event (S)	–	SH	SH	–	–	–
PDF, reweighting (S)	SH	SH	SH	SH	SH	SH
Total uncertainty	12.8	23.8	15.1	10.8	14.2	10.0

Contribution	Top	$V + b\bar{b}/c\bar{c}$	$V+l.f.$	Dibosons	Total Bkgd	$VH$
Jet ID/Reco Eff (S)	2.0	2.0	2.0	2.0	2.0	2.0
Jet Energy Scale (S)	1.0	1.6	3.9	1.6	1.6	0.5
Jet Resolution (S)	0.7	0.6	2.6	1.4	0.8	1.3
Vertex Conf. / Taggability (S)	3.0	1.9	2.4	2.0	2.3	1.9
b Tagging (S)	8.9	7.3	12.5	6.4	7.4	7.8
Lepton Identification	1.9	0.8	0.3	0.7	1.1	0.8
Trigger	2.0	2.0	2.0	2.0	2.0	2.0
Heavy Flavor Fractions	–	20.0	–	–	11.0	–
Cross Sections	10.0	10.2	10.2	7.0	10.0	7.0
Signal Branching Fraction	–	–	–	–	–	1-9
Luminosity	6.1	6.1	6.1	6.1	6.1	6.1
Multijet Normalization	–	–	–	–	0.2	–
ALPGEN MLM (S)	–	–	SH	–	–	–
ALPGEN Scale (S)	–	SH	SH	–	–	–
Underlying Event (S)	–	SH	SH	–	–	–
PDF, reweighting (S)	SH	SH	SH	SH	SH	SH
Total uncertainty	15.5	24.7	18.3	12.0	16.8	12.7





TABLE XVIII: Systematic uncertainties on the contributions for D0's  $ZH \rightarrow \ell^+ \ell^- b\bar{b}$  channels. Systematic uncertainties are listed by name; see the original references for a detailed explanation of their meaning and on how they are derived. Systematic uncertainties for  $ZH$  shown in this table are obtained for  $m_H = 125 \text{ GeV}/c^2$ . Uncertainties are relative, in percent, and are symmetric unless otherwise indicated. Shape uncertainties are labeled with an "(S)".

$ZH \rightarrow \ell b\bar{b}$  Single Tag (ST) channel relative uncertainties (%) in the  $t\bar{t}$  depleted region

Contribution	$ZH$	Multijet	$Z+l.f.$	$Z+b\bar{b}$	$Z+c\bar{c}$	Dibosons	Top
Jet Energy Scale (S)	0.6	–	3.1	2.3	2.3	4.8	0.3
Jet Energy Resolution (S)	0.7	–	2.7	1.3	1.6	1.0	1.1
Jet ID (S)	0.6	–	1.5	0.0	0.5	0.7	0.7
Taggability (S)	2.0	–	1.9	1.7	1.7	1.8	2.2
$Z_{p_T}$ Model (S)	–	–	1.6	1.7	1.5	–	–
HF Tagging Efficiency (S)	0.5	–	–	1.6	3.9	–	0.7
LF Tagging Efficiency (S)	–	–	68	–	–	2.9	–
$ee$ Multijet Shape (S)	–	45	–	–	–	–	–
Multijet Normalization	–	10	–	–	–	–	–
$Z$ +jets Jet Angles (S)	–	–	1.7	1.7	1.7	–	–
AlpGen MLM (S)	–	–	0.2	–	–	–	–
AlpGen Scale (S)	–	–	0.3	0.5	0.5	–	–
Underlying Event (S)	–	–	0.4	0.4	0.4	–	–
Trigger (S)	0.4-2	–	0.03-2	0.2-2	0.2-2	0.2-2	0.5-2
Cross Sections	6	–	–	20	20	7	10
Signal Branching Fraction	1-9	–	–	–	–	–	–
Normalization	5	–	4	4	4	6	5
PDFs	0.6	–	1.0	2.4	1.1	0.7	5.9

$ZH \rightarrow \ell b\bar{b}$  Double Tag (DT) channel relative uncertainties (%) in the  $t\bar{t}$  depleted region

Contribution	$ZH$	Multijet	$Z+l.f.$	$Z+b\bar{b}$	$Z+c\bar{c}$	Dibosons	Top
Jet Energy Scale (S)	0.5	–	4.6	3.0	1.3	4.5	1.4
Jet Energy Resolution(S)	0.4	–	7.0	1.8	2.9	0.9	0.9
JET ID (S)	0.6	–	7.9	0.3	0.5	0.5	0.5
Taggability (S)	1.7	–	7.0	1.5	1.5	3.0	1.7
$Z_{p_T}$ Model (S)	–	–	2.9	1.4	1.9	–	–
HF Tagging Efficiency (S)	4.4	–	–	5.0	5.6	–	3.8
LF Tagging Efficiency (S)	–	–	75	–	–	4.7	–
$ee$ Multijet Shape (S)	–	66	–	–	–	–	–
Multijet Normalization	–	10	–	–	–	–	–
$Z$ +jets Jet Angles (S)	–	–	1.9	3.5	3.8	–	–
AlpGen MLM (S)	–	–	0.2	–	–	–	–
AlpGen Scale (S)	–	–	0.4	0.5	0.5	–	–
Underlying Event(S)	–	–	0.5	0.4	0.4	–	–
Trigger (S)	0.4-2	–	0.6-6	0.3-2	0.3-3	0.4-2	0.6-5
Cross Sections	6	–	–	20	20	7	10
Signal Branching Fraction	1-9	–	–	–	–	–	–
Normalization	5	–	4	4	4	6	5
PDFs	0.6	–	1.0	2.4	1.1	0.7	5.9

$ZH \rightarrow \ell\ell b\bar{b}$  Single Tag (ST) channel relative uncertainties (%) in the  $t\bar{t}$  enriched region

Contribution	$ZH$	Multijet	$Z+l.f.$	$Z+b\bar{b}$	$Z+c\bar{c}$	Dibosons	Top
Jet Energy Scale (S)	7.5	–	4.6	1.7	3.9	11	2.5
Jet Energy Resolution (S)	0.2	–	4.5	0.7	3.1	3.9	0.7
Jet ID (S)	1.2	–	2.1	1.0	1.2	0.9	0.7
Taggability (S)	2.1	–	7.3	2.7	3.0	2.0	3.2
$Z_{p_T}$ Model (S)	–	–	3.3	1.5	1.4	–	–
HF Tagging Efficiency (S)	0.5	–	–	1.3	4.8	–	0.8
LF Tagging Efficiency (S)	–	–	73	–	–	4.1	–
$ee$ Multijet Shape (S)	–	59	–	–	–	–	–
Multijet Normalization	–	10	–	–	–	–	–
$Z$ +jets Jet Angles (S)	–	–	1.7	2.3	2.7	–	–
AlpGen MLM (S)	–	–	0.4	–	–	–	–
AlpGen Scale (S)	–	–	0.7	0.7	0.7	–	–
Underlying Event (S)	–	–	0.9	1.1	1.1	–	–
Trigger (S)	1-4	–	1-4	0.7-4	0.7-4	1-8	1-8
Cross Sections	6	–	–	20	20	7	10
Signal Branching Fraction	1-9	–	–	–	–	–	–
Normalization	5	–	4	4	4	6	5
PDFs	0.6	–	1.0	2.4	1.1	0.7	5.9

 $ZH \rightarrow \ell\ell b\bar{b}$  Double Tag (DT) channel relative uncertainties (%) in the  $t\bar{t}$  enriched region

Contribution	$ZH$	Multijet	$Z+l.f.$	$Z+b\bar{b}$	$Z+c\bar{c}$	Dibosons	Top
Jet Energy Scale (S)	6.6	–	0.8	1.6	2.2	5.9	1.5
Jet Energy Resolution(S)	1.4	–	267	1.4	2.1	4.0	0.4
JET ID (S)	0.9	–	0.6	0.5	3.6	2.8	0.6
Taggability (S)	2.0	–	0.9	1.6	1.9	3.1	2.1
$Z_{p_T}$ Model (S)	–	–	1.8	1.4	1.5	–	–
HF Tagging Efficiency (S)	4.0	–	–	5.1	6.6	–	4.2
LF Tagging Efficiency (S)	–	–	72	–	–	–	–
$ee$ Multijet Shape (S)	–	91	–	–	–	–	–
Multijet Normalization	–	10	–	–	–	–	–
$Z$ +jets Jet Angles (S)	–	–	1.4	3.7	2.3	–	–
AlpGen MLM (S)	–	–	0.5	–	–	–	–
AlpGen Scale (S)	–	–	0.8	0.5	0.4	–	–
Underlying Event(S)	–	–	0.9	0.7	0.5	–	–
Trigger (S)	1-3	–	1-3	0.6-3	0.7-4	0.7-4	1-3
Cross Sections	6	–	–	20	20	7	10
Signal Branching Fraction	1-9	–	–	–	–	–	–
Normalization	5	–	4	4	4	6	5
PDFs	0.6	–	1.0	2.4	1.1	0.7	5.9

TABLE XIX: Systematic uncertainties on the signal and background contributions for CDF's  $H \rightarrow W^+W^- \rightarrow \ell^\pm \ell'^\mp$  channels with zero, one, and two or more associated jets. These channels are sensitive to gluon fusion production (all channels) and  $WH, ZH$  and VBF production. Systematic uncertainties are listed by name (see the original references for a detailed explanation of their meaning and on how they are derived). Systematic uncertainties for  $H$  shown in this table are obtained for  $m_H = 160$  GeV/ $c^2$ . Uncertainties are relative, in percent, and are symmetric unless otherwise indicated. The uncertainties associated with the different background and signal processed are correlated within individual jet categories unless otherwise noted. Boldface and italics indicate groups of uncertainties which are correlated with each other but not the others on the line.

CDF:  $H \rightarrow W^+W^- \rightarrow \ell^\pm \ell'^\mp$  with no associated jet channel relative uncertainties (%)

Contribution	<i>WW</i>	<i>WZ</i>	<i>ZZ</i>	<i>t<math>\bar{t}</math></i>	DY	<i>W<math>\gamma</math></i>	<i>W+jet</i>	<i>gg <math>\rightarrow</math> H</i>	<i>WH</i>	<i>ZH</i>	VBF
<b>Cross Section</b>											
ScaleInclusive								13.4			
Scale1+Jets								-23.0			
Scale2+Jets								0.0			
PDF Model								7.6			
Total	<i>6.0</i>	<i>6.0</i>	<i>6.0</i>	<i>7.0</i>					<b>5.0</b>	<b>5.0</b>	10.0
<b>Acceptance</b>											
Scale (jets)	<i>0.3s</i>										
PDF Model (leptons)								2.7			
PDF Model (jets)	<i>1.1</i>							5.5			
Higher-order Diagrams		<i>10.0</i>	<i>10.0</i>	10.0		10.0			<b>10.0</b>	<b>10.0</b>	<b>10.0</b>
$\cancel{E}_T$ Modeling					19.0						
Conversion Modeling						6.8					
Jet Fake Rates											
(Low S/B)								15.0			
(High S/B)								24.0			
Jet Energy Scale	<i>3.1</i>	<i>6.2</i>	<i>3.5</i>	<i>28.2</i>	<i>18.0</i>	<i>3.5</i>		<i>5.7</i>	<i>9.9</i>	<i>5.3</i>	<i>12.9</i>
Lepton ID Efficiencies	<i>3.8</i>	<i>3.8</i>	<i>3.8</i>	<i>3.8</i>	<i>3.8</i>			<i>3.8</i>	<i>3.8</i>	<i>3.8</i>	<i>3.8</i>
Trigger Efficiencies	<i>2.0</i>	<i>2.0</i>	<i>2.0</i>	<i>2.0</i>	<i>2.0</i>			<i>2.0</i>	<i>2.0</i>	<i>2.0</i>	<i>2.0</i>
<b>Luminosity</b>	<i>5.9</i>	<i>5.9</i>	<i>5.9</i>	<i>5.9</i>	<i>5.9</i>			<i>5.9</i>	<i>5.9</i>	<i>5.9</i>	<i>5.9</i>

CDF:  $H \rightarrow W^+W^- \rightarrow \ell^\pm \ell'^\mp$  with one associated jet channel relative uncertainties (%)

Contribution	<i>WW</i>	<i>WZ</i>	<i>ZZ</i>	<i>t<math>\bar{t}</math></i>	DY	<i>W<math>\gamma</math></i>	<i>W+jet</i>	<i>gg <math>\rightarrow</math> H</i>	<i>WH</i>	<i>ZH</i>	VBF
<b>Cross Section</b>											
ScaleInclusive								0.0			
Scale1+Jets								35.0			
Scale2+Jets								-12.7			
PDF Model								17.3			
Total	<i>6.0</i>	<i>6.0</i>	<i>6.0</i>	<i>7.0</i>					<b>5.0</b>	<b>5.0</b>	10.0
<b>Acceptance</b>											
Scale (jets)	<i>-4.0s</i>										
PDF Model (leptons)								3.6			
PDF Model (jets)	<i>4.7</i>							-6.3			
Higher-order Diagrams		<i>10.0</i>	<i>10.0</i>	10.0		10.0			<b>10.0</b>	<b>10.0</b>	<b>10.0</b>
$\cancel{E}_T$ Modeling					21.0						
Conversion Modeling						6.8					
Jet Fake Rates											
(Low S/B)								16.0			
(High S/B)								27.0			
Jet Energy Scale	<i>-5.8</i>	<i>-1.1</i>	<i>-4.8</i>	<i>-13.1</i>	<i>-6.5</i>	<i>-9.5</i>		<i>-3.8</i>	<i>-8.5</i>	<i>-7.8</i>	<i>-6.8</i>
Lepton ID Efficiencies	<i>3.8</i>	<i>3.8</i>	<i>3.8</i>	<i>3.8</i>	<i>3.8</i>			<i>3.8</i>	<i>3.8</i>	<i>3.8</i>	<i>3.8</i>
Trigger Efficiencies	<i>2.0</i>	<i>2.0</i>	<i>2.0</i>	<i>2.0</i>	<i>2.0</i>			<i>2.0</i>	<i>2.0</i>	<i>2.0</i>	<i>2.0</i>
<b>Luminosity</b>	<i>5.9</i>	<i>5.9</i>	<i>5.9</i>	<i>5.9</i>	<i>5.9</i>			<i>5.9</i>	<i>5.9</i>	<i>5.9</i>	<i>5.9</i>

CDF:  $H \rightarrow W^+W^- \rightarrow \ell^\pm \ell'^\mp$  with two or more associated jets channel relative uncertainties (%)

Contribution	$WW$	$WZ$	$ZZ$	$t\bar{t}$	DY	$W\gamma$	$W+\text{jet}$	$gg \rightarrow H$	$WH$	$ZH$	VBF
<b>Cross Section</b>											
ScaleInclusive								0.0			
Scale1+Jets								0.0			
Scale2+Jets								33.0			
PDF Model								29.7			
Total	<i>6.0</i>	<i>6.0</i>	<i>6.0</i>	7.0					<b>5.0</b>	<b>5.0</b>	10.0
<b>Acceptance</b>											
Scale (jets)	<i>-8.2s</i>										
PDF Model (leptons)								4.8			
PDF Model (jets)	<i>4.2</i>							-12.3			
Higher-order Diagrams		<i>10.0</i>	<i>10.0</i>	10.0		10.0			<b>10.0</b>	<b>10.0</b>	<b>10.0</b>
$\cancel{E}_T$ Modeling					26.0						
Conversion Modeling						6.8					
Jet Fake Rates							19.0				
Jet Energy Scale	<i>-20.5</i>	<i>-13.2</i>	<i>-13.3</i>	<i>-1.7</i>	<i>-32.7</i>	<i>-22.0</i>		<i>-15.1</i>	<i>-4.0</i>	<i>-2.5</i>	<i>-3.8</i>
$b$ -tag Veto				3.6							
Lepton ID Efficiencies	<i>3.8</i>	<i>3.8</i>	<i>3.8</i>	<i>3.8</i>	<i>3.8</i>			<i>3.8</i>	<i>3.8</i>	<i>3.8</i>	<i>3.8</i>
Trigger Efficiencies	<i>2.0</i>	<i>2.0</i>	<i>2.0</i>	<i>2.0</i>	<i>2.0</i>			<i>2.0</i>	<i>2.0</i>	<i>2.0</i>	<i>2.0</i>
<b>Luminosity</b>	<i>5.9</i>	<i>5.9</i>	<i>5.9</i>	<i>5.9</i>	<i>5.9</i>			<i>5.9</i>	<i>5.9</i>	<i>5.9</i>	<i>5.9</i>

TABLE XX: Systematic uncertainties on the signal and background contributions for CDF's low- $M_{\ell\ell}$   $H \rightarrow W^+W^- \rightarrow \ell^\pm \ell'^\mp$  channel with zero or one associated jets. This channel is sensitive to only gluon fusion production. Systematic uncertainties are listed by name (see the original references for a detailed explanation of their meaning and on how they are derived). Systematic uncertainties for  $H$  shown in this table are obtained for  $m_H = 160$  GeV/ $c^2$ . Uncertainties are relative, in percent, and are symmetric unless otherwise indicated. The uncertainties associated with the different background and signal processed are correlated within individual categories unless otherwise noted. In these special cases, the correlated uncertainties are shown in either italics or bold face text.

CDF: low  $M_{\ell\ell}$   $H \rightarrow W^+W^- \rightarrow \ell^\pm \ell'^\mp$  with zero or one associated jets channel relative uncertainties (%)

Contribution	$WW$	$WZ$	$ZZ$	$t\bar{t}$	DY	$W\gamma$	$W+\text{jet}(s)$	$gg \rightarrow H$	$WH$	$ZH$	VBF
<b>Cross Section</b>											
ScaleInclusive								8.1			
Scale1+Jets								0.0			
Scale2+Jets								-5.1			
PDF Model								10.5			
Total	<i>6.0</i>	<i>6.0</i>	<i>6.0</i>	7.0	5.0				<b>5.0</b>	<b>5.0</b>	10.0
<b>Acceptance</b>											
Scale (jets)	<i>-0.4s</i>										
PDF Model (leptons)								1.0			
PDF Model (jets)	<i>1.6</i>							2.1			
Higher-order Diagrams		<i>10.0</i>	<i>10.0</i>	10.0	10.0				<b>10.0</b>	<b>10.0</b>	<b>10.0</b>
Conversion Modeling						8.4					
Jet Fake Rates							13.8				
Jet Energy Scale	<i>1.2</i>	<i>2.2</i>	<i>2.0</i>	<i>13.3</i>	<i>15.4</i>	<i>1.2</i>		<i>2.4</i>	<i>9.2</i>	<i>6.5</i>	<i>7.8</i>
Lepton ID Efficiencies	<i>3.8</i>	<i>3.8</i>	<i>3.8</i>	<i>3.8</i>	<i>3.8</i>			<i>3.8</i>	<i>3.8</i>	<i>3.8</i>	<i>3.8</i>
Trigger Efficiencies	<i>2.0</i>	<i>2.0</i>	<i>2.0</i>	<i>2.0</i>	<i>2.0</i>			<i>2.0</i>	<i>2.0</i>	<i>2.0</i>	<i>2.0</i>
<b>Luminosity</b>	<i>5.9</i>	<i>5.9</i>	<i>5.9</i>	<i>5.9</i>	<i>5.9</i>			<i>5.9</i>	<i>5.9</i>	<i>5.9</i>	<i>5.9</i>





TABLE XXII: Systematic uncertainties on the signal and background contributions for CDF's  $WH \rightarrow WWW \rightarrow \ell^\pm \ell'^\pm$  channel with one or more associated jets and  $WH \rightarrow WWW \rightarrow \ell^\pm \ell'^\pm \ell''^\mp$  channel. These channels are sensitive to only  $WH$  and  $ZH$  production. Systematic uncertainties are listed by name (see the original references for a detailed explanation of their meaning and on how they are derived). Systematic uncertainties for  $H$  shown in this table are obtained for  $m_H = 160 \text{ GeV}/c^2$ . Uncertainties are relative, in percent, and are symmetric unless otherwise indicated. The uncertainties associated with the different background and signal processed are correlated within individual categories unless otherwise noted. In these special cases, the correlated uncertainties are shown in either italics or bold face text.

CDF:  $WH \rightarrow WWW \rightarrow \ell^\pm \ell'^\pm$  channel relative uncertainties (%)

Contribution	$WW$	$WZ$	$ZZ$	$t\bar{t}$	DY	$W\gamma$	$W+\text{jet}$	$WH$	$ZH$
<b>Cross Section</b>									
Total	<i>6.0</i>	<i>6.0</i>	<i>6.0</i>	7.0	5.0			<b>5.0</b>	<b>5.0</b>
<b>Acceptance</b>									
Scale (jets)	-6.1								
PDF Model (jets)	5.7								
Higher-order Diagrams		<i>10.0</i>	<i>10.0</i>	10.0	10.0	10.0		<b>10.0</b>	<b>10.0</b>
Conversion Modeling						6.8			
Jet Fake Rates							37.7		
Charge Mismeasurement Rate	<i>25.0</i>				<i>25.0</i>				
Jet Energy Scale	<i>-4.1</i>	<i>-4.2s</i>	<i>-3.3s</i>	<i>-0.3</i>	<i>-4.9s</i>	<i>-9.1</i>		<i>-1.0s</i>	<i>-0.7s</i>
Lepton ID Efficiencies	<i>3.8</i>	<i>3.8</i>	<i>3.8</i>	<i>3.8</i>	<i>3.8</i>			<i>3.8</i>	<i>3.8</i>
Trigger Efficiencies	<i>2.0</i>	<i>2.0</i>	<i>2.0</i>	<i>2.0</i>	<i>2.0</i>			<i>2.0</i>	<i>2.0</i>
<b>Luminosity</b>	<i>5.9</i>	<i>5.9</i>	<i>5.9</i>	<i>5.9</i>	<i>5.9</i>			<i>5.9</i>	<i>5.9</i>

CDF:  $WH \rightarrow WWW \rightarrow \ell^\pm \ell'^\pm \ell''^\mp$  channel relative uncertainties (%)

Contribution	$WZ$	$ZZ$	$Z\gamma$	$t\bar{t}$	Fakes	$WH$	$ZH$
<b>Cross Section</b>							
Total	<i>6.0</i>	<i>6.0</i>	10.0	7.0		<b>5.0</b>	<b>5.0</b>
<b>Acceptance</b>							
Higher-order Diagrams	<i>10.0</i>	<i>10.0</i>	15.0	10.0		<b>10.0</b>	<b>10.0</b>
Jet Fake Rates					22.3		
$b$ -Jet Fake Rates				27.3			
Jet Energy Scale			<i>-3.0</i>				
Lepton ID Efficiencies	<i>5.0</i>	<i>5.0</i>	<i>5.0</i>	<i>5.0</i>		<i>5.0</i>	<i>5.0</i>
Trigger Efficiencies	<i>2.0</i>	<i>2.0</i>	<i>2.0</i>	<i>2.0</i>		<i>2.0</i>	<i>2.0</i>
<b>Luminosity</b>	<i>5.9</i>	<i>5.9</i>	<i>5.9</i>	<i>5.9</i>		<i>5.9</i>	<i>5.9</i>

TABLE XXIII: Systematic uncertainties on the signal and background contributions for CDF's  $ZH \rightarrow ZWW \rightarrow \ell^\pm \ell^\mp \ell'^\pm$  channels with 1 jet and 2 or more jets. These channels are sensitive to only  $WH$  and  $ZH$  production. Systematic uncertainties are listed by name (see the original references for a detailed explanation of their meaning and on how they are derived). Systematic uncertainties for  $H$  shown in this table are obtained for  $m_H = 160 \text{ GeV}/c^2$ . Uncertainties are relative, in percent, and are symmetric unless otherwise indicated. The uncertainties associated with the different background and signal processed are correlated within individual categories unless otherwise noted. In these special cases, the correlated uncertainties are shown in either italics or bold face text.

CDF:  $ZH \rightarrow ZWW \rightarrow \ell^\pm \ell^\mp \ell'^\pm$  with one associated jet channel relative uncertainties (%)

Contribution	$WZ$	$ZZ$	$Z\gamma$	$t\bar{t}$	Fakes	$WH$	$ZH$
<b>Cross Section</b>							
Total	<i>6.0</i>	<i>6.0</i>	10.0	7.0		<b>5.0</b>	<b>5.0</b>
<b>Acceptance</b>							
Higher-order Diagrams	<i>10.0</i>	<i>10.0</i>	15.0	10.0		<b>10.0</b>	<b>10.0</b>
Jet Fake Rates					23.6		
$b$ -Jet Fake Rates				42.0			
Jet Energy Scale	<i>-7.8</i>	<i>-2.4</i>	<i>-6.4</i>	<i>2.2</i>		<i>-7.0</i>	<i>7.1</i>
Lepton ID Efficiencies	<i>5.0</i>	<i>5.0</i>	<i>5.0</i>	<i>5.0</i>		<i>5.0</i>	<i>5.0</i>
Trigger Efficiencies	<i>2.0</i>	<i>2.0</i>	<i>2.0</i>	<i>2.0</i>		<i>2.0</i>	<i>2.0</i>
<b>Luminosity</b>	<i>5.9</i>	<i>5.9</i>	<i>5.9</i>	<i>5.9</i>		<i>5.9</i>	<i>5.9</i>

CDF:  $ZH \rightarrow ZWW \rightarrow \ell^\pm \ell^\mp \ell'^\pm$  with two or more associated jets channel relative uncertainties (%)

Contribution	$WZ$	$ZZ$	$Z\gamma$	$t\bar{t}$	Fakes	$WH$	$ZH$
<b>Cross Section</b>							
Total	<i>6.0</i>	<i>6.0</i>	10.0	7.0		<b>5.0</b>	<b>5.0</b>
<b>Acceptance</b>							
Higher-order Diagrams	<i>10.0</i>	<i>10.0</i>	15.0	10.0		<b>10.0</b>	<b>10.0</b>
Jet Fake Rates					18.4		
$b$ -Jet Fake Rates				22.2			
Jet Energy Scale	<i>-18.0</i>	<i>-15.4</i>	<i>-16.8</i>	<i>-2.3</i>		<i>-20.1</i>	<i>-5.5</i>
Lepton ID Efficiencies	<i>5.0</i>	<i>5.0</i>	<i>5.0</i>	<i>5.0</i>		<i>5.0</i>	<i>5.0</i>
Trigger Efficiencies	<i>2.0</i>	<i>2.0</i>	<i>2.0</i>	<i>2.0</i>		<i>2.0</i>	<i>2.0</i>
<b>Luminosity</b>	<i>5.9</i>	<i>5.9</i>	<i>5.9</i>	<i>5.9</i>		<i>5.9</i>	<i>5.9</i>

TABLE XXIV: Systematic uncertainties on the signal and background contributions for D0's  $H \rightarrow W^+W^- \rightarrow \ell^\pm \ell^\mp$  channels. Systematic uncertainties are listed by name; see the original references for a detailed explanation of their meaning and on how they are derived. Shape uncertainties are labeled with the "s" designation. Systematic uncertainties given in this table are obtained for the  $m_H = 165 \text{ GeV}/c^2$  Higgs selection. Cross section uncertainties on the  $gg \rightarrow H$  signal depend on the jet multiplicity, as described in the main text. Uncertainties are relative, in percent, and are symmetric unless otherwise indicated.

$H \rightarrow W^+W^- \rightarrow \ell^\pm \ell^\mp$  channels relative uncertainties (%)

Contribution	Dibosons	$Z/\gamma^* \rightarrow \ell\ell$	$W+\text{jet}/\gamma$	$t\bar{t}$	Multijet	$gg \rightarrow H$	$qq \rightarrow qqH$	$VH$
Luminosity/Normalization	4	-	4	4	4	4	4	4
Cross Section (Scale/PDF)	5-7	-	-	7	-	13-33/8-30	5	6
$Z/\gamma^* \rightarrow \ell\ell$ n-jet norm	-	2-15	-	-	-	-	-	-
$Z/\gamma^* \rightarrow \ell\ell$ MET model	-	5-19	-	-	-	-	-	-
$W+\text{jet}/\gamma$ norm	-	-	6-30	-	-	-	-	-
$W+\text{jet}/\gamma$ ISR/FSR model (s)	-	-	2-20	-	-	-	-	-
Vertex Confirmation (s)	1-5	1-5	1-5	5-6	-	1-5	1-5	1-5
Jet identification (s)	1	1	1	1	-	1	1	1
Jet Energy Scale (s)	1-5	1-5	1-5	1-4	-	1-5	1-5	1-4
Jet Energy Resolution(s)	1-4	1-4	1-4	1-4	-	1-3	1-4	1-3
B-tagging (s)	-	-	-	1-5	-	-	-	-

TABLE XXV: Systematic uncertainties on the signal and background contributions for D0's  $H \rightarrow W^+W^- \rightarrow \mu\nu\tau_{\text{had}}\nu$  channel. Systematic uncertainties are listed by name; see the original references for a detailed explanation of their meaning and on how they are derived. Shape uncertainties are labeled with the shape designation (S). Systematic uncertainties shown in this table are obtained for the  $m_H = 165 \text{ GeV}/c^2$  Higgs selection. Uncertainties are relative, in percent, and are symmetric unless otherwise indicated.

D0:  $H \rightarrow W^+W^- \rightarrow \mu\nu\tau_{\text{had}}\nu$  channel relative uncertainties (%)

Contribution	Diboson	$Z/\gamma^* \rightarrow \ell\ell$	$W+\text{jets}$	$t\bar{t}$	Multijet	$gg \rightarrow H$	$qq \rightarrow qqH$	$VH$
Luminosity ( $\sigma_{\text{inel}}(pp)$ )	4.6	4.6	-	4.6	-	4.6	4.6	4.6
Luminosity Monitor	4.1	4.1	-	4.1	-	4.1	4.1	4.1
Trigger	5.0	5.0	-	5.0	-	5.0	5.0	5.0
Lepton ID	3.7	3.7	-	3.7	-	3.7	3.7	3.7
EM veto	5.0	-	-	5.0	-	5.0	5.0	5.0
Tau Energy Scale (S)	1.0	1.1	-	<1	-	<1	<1	<1
Jet Energy Scale (S)	8.0	<1	-	1.8	-	2.5	2.5	2.5
Jet identification (S)	<1	<1	-	7.5	-	5.0	5.0	5.0
Multijet (S)	-	-	-	-	20-50	-	-	-
Cross Section (scale/PDF)	7.0	4.0	-	10	-	7/8	4.9	6.1
Signal Branching Fraction	-	-	-	-	-	0-7.3	0-7.3	0-7.3
Modeling	1.0	-	10	-	-	3.0	3.0	3.0

TABLE XXVI: Systematic uncertainties on the signal and background contributions for D0’s  $VH \rightarrow e^\pm \nu_e \mu^\pm \nu_\mu$  ( $V = W, Z$ ) channels. Systematic uncertainties are listed by name; see the original references for a detailed explanation of their meaning and on how they are derived. Shape uncertainties are labeled with the “shape” designation. Systematic uncertainties shown in this table are obtained for the  $m_H = 165$  GeV/ $c^2$  Higgs selection. Uncertainties are relative, in percent, and are symmetric unless otherwise indicated.

Contribution	VH	$Z + jet/\gamma$	$W + jet/\gamma$	$t\bar{t}$	Diboson	Multijet
Cross section	6.2	–	–	6	7	–
Luminosity/Normalization	4	–	4	4	4	–
Multijet	–	–	–	–	–	30
Trigger	2	2	2	2	2	2
Charge flip	–	50	–	50	50	–
W+jets/ $\gamma$	–	–	10	–	–	–
$W - p_T$ model	–	–	shape	–	–	–
$Z - p_T$ model	–	shape	–	–	–	–
W+jets/ $\gamma$ ISR/FSR model	–	–	shape	–	–	–

TABLE XXVII: Systematic uncertainties on the signal and background contributions for D0’s  $VH \rightarrow VWW \rightarrow ee\mu, \mu\mu e$  channels. Systematic uncertainties are listed by name; see the original references for a detailed explanation of their meaning and on how they are derived. Shape uncertainties are labeled with the “s” designation. Systematic uncertainties given in this table are obtained for the  $m_H = 145$  GeV Higgs selection. Uncertainties are relative, in percent, and are symmetric unless otherwise indicated. Jet shape uncertainties are applied to the  $\mu\mu e$  channel only.

Contribution	Dibosons	$Z/\gamma^* \rightarrow \ell\ell$	$W+jet/\gamma$	$t\bar{t}$	$Z\gamma$	$VH$	$gg \rightarrow H$	$qq \rightarrow qqH$
Luminosity	6.1	6.1	6.1	6.1	–	6.1	6.1	6.1
Cross Section (Scale/PDF)	6	6	6	7	–	6.2	7	4.9
PDF	2.5	2.5	2.5	2.5	–	2.5	2.5	2.5
Electron Identification	2.5	2.5	2.5	2.5	–	2.5	2.5	2.5
Muon Identification	4	4	4	4	–	4	4	4
Trigger	3.5	3.5	3.5	3.5	–	3.5	3.5	3.5
$Z\gamma$	–	–	–	–	9.5	–	–	–
$V + jets$ lepton fake rate	–	30	30	–	–	–	–	–
$Z-p_T$ reweighting (s)	–	$\pm 1\sigma$	–	–	–	–	–	–
Electron smearing (s)	$\pm 1\sigma$	$\pm 1\sigma$	$\pm 1\sigma$	$\pm 1\sigma$	–	$\pm 1\sigma$	$\pm 1\sigma$	$\pm 1\sigma$
Muon smearing (s)	$\pm 1\sigma$	$\pm 1\sigma$	$\pm 1\sigma$	$\pm 1\sigma$	–	$\pm 1\sigma$	$\pm 1\sigma$	$\pm 1\sigma$
Jet Shape systematics below applied to $\mu\mu e$ channel only								
Jet Energy Scale (s)	$\pm 1\sigma$	$\pm 1\sigma$	$\pm 1\sigma$	$\pm 1\sigma$	–	$\pm 1\sigma$	$\pm 1\sigma$	$\pm 1\sigma$
Jet Energy Resolution (s)	$\pm 1\sigma$	$\pm 1\sigma$	$\pm 1\sigma$	$\pm 1\sigma$	–	$\pm 1\sigma$	$\pm 1\sigma$	$\pm 1\sigma$
Jet Identification (s)	$-1\sigma$	$-1\sigma$	$-1\sigma$	$-1\sigma$	–	$-1\sigma$	$-1\sigma$	$-1\sigma$
Vertex Confirmation (s)	$-1\sigma$	$-1\sigma$	$-1\sigma$	$-1\sigma$	–	$-1\sigma$	$-1\sigma$	$-1\sigma$

TABLE XXVIII: Systematic uncertainties on the signal and background contributions for D0's  $\tau\tau\mu + X$  channel. Systematic uncertainties are listed by name; see the original references for a detailed explanation of their meaning and on how they are derived. Shape uncertainties are labeled with the "s" designation. Cross section uncertainties on the  $gg \rightarrow H$  signal depend on the jet multiplicity, as described in the main text. Uncertainties are relative, in percent, and are symmetric unless otherwise indicated.

Contribution	Dibosons	$Z/\gamma^*$	$t\bar{t}$	Instrumental	$gg \rightarrow H$	$qq \rightarrow qqH$	$VH$
Luminosity/Normalization	6	6	6	24	6	6	6
Trigger	3	3	3	–	3	3	3
Cross Section (Scale/PDF)	7	6	10	–	13-33/7.6-30	4.9	6.2
PDF	2.5	2.5	2.5	–	2.5	2.5	2.5
Tau Id per $\tau$ (Type 1/2/3)	7/3.5/5	7/3.5/5	7/3.5/5	–	7/3.5/5	7/3.5/5	7/3.5/5
Tau Energy Scale	1	1	1	–	1	1	1
Tau Track Match per $\tau$	1.4	1.4	1.4	–	1.4	1.4	1.4
Muon Identification	2.9	2.9	2.9	–	2.9	2.9	2.9

TABLE XXIX: Systematic uncertainties on the signal and background contributions for D0's  $H \rightarrow WW^* \rightarrow \ell\nu jj$  electron and muon channels. Systematic uncertainties are listed by name; see the original references for a detailed explanation of their meaning and on how they are derived. Signal uncertainties are shown for  $m_H = 160 \text{ GeV}/c^2$  for all channels except for  $WH$ , shown for  $m_H = 115 \text{ GeV}/c^2$ . Those affecting the shape of the RF discriminant are indicated with "Y." Uncertainties are listed as relative changes in normalization, in percent, except for those also marked by "S," where the overall normalization is constant, and the value given denotes the maximum percentage change from nominal in any region of the distribution.

Contribution	Shape	$W$ +jets	$Z$ +jets	Top	Diboson	$gg \rightarrow H$	$qq \rightarrow qqH$	$WH$
Jet energy scale	Y	$(+6.7)_{-5.4}^S$	$< 0.1$	$\pm 0.7$	$\pm 3.3$	$(+5.7)_{-4.0}$	$\pm 1.5$	$(+2.7)_{-2.3}$
Jet identification	Y	$\pm 6.6^S$	$< 0.1$	$\pm 0.5$	$\pm 3.8$	$\pm 1.0$	$\pm 1.1$	$\pm 1.0$
Jet resolution	Y	$(+6.6)_{-4.1}^S$	$< 0.1$	$\pm 0.5$	$(+1.0)_{-0.5}$	$(+3.0)_{-0.5}$	$\pm 0.8$	$\pm 1.0$
Association of jets with PV	Y	$\pm 3.2^S$	$\pm 1.3^S$	$\pm 1.2$	$\pm 3.2$	$\pm 2.9$	$\pm 2.4$	$(+0.9)_{-0.2}$
Luminosity	N	n/a	n/a	$\pm 6.1$	$\pm 6.1$	$\pm 6.1$	$\pm 6.1$	$\pm 6.1$
Muon trigger	Y	$\pm 0.4^S$	$< 0.1$	$< 0.1$	$< 0.1$	$< 0.1$	$< 0.1$	$< 0.1$
Electron identification	N	$\pm 4.0$	$\pm 4.0$	$\pm 4.0$	$\pm 4.0$	$\pm 4.0$	$\pm 4.0$	$\pm 4.0$
Muon identification	N	$\pm 4.0$	$\pm 4.0$	$\pm 4.0$	$\pm 4.0$	$\pm 4.0$	$\pm 4.0$	$\pm 4.0$
ALPGEN tuning	Y	$\pm 1.1^S$	$\pm 0.3^S$	n/a	n/a	n/a	n/a	n/a
Cross Section	N	$\pm 6$	$\pm 6$	$\pm 10$	$\pm 7$	$\pm 10$	$\pm 10$	$\pm 6$
Heavy-flavor fraction	Y	$\pm 20$	$\pm 20$	n/a	n/a	n/a	n/a	n/a
Signal Branching Fraction	N	n/a	n/a	n/a	n/a	0-7.3	0-7.3	0-7.3
PDF	Y	$\pm 2.0^S$	$\pm 0.7^S$	$< 0.1^S$	$< 0.1^S$	$< 0.1^S$	$< 0.1^S$	$< 0.1^S$
Multijet Background	Y	Electron channel			Muon channel			
		$\pm 6.5$			$\pm 26$			

TABLE XXX: Systematic uncertainties on the signal and background contributions for CDF's  $H \rightarrow \ell^\pm \ell^\mp \ell'^\pm \ell'^\mp$  channel. This channel is sensitive to gluon fusion production and  $WH$ ,  $ZH$  and VBF production. Systematic uncertainties are listed by name (see the original references for a detailed explanation of their meaning and on how they are derived). Uncertainties are relative, in percent, and are symmetric unless otherwise indicated. The uncertainties associated with the different background and signal processed are correlated unless otherwise noted. Boldface and italics indicate groups of uncertainties which are correlated with each other but not the others within a line. Shape uncertainties are labeled with an "s".

CDF:  $H \rightarrow \ell^\pm \ell^\mp \ell'^\pm \ell'^\mp$  channel relative uncertainties (%)

Contribution	$ZZ$	$Z(/\gamma^*)+\text{jets}$	$gg \rightarrow H$	$WH$	$ZH$	VBF
<b>Cross Section :</b>						
Scale			7.0			
PDF Model			7.7			
Total	<i>10.0</i>			<b>5.0</b>	<b>5.0</b>	10.0
$\mathcal{BR}(H \rightarrow VV)$			3.0	3.0	3.0	3.0
<b>Acceptance :</b>						
PDF Model	2.7					
Higher-order Diagrams	2.5					
Jet Fake Rates		50.0				
$\cancel{E}_T$ Resolution	s		s		s	s
Lepton ID Efficiencies	<i>3.6</i>		<i>3.6</i>	<i>3.6</i>	<i>3.6</i>	<i>3.6</i>
Trigger Efficiencies	<i>0.4</i>		<i>0.5</i>	<i>0.5</i>	<i>0.5</i>	<i>0.5</i>
Luminosity	<i>5.9</i>		<i>5.9</i>	<i>5.9</i>	<i>5.9</i>	<i>5.9</i>

TABLE XXXI: Systematic uncertainties on the signal and background contributions for CDF's  $t\bar{t}H \rightarrow \ell + \text{jets}$  channels. Systematic uncertainties are listed by name; see the original references for a detailed explanation of their meaning and on how they are derived. Systematic uncertainties for  $t\bar{t}H$  shown in this table are obtained for  $m_H = 115 \text{ GeV}/c^2$ . Uncertainties are relative, in percent, and are symmetric unless otherwise indicated.

CDF:  $t\bar{t}H \ell + \cancel{E}_T$  4 jets channel relative uncertainties (%)

Contribution	1 tight, 1 loose		1 tight, $\geq 2$ loose		2 tight, 0 loose		2 tight, $\geq 1$ loose		$\geq 3$ tight, $\geq 0$ loose	
	$t\bar{t}$	$t\bar{t}H$	$t\bar{t}$	$t\bar{t}H$	$t\bar{t}$	$t\bar{t}H$	$t\bar{t}$	$t\bar{t}H$	$t\bar{t}$	$t\bar{t}H$
$t\bar{t}$ Cross Section		10		10		10		10		10
$t\bar{t}H$ Cross Section	10		10		10		10		10	
Luminosity ( $\sigma_{\text{inel}}(p\bar{p})$ )	3.8	3.8	3.8	3.8	3.8	3.8	3.8	3.8	3.8	3.8
Luminosity Monitor	4.4	4.4	4.4	4.4	4.4	4.4	4.4	4.4	4.4	4.4
$B$ -Tag Efficiency	+1.79 -1.89	-0.23 -0.86	+4.77 -4.75	-1.74 -1.84	+9.09 -9.75	+7.50 -5.98	+14.42 -9.41	+5.14 -6.72	+14.79 -19.02	+15.46 -14.28
Mistag Rate	+1.89 -0.72	+1.09 -0.11	+12.41 -6.71	+5.14 -4.84	-0.27 +0.64	-0.14 +0.39	+9.61 -3.56	+1.92 +1.75	+2.99 -5.14	+1.13 -1.37
Jet Energy Scale	+2.77 -4.38	-8.80 +8.06	+3.57 -0.33	-8.33 +11.92	+2.52 -3.80	-9.06 +7.42	+3.77 -0.48	-9.77 +8.77	+1.48 -2.61	-5.66 +6.74
ISR+FSR+PDF	0.36	3.04	0.38	0.75	1.29	2.73	3.86	5.28	0.33	5.13

CDF:  $t\bar{t}H \ell + \cancel{E}_T$  5 jets channel relative uncertainties (%)

Contribution	1 tight, 1 loose		1 tight, $\geq 2$ loose		2 tight, 0 loose		2 tight, $\geq 1$ loose		$\geq 3$ tight, $\geq 0$ loose	
	$t\bar{t}$	$t\bar{t}H$	$t\bar{t}$	$t\bar{t}H$	$t\bar{t}$	$t\bar{t}H$	$t\bar{t}$	$t\bar{t}H$	$t\bar{t}$	$t\bar{t}H$
$t\bar{t}$ Cross Section		10		10		10		10		10
$t\bar{t}H$ Cross Section	10		10		10		10		10	
Luminosity ( $\sigma_{\text{inel}}(p\bar{p})$ )	3.8	3.8	3.8	3.8	3.8	3.8	3.8	3.8	3.8	3.8
Luminosity Monitor	4.4	4.4	4.4	4.4	4.4	4.4	4.4	4.4	4.4	4.4
$B$ -Tag Efficiency	+1.25 -0.55	-1.96 +2.06	+1.99 -5.21	-0.99 +0.89	+8.69 -9.74	+5.80 -7.30	+11.36 -12.13	+4.48 -4.50	+14.94 -16.28	+12.96 -15.87
Mistag Rate	+2.81 -0.78	+1.96 -0.66	+12.47 -11.50	+1.19 -2.53	-1.94 +0.92	-0.57 -0.77	+10.70 -7.19	+0.87 -2.66	+4.02 -9.48	+1.15 -0.23
Jet Energy Scale	+14.48 -11.71	-1.02 +2.51	+9.96 -12.79	-0.64 -1.34	+11.84 -13.49	-2.21 +0.66	+13.07 -9.15	-3.40 +1.48	+6.51 -7.57	-3.12 +2.45
ISR+FSR+PDF	3.42	2.41	11.28	0.79	5.24	2.30	3.89	3.26	3.95	2.88

CDF:  $t\bar{t}H \ell + \cancel{E}_T$  6 or more jets channel relative uncertainties (%)

Contribution	1 tight, 1 loose		1 tight, $\geq 2$ loose		2 tight, 0 loose		2 tight, $\geq 1$ loose		$\geq 3$ tight, $\geq 0$ loose	
	$t\bar{t}$	$t\bar{t}H$	$t\bar{t}$	$t\bar{t}H$	$t\bar{t}$	$t\bar{t}H$	$t\bar{t}$	$t\bar{t}H$	$t\bar{t}$	$t\bar{t}H$
$t\bar{t}$ Cross Section		10		10		10		10		10
$t\bar{t}H$ Cross Section	10		10		10		10		10	
Luminosity ( $\sigma_{\text{inel}}(p\bar{p})$ )	3.8	3.8	3.8	3.8	3.8	3.8	3.8	3.8	3.8	3.8
Luminosity Monitor	4.4	4.4	4.4	4.4	4.4	4.4	4.4	4.4	4.4	4.4
$B$ -Tag Efficiency	+1.52 -1.47	-2.07 +1.85	+4.07 -1.53	-0.89 +2.99	+9.02 -8.39	+4.27 -8.07	+17.30 -8.32	+4.78 -3.91	+12.00 -14.59	+13.13 -12.00
Mistag Rate	+1.76 -2.29	+1.72 +0.21	+17.63 -16.95	+4.43 -3.03	-1.46 +2.68	-2.55 -1.33	+15.68 -12.32	+2.25 +0.98	+8.47 -11.76	-0.12 -2.05
Jet Energy Scale	+25.07 -21.07	+12.17 -12.62	+17.29 -20.68	+11.78 -9.86	+25.58 -22.19	+10.81 -13.16	+26.49 -17.30	+10.02 -8.69	+23.29 -19.76	+8.58 -11.05
ISR+FSR+PDF	13.17	0.75	17.33	2.32	12.38	1.42	20.89	1.15	14.84	0.38

TABLE XXXII: Systematic uncertainties on the signal and background contributions for CDF's  $t\bar{t}H$  2-tag and 3-tag  $\cancel{E}_T$ +jets channels. Systematic uncertainties are listed by name; see the original references for a detailed explanation of their meaning and on how they are derived. Systematic uncertainties for  $t\bar{t}H$  shown in this table are obtained for  $m_H = 120 \text{ GeV}/c^2$ . Uncertainties are relative, in percent, and are symmetric unless otherwise indicated.

CDF:  $t\bar{t}H$   $\cancel{E}_T$ +jets 2-tag channel relative uncertainties (%)

Contribution	non- $t\bar{t}$	$t\bar{t}$	$t\bar{t}H$
Luminosity ( $\sigma_{\text{inel}}(p\bar{p})$ )	0	3.8	3.8
Luminosity Monitor	0	4.4	4.4
Jet Energy Scale	0	2	11
Trigger Efficiency	0	7	7
$B$ -Tag Efficiency	0	7	7
ISR/FSR	0	2	2
PDF	0	2	2
$t\bar{t}$ Cross Section	0	10	0
$t\bar{t}b\bar{b}$ Cross Section	0	3	0
Signal Cross Section	0	0	10
Background Modeling	6	0	0
Background $B$ -tagging	5	0	0

CDF:  $t\bar{t}H$   $\cancel{E}_T$ +jets 3-tag channel relative uncertainties (%)

Contribution	non- $t\bar{t}$	$t\bar{t}$	$t\bar{t}H$
Luminosity ( $\sigma_{\text{inel}}(p\bar{p})$ )	0	3.8	3.8
Luminosity Monitor	0	4.4	4.4
Jet Energy Scale	0	3	13
Trigger Efficiency	0	7	7
$B$ -Tag Efficiency	0	9	9
ISR/FSR	0	2	2
PDF	0	2	2
$t\bar{t}$ Cross Section	0	10	0
$t\bar{t}b\bar{b}$ Cross Section	0	5	0
Signal Cross Section	0	0	10
Background Modeling	6	0	0
Background $B$ -tagging	10	0	0



TABLE XXXIII: Systematic uncertainties on the signal and background contributions for CDF's  $t\bar{t}H$  2-tag and 3-tag all jets channels. Systematic uncertainties are listed by name; see the original references for a detailed explanation of their meaning and on how they are derived. Systematic uncertainties for  $t\bar{t}H$  shown in this table are obtained for  $m_H = 120 \text{ GeV}/c^2$ . Uncertainties are relative, in percent, and are symmetric unless otherwise indicated.

CDF:  $t\bar{t}H$  all jets 2-tag channel relative uncertainties (%)

Contribution	non- $t\bar{t}$	$t\bar{t}$	$t\bar{t}H$
Luminosity ( $\sigma_{\text{inel}}(p\bar{p})$ )	0	3.8	3.8
Luminosity Monitor	0	4.4	4.4
Jet Energy Scale	0	11	20
Trigger Efficiency	0	7	7
$B$ -Tag Efficiency	0	7	7
ISR/FSR	0	2	2
PDF	0	2	2
$t\bar{t}$ Cross Section	0	10	0
$t\bar{t}b\bar{b}$ Cross Section	0	3	0
Signal Cross Section	0	0	10
Background Modeling	9	0	0
Background $B$ -tagging	5	0	0

CDF:  $t\bar{t}H$  all jets 3-tag channel relative uncertainties (%)

Contribution	non- $t\bar{t}$	$t\bar{t}$	$t\bar{t}H$
Luminosity ( $\sigma_{\text{inel}}(p\bar{p})$ )	0	3.8	3.8
Luminosity Monitor	0	4.4	4.4
Jet Energy Scale	0	13	22
Trigger Efficiency	0	7	7
$B$ -Tag Efficiency	0	9	9
ISR/FSR	0	2	2
PDF	0	2	2
$t\bar{t}$ Cross Section	0	10	0
$t\bar{t}b\bar{b}$ Cross Section	0	6	0
Signal Cross Section	0	0	10
Background Modeling	9	0	0
Background $B$ -tagging	10	0	0

TABLE XXXIV: Systematic uncertainties on the signal and background contributions for CDF's  $H \rightarrow \tau^+\tau^-$  channels. Systematic uncertainties are listed by name; see the original references for a detailed explanation of their meaning and on how they are derived. Systematic uncertainties for the Higgs signal shown in these tables are obtained for  $m_H = 120 \text{ GeV}/c^2$ . Uncertainties are relative, in percent, and are symmetric unless otherwise indicated. Shape uncertainties are labeled with an "S".

CDF:  $H \rightarrow \tau^+\tau^- (e/\mu + \tau_{had})$  channel relative uncertainties (%)

Contribution	$Z/\gamma^* \rightarrow \tau\tau$	$Z/\gamma^* \rightarrow ee$	$Z/\gamma^* \rightarrow \mu\mu$	$t\bar{t}$	diboson	fakes from SS	W+jets	$WH$	$ZH$	VBF	$gg \rightarrow H$
PDF Uncertainty	-	-	-	-	-	-	-	1.2	0.9	2.2	4.9
ISR/FSR 1 JET	-	-	-	-	-	-	-	6.7	8.7	8.8	3.6
ISR/FSR $\geq 2$ JETS	-	-	-	-	-	-	-	4.8	3.8	3.9	19.1
JES (S) 1 JET	9.5	8.5	8.5	14.5	0.5	-	4.2	2.8	6.4	6.5	4.3
JES (S) $\geq 2$ JETS	18.9	22.3	22.3	1.3	10.7	-	15.4	5.1	3.9	3.7	14.5
Normalization 1 JET	2.0	5.0	5.0	10.0	6.0	1.3	14.8	5.0	5.0	10.0	23.5
Normalization $\geq 2$ JETS	2.0	5.0	5.0	10.0	6.0	2.5	14.8	5.0	5.0	10.0	33.0
$\varepsilon_{trig}$ (e leg)	0.3	0.3	-	0.3	0.3	-	-	0.3	0.3	0.3	0.3
$\varepsilon_{trig}$ ( $\mu$ leg)	1.0	-	1.0	1.0	1.0	-	-	1.0	1.0	1.0	1.0
$\varepsilon_{trig}$ ( $\tau$ leg)	3.0	3.0	3.0	3.0	3.0	-	-	3.0	3.0	3.0	3.0
$\varepsilon_{IDe}$	2.4	2.4	-	2.4	2.4	-	-	2.4	2.4	2.4	2.4
$\varepsilon_{ID\mu}$	2.6	-	2.6	2.6	2.6	-	-	2.6	2.6	2.6	2.6
$\varepsilon_{ID\tau}$	3.0	3.0	3.0	3.0	3.0	-	-	3.0	3.0	3.0	3.0
$\varepsilon_{vtx}$	0.5	0.5	0.5	0.5	0.5	-	-	0.5	0.5	0.5	0.5
Luminosity	5.9	5.9	5.9	5.9	5.9	-	-	5.9	5.9	5.9	5.9

TABLE XXXV: Systematic uncertainties on the signal and background contributions for CDF's  $WH \rightarrow \ell\nu\tau^+\tau^-$  and  $ZH \rightarrow \ell^+\ell^-\tau^+\tau^-$  channels. Systematic uncertainties are listed by name; see the original references for a detailed explanation of their meaning and on how they are derived. Systematic uncertainties for the Higgs signal shown in these tables are obtained for  $m_H = 120 \text{ GeV}/c^2$ . Uncertainties are relative, in percent, and are symmetric unless otherwise indicated.

CDF:  $WH \rightarrow \ell\nu\tau^+\tau^-$  and  $ZH \rightarrow \ell^+\ell^-\tau^+\tau^- \ell\ell\tau_h + X$  channel relative uncertainties (%)

Contribution	$ZZ$	$WZ$	$WW$	$DY(ee)$	$DY(\mu\mu)$	$DY(\tau\tau)$	$Z\gamma$	$t\bar{t}$	$W\gamma$	$W + jet$	$WH$	$ZH$	$VBF$	$gg \rightarrow H$
Luminosity	5.9	5.9	5.9	5.9	5.9	5.9	5.9	5.9	5.9	5.9	5.9	5.9	5.9	5.9
Cross Section	11.7	11.7	11.7	5.0	5.0	5.0	11.7	14.1	11.7	5.0	5.0	5.0	10.0	10.0
Z-vertex Cut Efficiency	0.5	0.5	0.5	0.5	0.5	0.5	0.5	0.5	0.5	0.5	0.5	0.5	0.5	0.5
Trigger Efficiency	1.1	1.1	1.0	1.0	1.0	1.1	1.1	1.0	0.8	1.0	1.2	1.2	1.2	1.1
Lepton ID Efficiency	2.4	2.3	2.4	2.4	2.4	2.4	2.4	2.4	2.3	2.4	2.4	2.4	2.4	2.4
Lepton Fake Rate	10.7	8.0	26.7	26.0	26.6	15.1	27.1	22.4	22.8	28.7	2.9	2.3	15.1	13.6
Jet Energy Scale	1.3	1.1	0.0	3.2	5.1	0.6	6.6	0.1	2.0	0.2	0.1	0.03	0.6	0.4
MC stat	3.7	2.9	7.6	1.5	1.7	2.2	4.1	3.1	20.0	3.1	1.5	1.4	3.8	9.4
PDF Model	-	-	-	-	-	-	-	-	-	-	1.2	0.9	2.2	4.9
ISR/FSR Uncertainties	-	-	-	-	-	-	-	-	-	-	1.3	2.1	0.6	0.2

CDF:  $WH \rightarrow \ell\nu\tau^+\tau^-$  and  $ZH \rightarrow \ell^+\ell^-\tau^+\tau^- e\mu\tau_h + X$  channel relative uncertainties (%)

Contribution	$ZZ$	$WZ$	$WW$	$DY(ee)$	$DY(\mu\mu)$	$DY(\tau\tau)$	$Z\gamma$	$t\bar{t}$	$W\gamma$	$W + jet$	$WH$	$ZH$	$VBF$	$gg \rightarrow H$
Luminosity	5.9	5.9	5.9	5.9	5.9	5.9	5.9	5.9	5.9	5.9	5.9	5.9	5.9	5.9
Cross Section	11.7	11.7	11.7	5.0	5.0	5.0	11.7	14.1	11.7	5.0	5.0	5.0	10.0	10.0
Z-vertex Cut Efficiency	0.5	0.5	0.5	0.5	0.5	0.5	0.5	0.5	0.5	0.5	0.5	0.5	0.5	0.5
Trigger Efficiency	1.4	1.4	1.1	1.1	1.3	1.1	1.4	1.1	1.0	0.7	1.3	1.3	1.2	1.2
Lepton ID Efficiency	2.4	2.4	2.4	2.4	2.4	2.4	2.4	2.4	2.4	2.4	2.4	2.4	2.4	2.4
Lepton Fake Rate	9.0	6.5	26.6	20.8	31.4	25.2	39.4	27.8	19.3	41.9	1.6	2.5	28.5	29.2
Jet Energy Scale	0.0	0.3	2.2	0.0	0.8	1.5	0.5	0.8	0.0	0.0	0.2	0.1	1.7	0.0
MC stat	12.9	7.2	20.9	57.7	12.6	7.7	10.2	12.4	35.4	25.8	2.1	3.9	13.0	44.7
PDF Model	-	-	-	-	-	-	-	-	-	-	1.2	0.9	2.2	4.9
ISR/FSR Uncertainties	-	-	-	-	-	-	-	-	-	-	0.6	0.2	0.1	0.0

CDF:  $WH \rightarrow \ell\nu\tau^+\tau^-$  and  $ZH \rightarrow \ell^+\ell^-\tau^+\tau^- \ell\tau_h\tau_h + X$  channel relative uncertainties (%)

Contribution	$ZZ$	$WZ$	$WW$	$DY(ee)$	$DY(\mu\mu)$	$DY(\tau\tau)$	$Z\gamma$	$t\bar{t}$	$W\gamma$	$W + jet$	$WH$	$ZH$	$VBF$	$gg \rightarrow H$
Luminosity	5.9	5.9	5.9	5.9	5.9	5.9	5.9	5.9	5.9	5.9	5.9	5.9	5.9	5.9
Cross Section	11.7	11.7	11.7	5.0	5.0	5.0	11.7	14.1	11.7	5.0	5.0	5.0	10.0	10.0
Z-vertex Cut Efficiency	0.5	0.5	0.5	0.5	0.5	0.5	0.5	0.5	0.5	0.5	0.5	0.5	0.5	0.5
Trigger Efficiency	1.0	1.1	0.9	1.0	1.1	1.1	1.1	1.0	0.7	0.9	1.1	1.1	1.1	1.1
Lepton ID Efficiency	3.3	3.3	3.3	3.3	3.3	3.3	3.3	3.3	3.3	3.3	3.3	3.3	3.3	3.3
Lepton Fake Rate	10.4	6.8	38.1	43.3	39.9	24.8	32.8	34.2	28.8	34.8	3.1	5.9	28.1	26.3
Jet Energy Scale	5.5	0.0	0.0	3.3	1.6	1.2	1.6	0.0	0.0	1.1	0.1	0.6	1.8	1.7
MC stat	12.5	8.1	16.9	18.3	12.5	4.9	12.6	14.7	70.7	8.7	2.0	3.3	9.4	18.3
PDF Model	-	-	-	-	-	-	-	-	-	-	1.2	0.9	2.2	4.9
ISR/FSR Uncertainties	-	-	-	-	-	-	-	-	-	-	1.2	0.5	0.4	0.04

TABLE XXXVI: Systematic uncertainties on the signal and background contributions for CDF’s  $WH + ZH \rightarrow jjbb$  and  $VBF \rightarrow jjbb$  channels. Systematic uncertainties are listed by name; see the original references for a detailed explanation of their meaning and on how they are derived. Uncertainties with provided shape systematics are labeled with “s”. Systematic uncertainties for  $H$  shown in this table are obtained for  $m_H = 115 \text{ GeV}/c^2$ . Uncertainties are relative, in percent, and are symmetric unless otherwise indicated. The cross section uncertainties are uncorrelated with each other (except for single top and  $t\bar{t}$ , which are treated as correlated). The QCD uncertainty is also uncorrelated with other channels’ QCD rate uncertainties.

CDF:  $WH + ZH \rightarrow jjbb$  and  $VBF \rightarrow jjbb$  channel relative uncertainties (%)

Contribution	QCD	$t\bar{t}$	single-top	diboson	W/Z+Jets	VH	VBF
Jet Energy Correction		9 s	9 s	9 s	9 s	9 s	9 s
PDF Modeling						2	2
SecVtx+SecVtx		7.1	7.1	7.1	7.1	7.1	7.1
SecVtx+JetProb		6.4	6.4	6.4	6.4	6.4	6.4
Luminosity		6	6	6	6	6	6
ISR/FSR modeling						3 s	3 s
Jet Width		s	s	s	s	s	s
Trigger		3.6	3.6	3.6	3.6	3.6	3.6
QCD Interpolation	s						
QCD MJJ Tuning	s						
QCD NN Tuning	s						
cross section		7	7	6	50	5	10

TABLE XXXVII: Systematic uncertainties on the signal and background contributions for CDF’s  $H \rightarrow \gamma\gamma$  channels. Systematic uncertainties are listed by name; see the original references for a detailed explanation of their meaning and on how they are derived. Uncertainties are relative, in percent, and are symmetric unless otherwise indicated.

CDF:  $H \rightarrow \gamma\gamma$  channel relative uncertainties (%)

Channel	CC	CP	C’C	C’P
<b>Signal Uncertainties :</b>				
Luminosity	6	6	6	6
$\sigma_{ggH}/\sigma_{VH}/\sigma_{VBF}$	14/7/5	14/7/5	14/7/5	14/7/5
PDF	5	2	5	2
ISR/FSR	3	4	2	5
Energy Scale	0.2	0.8	0.1	0.8
Trigger Efficiency	1.0	1.3	1.5	6.0
$z$ Vertex	0.07	0.07	0.07	0.07
Conversion ID	–	–	7	7
Detector Material	0.4	3.0	0.2	3.0
Photon/Electron ID	1.0	2.8	1.0	2.6
Run Dependence	3.0	2.5	1.5	2.0
Data/MC Fits	0.4	0.8	1.5	2.0
<b>Background Uncertainties :</b>				
Fit Function	2.8	0.9	6.1	3.3

TABLE XXXVIII: Systematic uncertainties on the signal and background contributions for D0's  $H \rightarrow \gamma\gamma$  channel. Systematic uncertainties for the Higgs signal shown in this table are obtained for  $m_H = 125 \text{ GeV}/c^2$ . Systematic uncertainties are listed by name; see the original references for a detailed explanation of their meaning and on how they are derived. Uncertainties are relative, in percent, and are symmetric unless otherwise indicated.

D0:  $H \rightarrow \gamma\gamma$  channel relative uncertainties (%)

Contribution	Background	Signal
Luminosity	6	6
Acceptance	–	2
electron ID efficiency	2	–
electron track-match inefficiency	10	–
Photon ID efficiency	3	3
Cross Section	4	10
Background subtraction	15	-